

Modeling and Control of the Aeroelastic Response of Highly Flexible Active Wings

by

Miguel Ortega-Morales

Mechanical Engineer
Polytechnical University of Catalonia, 1993

Submitted to the Department of Aeronautics and Astronautics
in Partial Fulfillment of the Requirements for the Degree of

Master of Science in Aeronautics and Astronautics

and

Engineer in Aeronautics and Astronautics

at the

Massachusetts Institute of Technology

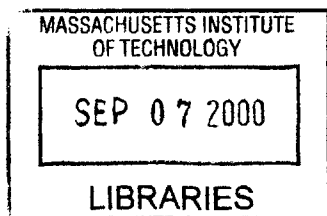
February 2000

©2000 Massachusetts Institute of Technology
All rights reserved

Signature of Author.....
Department of Aeronautics and Astronautics
January 28, 2000

Certified by.....
Carlos E. S. Cesnik
Assistant Professor of Aeronautics and Astronautics
Thesis Supervisor

Accepted by.....
Nesbitt W. Hagood, IV
Chairman, Department Graduate Committee



Aero

Modeling and Control of the Aeroelastic Response of Highly Flexible Active Wings

by

Miguel Ortega-Morales

Submitted to the Department of Aeronautics and
Astronautics on February 28, 2000 in Partial Fulfillment
of the Requirements for the Degree of Master of Science
in Aeronautics and Astronautics and the Degree of
Engineer in Aeronautics and Astronautics

ABSTRACT

The present work presents an integrated framework to study the behavior of highly flexible wings with distributed actuation control, providing the ability to explore structural flexibility to enhance flight performance and reduce overall weight.

A non-linear analysis tool is used for the aeroelastic analysis. It is a combination of a geometrically-exact mixed formulation for dynamics of moving beams and finite-state unsteady aerodynamics with the ability to model dynamic stall. It includes the appropriate constitutive law to incorporate the effects of distributed integral anisotropic actuators.

An active composite beam cross-sectional model has been developed to supply the properties required by the aeroelastic analysis. It is derived from three-dimensional electroelasticity, where the original problem is reduced via the variational asymptotic method. The resulting cross-sectional analysis is able to take into consideration passive and active anisotropic, non-homogeneous materials and to represent general cross-sectional geometries. The developed formulation is numerically implemented in VABS-A, and several numerical and experimental tests cases are used to support validation of the proposed theory.

A Linear Quadratic Gaussian regulator is implemented for the control of a linearized plant about a non-linear equilibrium. Several interfacing tools including three-dimensional and two-dimensional simulators of the complete aeroelastic model are developed to assist in the design process.

The viability of the present framework as an aeroelastic analysis tool is proven by computer simulation of selected cases on a proposed wind-tunnel model. Different controllers are simulated for set flight velocities in order to study the impact of parameter variation in flight performance, namely angle of attack, actuation orientation and grouping, and sensor location and type. A normalized control cost denoting the actuation energy and a normalized state cost denoting the total energy of the wing are the selected performance parameters. The results indicate that the regulator offers linearized increased stability margin together with effective gust alleviation even above the flutter airspeed.

Thesis Supervisor: Carlos E. S. Cesnik
Title: Assistant Professor of Aeronautics and Astronautics

Acknowledgments

The realization of this thesis would have never been accomplished without the professional and human qualities of my advisor, Professor Carlos E. S. Cesnik.

This work was sponsored in part by the Air Force Office of Scientific Research, under Grant F49620-98-0289 and Subgrant E-16-N96-G1.

Table of Contents

ACKNOWLEDGMENTS	5
TABLE OF CONTENTS	7
LIST OF FIGURES	11
LIST OF TABLES	17
1. INTRODUCTION.....	19
1.1 Motivation.....	19
1.2 Previous Work.....	20
1.3 Present Work Overview	23
2. ACTIVE AEROELASTIC ANALYSIS.....	27
2.1 Aeroelastic Model.....	27
2.1.1 Basic Geometry	28
2.1.2 Structural Analysis	29
2.1.3 Aerodynamic Analysis	33
2.1.4 Solution of the Aeroelastic System	35
2.2 Active Composite Beam Cross-Sectional Model.....	37
2.2.1 Previous Work.....	37
2.2.2 Formulation	40
2.2.2.1 Three-Dimensional Formulation.....	41
2.2.2.1.1 Strain Field.....	41
2.2.2.1.2 Energy Functional of an Active Beam	43
2.2.2.2 Small Parameters	44
2.2.2.3 Discretization.....	45
2.2.2.4 Warping Field for a Prismatic Beam	46

2.2.2.5 Stiffness and Actuation Constants	47
2.2.3 Finite Element Implementation: VABS-A	48
2.2.4 Validation	48
2.2.4.1 Active Box-Beam Cases	49
2.2.4.2 Simple Active NACA 0012 Wing	52
2.2.4.3 ATR Prototype Blade	54
2.2.4.3.1 Front Spar	55
2.2.4.3.2 Full Blade.....	59
2.2.4.4 Mach-Scaled CH47-D Active Blade Section.....	64
3. AEROELASTIC CONTROL DESIGN.....	67
3.1 The LQR Regulator	67
3.2 The LQG Regulator	69
3.3 Structural and Aerodynamic Modes	72
3.4 Sensing	73
3.4.1 Sensor Types	73
3.4.2 Sensor Placement	75
3.5 Gust model.....	76
3.6 Cost Calculation and Normalization	77
3.6.1 Formulation	77
3.6.1.1 Cost Functions for a LQR Regulator	78
3.6.1.2 Cost Functions for a LQG Regulator.....	80
3.6.2 Implementation.....	81
3.7 Transfer Function Sinusoidal Disturbance to Normalized Voltage Magnitude	82
3.7.1 Formulation	83
3.7.2 Implementation.....	84
3.8 Stability Cost and Pole-Zero Mapping.....	85
3.8.1 Stability Cost	85
3.8.2 Pole Zero Mapping.....	86
3.9 Stall Detection.....	86
3.9.1 Formulation	87

3.9.2 Simulation results	88
3.9.3 Control design using the parity signal	88
4. RESULTS	93
4.1 A Proposed Wind Tunnel Model Wing	93
4.2 Open Loop Performance	96
4.2.1 The Effect of Airspeed	96
4.2.2 The Effect of Angle of Attack	101
4.3 Closed Loop Performance	102
4.3.1 Stabilizing the plant by determining the weighting parameter ρ	103
4.3.2 The Effect of Actuation Orientation	107
4.3.2.1 The Effect of Actuation Orientation on Stability	108
4.3.2.2 The Effect of Actuation Orientation on Gust Alleviation	110
4.3.2.2.1 Wing Flying Above Flutter Speed	113
4.3.2.2.2 Wing Flying Below Flutter Speed	119
4.3.3 The Effect of Multiple Control Regions	125
4.3.3.1 The Effect of Multiple Control Regions on Stability	126
4.3.3.2 The Effect of Multiple Control Regions on Gust Alleviation	127
4.3.4 The Effect of Sensor Type and Placement	127
4.3.4.1 The Effect of Sensor Type and Placement on Stability	131
4.3.4.2 The Effect of Sensor Type and Placement on Gust Alleviation	132
4.3.5 Robustness Check	133
4.3.5.1 Robustness of the Regulator under Changes in the Airspeed	134
4.3.5.2 Robustness of the Regulator under Changes in the Root Angle of Attack	135
CONCLUSIONS	137
FUTURE WORK	141
BIBLIOGRAPHY	143
APPENDIX A - CROSS-SECTIONAL PROPERTIES FOR THE WIND TUNNEL MODEL (NACA 0014)	151

APPENDIX B - AN APPROXIMATION FOR THE STRUCTURAL MODES	165
APPENDIX C - SIMULATION.....	169
APPENDIX D - THE TCL/TK COMPUTER BASED FRAMEWORK.....	175

List of Figures

Figure 2.1 Wing frames of reference. 28

Figure 2.2 Overview of the proposed beam analysis (shaded areas represent the scope of this section). 39

Figure 2.3 Kinematics of a slender (beam) structure. 43

Figure 2.4 Active Fiber Composite: (a) mode of operation, showing axial extension along fibers and contraction transverse to fibers; (b) SEM photo of the cross section..... 49

Figure 2.5 Geometry and material distribution of the box-beam BB1 numerical test case 50

Figure 2.6 Geometry and material distribution of the box-beam BB2 numerical test case 50

Figure 2.7 Geometry and material distribution of the simple active NACA 0012 cross section case..... 52

Figure 2.8 Tip twist induced by the applied voltage for the simple active NACA 0012 cross section case. 54

Figure 2.9 Schematic diagram of the final ATR blade section design. Dimensions are in inches..... 55

Figure 2.10 Torsional stiffness results for the ATR spar (only)-Experimental result has $\pm 5\%$ deviation. 57

Figure 2.11 Actuation twist rate results for the ATR spar (only) for a 2000 Vpp. 59

Figure 2.12 Torsional stiffness results for the complete ATR blade-Experimental results has $\pm 5\%$ deviation. 60

Figure 2.13 Actuation twist rate results for the complete ATR blade..... 61

Figure 2.14 Warping modes for the ATR blade model *without including* the foam core (different magnifications were used to facilitate visualization). 62

Figure 2.15 Warping modes for the ATR blade model *including* the foam core (different magnifications were used to facilitate visualization). 63

Figure 2.16 1/6th Mach-scaled active CH47-D blade..... 64

Figure 3.1 Linear Quadratic Regulator (LQR) Diagram.....	68
Figure 3.2 Linear Quadratic Gaussian Diagram.....	70
Figure 3.3 Placement of two strain gauges at 0° in a non-symmetric longitudinal cross-section.....	74
Figure 3.4 1-Cosine gust model	76
Figure 3.5 Locus of the points that minimize the total energy of the system	82
Figure 3.6 Bode plot of the transfer function sinusoidal disturbance to normalized voltage.....	85
Figure 3.7 Flutter onset detection by pole movement tracking.....	86
Figure 3.8 Diagram of a stall detection and control model.....	87
Figure 3.9 Simulink block diagram of a stall detection and control model	90
Figure 3.10 Simulink block of the aerodynamics model	91
Figure 3.11 Simulink block of the lift stall model	91
Figure 3.12 Generation of the parity function.....	92
Figure 4.1 Planform diagram of the proposed wing design showing the distribution of the actuation (dimensions in cm).	94
Figure 4.2 Lay-up of the wind tunnel model's cross-section (NACA 0014).....	94
Figure 4.3 Maximum actuation for twist and bending as function of the AFC actuator ply angle.	95
Figure 4.4 Open loop pole variation of the plant with airspeed (zoomed below).....	98
Figure 4.5 Open loop structural modes at zero speed, 2° angle of attack and AFCs oriented at $\pm 45^\circ$ (modes 1 to 10).....	99
Figure 4.6 Open loop structural modes at zero speed, 2° angle of attack and AFCs oriented at $\pm 45^\circ$ (modes 11 to 20).....	100
Figure 4.7 Open loop structural modes at flutter speed, 2° angle of attack and AFCs oriented at $\pm 45^\circ$ (modes 1 to 10).....	101
Figure 4.8 Effect of non-linear steady state on flutter.....	102
Figure 4.9 State cost vs. control cost plot for a configuration flown at 15% over the flutter speed and at 2° root angle of attack.....	105

Figure 4.10 Open loop (\times) - closed loop (\diamond) pole map of the $\pm 45^\circ$ actuator orientation at 2° root angle of attack from flutter speed (43.4 m/s) to 15% above flutter (49.9 m/s) in 2.5% intervals (zoomed below)..... 106

Figure 4.11 Normalized stability control cost vs. percentage over flutter speed for the wing flying at 2° root angle of attack (zoomed on the right) for different actuator orientations..... 109

Figure 4.12 Sinusoidal disturbance to voltage T.F. for $\pm 45^\circ$ actuation orientation actuated in torsion (above) and bending (below), at 2° root angle of attack and 15% above flutter..... 111

Figure 4.13 Sinusoidal disturbance to voltage T.F. for the 0° actuation orientation actuated in bending at 2° root angle of attack and 15% above flutter..... 112

Figure 4.14 Profile of the ‘1-Cosine’ gust disturbance (5 m/s, 3 Hz)..... 114

Figure 4.15 State energy for actuation oriented at $\pm 45^\circ$ actuated in torsion under a 5 m/s, 3 Hz gust disturbance at 15% above flutter speed and wing at 2° root angle of attack. 115

Figure 4.16 Control energy for actuation oriented at $\pm 45^\circ$ actuated in torsion under a 5 m/s, 3 Hz gust disturbance at 15% above flutter speed and wing at 2° root angle of attack. 115

Figure 4.17 Gust alleviation for twist actuation oriented at $\pm 45^\circ$. (i) chordwise tip deflection (u_2), (ii) flatwise tip deflection (u_3), (iii) tip rotation (θ_3). Gust frequency is 3 Hz at 15% above flutter speed and root angle of attack is 2° 116

Figure 4.18 Voltage history for twist actuation oriented at $\pm 45^\circ$ under a 3 Hz gust disturbance at 15% above flutter speed, and 2° root angle of attack. 116

Figure 4.19 Gust alleviation for bending actuation oriented at $\pm 45^\circ$. (i) chordwise tip deflection (u_2), (ii) flatwise tip deflection (u_3), (iii) tip rotation (θ_3). Gust frequency is 3 Hz at 15% above flutter speed and root angle of attack is 2° 117

Figure 4.20 Voltage history for bending actuation oriented at $\pm 45^\circ$ under a 3 Hz gust disturbance at 15% above flutter speed, and 2° root angle of attack. 117

Figure 4.21 Gust alleviation for bending actuation oriented at 0° . (i) chordwise tip deflection (u_2), (ii) flatwise tip deflection (u_3), (iii) tip rotation (θ_3). Gust frequency is 3 Hz at 15% above flutter speed and root angle of attack is 2° 118

Figure 4.22 Voltage history for bending actuation oriented at 0° under a 3 Hz gust disturbance at 15% above flutter speed, and 2° root angle of attack. 118

Figure 4.23 Gust alleviation for twist actuation oriented at $\pm 45^\circ$. (i) chordwise tip deflection (u_2), (ii) flatwise tip deflection (u_3), (iii) tip rotation (θ_3). Gust frequency is 3 Hz at 15% below flutter speed and root angle of attack is 2° 120

Figure 4.24 Voltage history for twist actuation oriented at $\pm 45^\circ$ under a 3 Hz gust disturbance at 15% below flutter speed, and 2° root angle of attack. 121

Figure 4.25 Gust alleviation for bending actuation oriented at $\pm 45^\circ$. (i) chordwise tip deflection (u_2), (ii) flatwise tip deflection (u_3), (iii) tip rotation (θ_3). Gust frequency is 3 Hz at 15% below flutter speed and root angle of attack is 2° 121

Figure 4.26 Voltage history for bending actuation oriented at $\pm 45^\circ$ under a 3 Hz gust disturbance at 15% below flutter speed, and 2° root angle of attack. 122

Figure 4.27 Gust alleviation for twist actuation oriented at $\pm 22^\circ$. (i) chordwise tip deflection (u_2), (ii) flatwise tip deflection (u_3), (iii) tip rotation (θ_3). Gust frequency is 3 Hz at 15% below flutter speed and root angle of attack is 2° 122

Figure 4.28 Voltage history for twist actuation oriented at $\pm 22^\circ$ under a 3 Hz gust disturbance at 15% below flutter speed, and 2° root angle of attack. 123

Figure 4.29 Gust alleviation for bending actuation oriented at $\pm 22^\circ$. (i) chordwise tip deflection (u_2), (ii) flatwise tip deflection (u_3), (iii) tip rotation (θ_3). Gust frequency is 3 Hz at 15% below flutter speed and root angle of attack is 2° 123

Figure 4.30 Voltage history for bending actuation oriented at $\pm 22^\circ$ under a 3 Hz gust disturbance at 15% below flutter speed, and 2° root angle of attack. 124

Figure 4.31 Gust alleviation for bending actuation oriented at 0° . (i) chordwise tip deflection (u_2), (ii) flatwise tip deflection (u_3), (iii) tip rotation (θ_3). Gust frequency is 3 Hz at 15% below flutter speed and root angle of attack is 2° 124

Figure 4.32 Voltage history for bending actuation oriented at 0° under a 3 Hz gust disturbance at 15% below flutter speed, and 2° root angle of attack. 125

Figure 4.33 Normalized stability control cost vs. percentage over flutter speed for the wing flying at 2° root angle of attack (zoomed on the right) for different number of twist active regions. 126

Figure 4.34 First bending modes and their curvatures with the actuators oriented at $\pm 45^\circ$ 129

Figure 4.35 First torsion modes and their curvatures with the actuators oriented at $\pm 45^\circ$ 129

Figure 4.36 Optimum locations if one strain gauge is used to sense each bending or torsion mode for a wing divided into 10 elements. 130

Figure 4.37 Stability control cost for five sensor configurations (“max” means the three types of sensors are present in each element; “full” implies there is a bending and a 131

Figure 4.38 Stability control cost for a regulator designed at 7.5% over flutter speed and tested at other speeds. 134

Figure 4.39 Percentage over the nominal stability control cost for a regulator designed at 7.5% over flutter speed and tested at other speeds. 135

Figure 4.40 Stability control cost for a regulator designed at 2° root angle of attack and 7.5% over flutter speed and tested at a $\pm 2^\circ$ interval. 136

Figure 4.41 Percentage over the nominal stability control cost for a regulator designed at 2° angle root of attack and 7.5% over flutter speed and tested at a $\pm 2^\circ$ interval. ... 136

Figure B.1 Unit force applied on a cantilever beam (u_3 measures the deflection). 165

Figure C.1 Element Rotation in Space 170

Figure C.2 Normalized voltages with respect to time for a wing divided into 5 active regions 172

Figure C.3 Two displacements and a rotation at the tip after a disturbance: (i) chordwise tip deflection (u_2), (ii) flatwise tip deflection (u_3), (iii) tip twist (θ_1). 172

Figure C.4 One frame in a 3-D simulation of a 5-element wing hit by a sinusoidal disturbance 173

List of Tables

Table 2.1 Material properties for the numerical box-beam cases (“L” direction is along the fibers and “N” is normal to the laminate)..... 51

Table 2.2 Non-zero stiffness and actuation constants for box-beam BB1..... 51

Table 2.3 Non-zero stiffness and actuation constants for box-beam BB2..... 52

Table 2.4 Material properties used in the Simple Active NACA 0012 wing Q_{ij} are the laminate reduced stiffnesses of the actuator pack—“L” direction is along the fibers and “N” is normal to the laminate)..... 53

Table 2.5 Non-zero stiffness and actuation constants for simple active NACA 0012 wing (N, N m, N m² for stiffness constants, and N/m, N m/m for the actuation constants).
..... 53

Table 2.6 Material properties used in the ATR prototype blade (Q_{ij} are the laminate reduced stiffnesses of the actuator pack—“L” direction is along the fibers and “N” is normal to the laminate). 56

Table 2.7 Non-zero stiffness and actuation constants for ATR spar (N, N m, N m² for stiffness constants, and N/m, N m/m for the actuation constants). 58

Table 2.8 Non-zero stiffness and actuation constants for ATR prototype full blade (N, N m, N m² for stiffness constants, and N/m, N m/m for the actuation constants). 60

Table 2.9 Peak-to-peak twist actuation results for the 1/6th Mach-scaled CH47-D active blade-based on 54% span and 4000 V_{PP}/800 V_{DC}..... 65

Table 4.1 Structural modes for zero airspeed, 2° angle of attack and AFCs at ±45° 97

Table 4.2 Flutter velocities for the different orientation of the AFC lamination angle for a root angle of attack of 2° 107

Table 4.3 Gust amplitudes used in the study of the different active configurations. 113

Table 4.4 Effect of the actuation orientation on the response settling time due to a gust disturbance of a wing flying at 15% above corresponding flutter speed and for a 2° root angle of attack. 114

Table 4.5 Effect of the actuation orientation on the response settling time due to a gust disturbance of a wing flying at 15% below corresponding flutter speed and for a 2° root angle of attack.....	120
Table 4.6 Effect of the number of twist active regions on the response settling time due to a gust disturbance of a wing flying at 15% above corresponding flutter speed and for a 2° root angle of attack.....	127
Table 4.7 Effect of the number of twist active regions on the response settling time due to a gust disturbance of a wing flying at 15% below corresponding flutter speed and for a 2° root angle of attack.....	127
Table 4.8 Location of the maximum curvature for the first three modes.....	130
Table 4.9 Effect of the sensor placement on the response settling time due to a gust disturbance of a wing flying at 15% above corresponding flutter speed and for a 2° root angle of attack.....	132
Table 4.10 Effect of the sensor placement on the response settling time due to a gust disturbance of a wing flying at 15% below corresponding flutter speed and for a 2° root angle of attack.....	133
Table A.1 Material properties for the wind tunnel model's cross section (NACA 0014).	151

Chapter 1

Introduction

1.1 Motivation

High Altitude Long Endurance (HALE) aircraft are gaining importance for future military and civilian missions. HALE aircraft need very high lift-to-drag ratio wings, thus leading to high aspect ratios. HALE Uninhabited Reconnaissance Aerial Vehicle (URAV) is essentially autonomous with as little manual inputs as possible. Uninhabited Combat Aerial Vehicles (UCAV) will push for high maneuverability and high loads, extending the flight envelope. If the classical aeroelastic approach of stiffening the structure to extend the aeroelastic stability margin is used, the final design is too heavy and poorly maneuverable.

This poses new challenges to the aeroelastician. Among them, there is the potential ability to explore structural flexibility to enhance flight performance, reduce structural weight and control aeroelastic instabilities. Due to the nature of such systems, non-linear aero-structural interactions will become important and will have to be tightly coupled with active controls. This can be achieved by means of an embedded array of distributed anisotropic strain actuators and sensors.

Robust active control systems are required due to inherent uncertainties in the modeling. Distributed sensing and actuation technologies are necessary for increased controllability and optimality of the controller. These sensing and actuation devices must be embedded as an integral part of the structural system for optimal performance.

There is clearly the need for a framework that tightly integrates the aerolastic modeling, the analysis and the control. The aeroelastician requires a development environment where the interactions between structures, aerodynamics and controls can be investigated without the need for costly experimental results. Such a design tool would allow the designer to

- model complicated built-up wing structures of moderate to high aspect ratio with the presence of embedded strain actuation and sensors distributed throughout the structure.
- model representative flow about the wings (including stall effects) without the complexity of CFD.
- understand the mechanisms of controlled aeroelastic interactions in highly flexible aerodynamic surfaces
- comprehend the interactions of sensors and actuators with an anisotropic structure
- validate the performance and robustness of the control methodology for aeroelastic instabilities of highly flexible wings
- provide a framework for straightforward aeroelastic tailoring
- provide a sufficiently high degree of fidelity to ensure that a control system designed for the model will work for real systems as well.
- reduce the overall development time for a new design

Such a design framework would be an invaluable tool for the aeroelastician and would provide decisive savings in cost and development time.

1.2 Previous Work

There is important work in the literature that covers some of the concepts just introduced, even though the goal of the present work is to incorporate all of them into a single framework. This section will review some of the most significant efforts.

Nonlinear aeroelastic analysis has gathered a lot of momentum in the last decade due to the availability of mathematical tools which help to model non-linear dynamic systems. The studies conducted by Dugundji and his co-workers are a combination of analysis and experimental validation of the effects of dynamic stall on aeroelastic instabilities for simple cantilevered laminated plate-like wings [1]. There, the ONERA stall model was used for aerodynamic loads, which is the model also adopted in the current work. Tang and Dowell have studied the flutter and forced response of a flexible rotor blade [2]. In this study, geometrical structural non-linearity and free-play structural

non-linearity are taken into consideration. Again, high angle of attack unsteady aerodynamics was modeled using the ONERA dynamic stall model. Virgin and Dowell have studied the non-linear behavior of airfoils with control surfaces free-play and investigated the limit-cycle oscillations and chaotic motion of airfoils [3]. Gilliatt, Strganac and Kurdila have investigated airfoil non-linear aeroelastic behavior both experimentally and analytically [32]. A non-linear support mechanism was constructed and is used to represent continuous structural non-linearities. Drela presented an aircraft simulation model with aerodynamics, structures, flight dynamics, and control laws fully and nonlinearly coupled [60]. In order to get a better understanding of the non-linear aeroelastic phenomena involving the entire vehicle, Cesnik and his co-workers have been developing a low-order high-fidelity aeroelastic model for preliminary design and control synthesis (Refs. [5] and [6]). It focuses on a very flexible high-aspect ratio (passive) composite wing with discrete flap control, and models the entire aircraft. The non-linear aeroelastic model adopted in the present framework is essentially based in that work.

Aeroelastic control can be more difficult than traditional aeroelastic problems, in that the control system introduces a second potential source of instability [6]. Ref. [13] describes an aeroelastic control experiment conducted both at MIT as well as at NASA Langley Research Center (LaRC) for a relatively rigid transonic transport wing. That resulted in the PARTI wing, which stands for Piezoelectric Aeroelastic Response Tailoring Investigation, which concentrated in linear aeroelasticity and its corresponding linear control law. This study examines the effects of the composite tailoring, geometric wing sweep, piezoelectric coverage, thickness and grouping, and the wing taper ratio on the passive and active aeroelastic behavior. However, since it represents a transport-like aircraft wing it does not address issues related to very flexible wings. Various approaches have been developed over the past years for the control of structures. Linear Quadratic Gaussian (LQG) control has been the most common control method adopted so far [14]. Lin [15] used a Sensitivity Weighted LQG for better performance by adding sensitivity to parameter variation in the cost function. This was compared against a compensator designed using a weighted average of LQG cost for a discrete set of plants (even there is no guarantee for the latter to yield stable intermediate plants). Recent approaches to control design take into account real parameter uncertainty optimally by using the Popov

stability criterion. These control methodologies have been applied to benchmark problems [16] and Middeck Active Control experiments with great success [17].

Finally, some selected physical means to achieve aeroelastic vibration and control are reviewed. There have been considerable efforts in the area of aeroservoelasticity. Livne [7] and Giurgiutiu and Rogers [49] present a good survey, reviewing recent applications of smart materials to suppress aeroelastic effects and vibrations in helicopters and in fixed wing aircraft. Conventional active flutter and vibration control technology, relying on the use of servo-hydraulic actuators, has given way to high-performance induced strain actuators. Loewy reviews the use of such smart materials technology in detail [8]. Millott and Friedmann highlighted the benefits of an aerodynamic servo-flap for active helicopter rotor control. They used an extensive aeroelastic model coupled with a vibration-reduction controller, which included geometrical nonlinearities and advanced unsteady 2-D aerodynamic models [53]. Hall and Prechl have implemented an effective servo flap and tested in hover [56]. Chen and Chopra [51] induce twist through PZT wafers embedded in the composite blade structure. Rodgers and Hagood [52] incorporated active fiber composites (AFC) into the construction of a 1/6th Mach scale CH-47D blade model for wind tunnel testing at Boeing Helicopters. Cesnik and Shin [41] have also been working on developing the NASA/Army/MIT Active Twist Rotor blade. Successful bench tests were conducted at MIT and hover tests at NASA Langley Transonic Dynamics Tunnel. The AFC consists of a laminated structure of PZT-fibers in an epoxy layer. The AFC will be the strain actuator used for the numerical results in Chapters 2 and 4 of the present work. Alternative concepts for controlling airplane aerodynamic surfaces have been under investigation, e.g. the Active Flexible Wing technology [9], other variable stiffness concepts [31], the Smart Wing effort by Northrop Grumman [11], and the aforementioned NASA PARTI wing [12].

1.3 Present Work Overview

The goal of the present work is to develop an integrated framework to study the behavior of highly flexible wings with distributed actuation. In particular, it should be able to model the interactions of sensors and actuators with an anisotropic structure. By exploring flexibility, the model will assist the designer in pursuing three fundamental objectives. Firstly, the ability to increase the stability margin of operation. Secondly, the capacity to perform gust alleviation. And thirdly, the minimization of the actuation energy needed in the active wing. By achieving those three goals, the designer will be able to minimize the total weight of the structure.

The present framework consists of three main building blocks: the *active aeroelastic analysis*, the *aeroelastic control design* and the *simulator*. They are introduced now and are described in detail in the following chapters. The block diagram in Figure 1.1 represents a complete overview of these blocks. It depicts the three main areas in which the framework is divided showing all the interactions between them and how the flow of data is fed or retrieved from the blocks. The figure should help to understand the explanation of the three pillars that make the framework that follows.

Chapter 2 is dedicated to the active aeroelastic analysis (which corresponds to the top half of Figure 1.1). It consists of two parts: the non-linear *aeroelastic model* (on the left), and the *active composite wing cross-sectional model* (on the right).

The non-linear aeroelastic model is able to handle representative flow about realistic high aspect ratio wings. It needs structural as well as aerodynamic data as input. Flight conditions and aerodynamic data are simply fed into the model as numerical values. On the contrary, the structural data (essentially the cross-sectional stiffness and the actuation constants) needs to be computed.

The active cross-sectional model handles this calculation. It allows general cross sectional geometries with anisotropic materials. Its finite element implementation is labeled as *VABS-A* (Variational Asymptotical Beam Sectional-Active analysis).

Chapter 3 addresses the control of the wing. The LQR is introduced first as a fundamental building block of the LQG, a much more realistic regulator. Upon study of a nominal configuration in open loop, the need for a regulator is realized and the LQG is

chosen. Appropriate tools to quantify that performance close up the chapter. The left part of the diagram in Figure 1.1 symbolizes the aeroelastic control design block.

In Chapter 4, the viability of the presented framework as an aerolastic tool for analysis and tailoring is demonstrated. A Linear Quadratic Gaussian regulator (LQG) is designed and simulated at set flight velocities on a wind-tunnel model representative of a UAV wing. Simulation on a digital computer allows to study the impact of parameter variation in flight performance, namely angle of attack, actuation orientation and grouping, and sensor location and type. Two are the selected performance parameters, the control cost denoting the actuation energy and the state cost denoting the total energy of the wing. Finally, a simple robustness checked is performed on the LQG regulator.

Appendix C deals with the two simulators: a two-dimensional and a three-dimensional one. The lower half of Figure 1.1 represents both simulators, each one in a corner of the figure. The simulator interfaces with the control design and provides an extremely intuitive way to visualize the behavior of the wing.

OVERVIEW

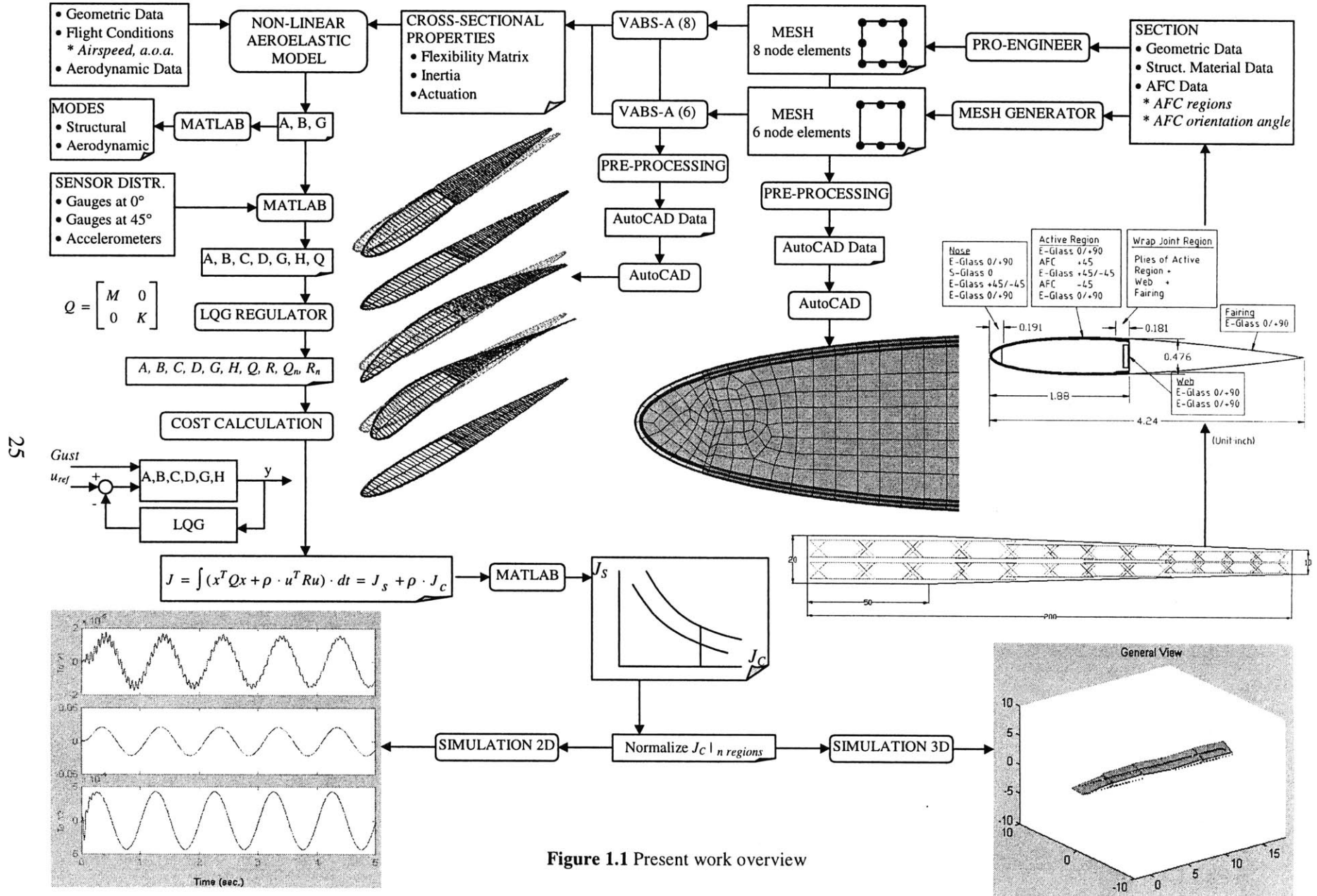


Figure 1.1 Present work overview

Chapter 2

Active Aeroelastic Analysis

This chapter describes in detail the active aeroelastic analysis model, which is a fundamental building block for the framework outlined in Chapter 1. The non-linear active aeroelastic model is introduced first. Due to the fact that the anisotropic strain actuators are embedded in the wing structure, the model requires an active composite beam cross-sectional formulation, which is presented next. The cross-sectional model is implemented in a finite element code, and several numerical and experimental tests cases are used to support validation of the proposed theory. Lastly, a cross-section mesh generator that provides the input for the model is introduced.

2.1 Aeroelastic Model

An active aeroelastic model that extends the non-linear aeroelastic formulation of Ref. [6] is developed here. It is a combination of a geometrically-exact mixed formulation for dynamics of moving beams and a finite-state unsteady aerodynamics with the ability to model dynamic stall. It includes the appropriate constitutive law to incorporate the effects of distributed integral anisotropic actuators. The basic theory is based on two separate works, viz. *i)* mixed variational formulation based on exact intrinsic equations for dynamics of moving beams [18] and, *ii)* finite-state airloads for deformable airfoils on fixed and rotating wings [19], [20].

The former theory is a non-linear intrinsic formulation for the dynamics of initially curved and twisted beams in a moving frame. There are no approximations to the geometry of the deformed reference line or to the orientation of the cross-sectional reference frame. A compact mixed variational formulation can be derived from these

equations, which is well suited for low-order beam finite element analysis. The exact intrinsic equations are extended to reflect the new constitutive law that also includes the effects of the anisotropic actuation. The vector that contains the actuation effects is a function of an external parameter (e.g. applied voltage in the case of piezoelectric actuators) that can be modulated by the controller as function of the sensing parameters (time dependent).

The latter work presents a state-space theory for the lift, drag, and all generalized forces of a deformable airfoil. The theory allows for a thin airfoil performing arbitrary small motions with respect to a reference frame that can perform arbitrary large motions.

2.1.1 Basic Geometry

Let a be the global frame, with its axes labeled as a_1 , a_2 and a_3 . The undeformed reference frame of the blade is named b , with its axes labeled as b_1 , b_2 and b_3 , and the deformed reference frame named B , with its axes labeled as B_1 , B_2 , and B_3 as represented in Figure 2.1.

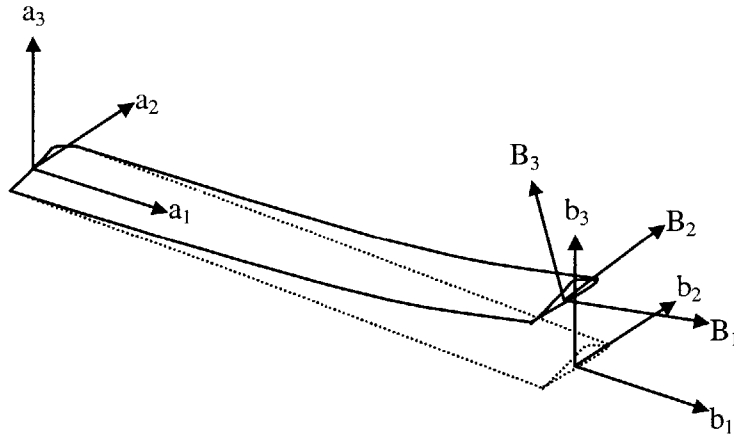


Figure 2.1 Wing frames of reference.

Any arbitrary vector Z represented by its components in one of the basis may be converted to another basis like

$$Z_b = C^{ba} Z_a, \quad Z_B = C^{Ba} Z_a \quad (2.1)$$

where C^{ba} is the transformation matrix from a to b , and C^{Ba} is that from a to B . There

are several ways to express the transformation matrices. C^{ba} can be expressed in terms of direction cosines from the initial geometry of the wing, while C^{Ba} contains the unknown rotation variables.

2.1.2 Structural Analysis

As described in details in Ref. [18], the variational formulation is derived from Hamilton's principle, which can be written as

$$\int_{t_1}^{t_2} \int_0^l [\delta(K - U) + \delta\overline{W}] dx_1 dt = \delta\overline{A} \quad (2.2)$$

where t_1 and t_2 are arbitrarily fixed times, K and U are the kinetic and potential energy densities per unit span, respectively. $\delta\overline{A}$ is the virtual action at the ends of the beam and at the ends of the time interval, and $\delta\overline{W}$ is the virtual work of applied loads per unit span.

Taking the variation of the kinetic and potential energy terms with respect to V_B and (the linear and angular velocity column vectors) and with respect to γ and κ (the generalized strain column vectors) yields

$$\begin{aligned} F_B &= \left(\frac{\partial U}{\partial \gamma} \right)^T, & M_B &= \left(\frac{\partial U}{\partial \kappa} \right)^T \\ P_B &= \left(\frac{\partial K}{\partial V_B} \right)^T, & H_B &= \left(\frac{\partial K}{\partial \Omega_B} \right)^T \end{aligned} \quad (2.3)$$

where F_B and M_B are internal force and moment column vectors, and P_B and H_B are linear and angular momentum column vectors.

The geometrically exact kinematical relations in the a frame are given by

$$\begin{aligned} \gamma^* &= C^{Ba} (C^{ab} e_1 + u'_a) - e_1 \\ \kappa^* &= C^{ba} \begin{pmatrix} \Delta - \frac{\tilde{\theta}}{2} \\ \theta^T \theta \\ 1 + \frac{\theta^T \theta}{4} \end{pmatrix} \cdot \theta' \end{aligned} \quad (2.4)$$

$$V_B^* = C^{Ba} (v_a + \dot{u}_a + \tilde{\omega}_a u_a)$$

$$\Omega_B^* = C^{ba} \begin{pmatrix} \Delta - \frac{\tilde{\theta}}{2} \\ \frac{\theta^T \theta}{1 + \frac{\theta^T \theta}{4}} \end{pmatrix} \cdot \dot{\theta} + C^{Ba} \omega_a$$

where u_a is the displacement vector measured in the a frame, θ is the rotation vector expressed in terms of Rodrigues parameters, e_1 is the unit vector $[1, 0, 0]^T$, Δ is the 3×3 identity matrix, and v_a and ω_a are the initial velocity and initial angular velocity of a generic point on the a frame. The $(\tilde{\cdot})$ operator applied to a column vector is defined as:

$$\tilde{Z} = \begin{bmatrix} 0 & -Z_3 & Z_2 \\ Z_3 & 0 & -Z_1 \\ -Z_2 & Z_1 & 0 \end{bmatrix} \quad (2.5)$$

The operator $(\dot{\cdot})$ denotes the derivative with respect to time, $(\cdot)'$ denotes the derivative with respect to x_l , and $(\cdot)^*$ denotes the expression of all the exact kinematical relations. To form a mixed formulation, Lagrange's multipliers are used to enforce V_B , γ and κ to satisfy the geometric equations in Eq. (2.4).

Manipulating the equations accordingly [21], one can obtain the variational formulation based on an exact intrinsic equations for dynamics of moving beams with respect to the fixed frame a as

$$\int_{t_1}^{t_2} \delta \Pi_a dt = 0 \quad (2.6)$$

where

$$\begin{aligned}
\delta\Pi_a = & \int_0^l \{ \delta u_a'^T C^T C^{ab} F_B + \delta u_a^T [(C^T \dot{C}^{ab} P_B) + \tilde{\omega}_a C^T C^{ab} P_B] + \\
& + \overline{\delta\psi}_a'^T C^T C^{ab} M_B - \overline{\delta\psi}_a^T C^T C^{ab} (\tilde{e}_1 + \tilde{\gamma}) F_B + \overline{\delta\psi}_a^T [(C^T \dot{C}^{ab} H_B) + \\
& + \tilde{\omega}_a C^T C^{ab} H_B + C^T C^{ab} \tilde{V}_B P_B] - \overline{\delta F}_a^T [C^T C^{ab} (e_1 + \gamma) - C^{ab} e_1] - \\
& - \overline{\delta F}_a'^T u_a - \overline{\delta M}_a^T (\Delta + \frac{\tilde{\theta}}{2} + \frac{\theta\theta^T}{4}) C^{ab} \kappa - \overline{\delta M}_a^T \theta + \\
& + \overline{\delta P}_a^T (C^T C^{ab} V_B - v_a - \tilde{\omega}_a u_a) - \overline{\delta P}_a^T \dot{u}_a + \\
& + \overline{\delta H}_a^T (\Delta + \frac{\tilde{\theta}}{2} + \frac{\theta\theta^T}{4}) (C^T C^{ab} \Omega_B - \omega_a) - \overline{\delta H}_a^T \dot{\theta} - \delta u_a^T f_a - \overline{\delta\psi}_a^T m_a \} dx_1 - \\
& - \left| \delta u_a^T \hat{F}_a + \overline{\delta\psi}_a^T \hat{M}_a - \overline{\delta F}_a^T \hat{u}_a - \overline{\delta M}_a^T \hat{\theta} \right|_0^l
\end{aligned} \tag{2.7}$$

and the rotation matrix C is the product and $C^{ba} C^{Ba}$, and it is expressed in terms of θ as

$$C = \frac{\left(1 - \frac{\theta^T \theta}{4} \right) \Delta - \tilde{\theta} + \frac{\theta\theta^T}{2}}{1 + \frac{\theta^T \theta}{4}} \tag{2.8}$$

In Eq. (2.7), f_a and m_a are the external force and moment vectors respectively, which result from aerodynamic loads. The $(\hat{\quad})$ terms are boundary values of the corresponding quantities, while the $(\bar{\quad})$ terms refer to the steady-state solution. $\overline{\delta\psi}$ is associated with virtual rotation and is not the variation of a function [18]. The generalized strain and force measures, and velocity and momentum measures are related through the constitutive relations in the following form:

$$\begin{aligned}
\begin{Bmatrix} F_B \\ M_B \end{Bmatrix} &= [K] \begin{Bmatrix} \gamma \\ \kappa \end{Bmatrix} - \begin{Bmatrix} F_B^{(a)} \\ M_B^{(a)} \end{Bmatrix} \\
\begin{Bmatrix} P_B \\ H_B \end{Bmatrix} &= \begin{bmatrix} m\Delta & -\tilde{\zeta}m \\ \tilde{\zeta}m & I \end{bmatrix} \begin{Bmatrix} V_B \\ \Omega_B \end{Bmatrix}
\end{aligned} \tag{2.9}$$

and these expressions are solved for γ , κ , V_B and Ω_B as function of the other measures and constants, and used in Eq. (2.7). In the inertia matrix, m is the mass per unit length, $m\tilde{\zeta}$ is the static unbalance, and I is the second moment of inertia. The stiffness $[K]$ is in general a 6×6 matrix, function of material distribution and cross sectional geometry. As

described in [22], the 6×6 stiffness matrix is related to the 4×4 one. The latter is used in this work, where the stiffness matrix and column vector for the piezoelectric actuation are described in Ref. [23].

Adopting a finite element discretization by dividing the wing into N elements, Eq. (2.6) is written as

$$\int_{t_1}^{t_2} \sum_i \delta \Pi_i dt = 0 \quad (2.10)$$

where index i indicates the i -th element with length Δl_i , $\delta \Pi_i$ is the corresponding spatial integration of the function in Eq. (2.8) over the i -th element. Due to the formulation's weakest form, the simplest shape functions can be used. Therefore, the following transformation and interpolation are applied within each element, similarly to the ones employed by [21]:

$$\begin{aligned} x &= x_i + \xi \Delta l_i, & dx &= \Delta l_i d\xi, & ()' &= \frac{1}{\Delta l_i} \frac{d}{d\xi} () \\ \delta u_a &= \delta u_i (1 - \xi) + \delta u_{i+1} \xi, & u_a &= u_i \\ \overline{\delta \psi}_a &= \overline{\delta \psi}_i (1 - \xi) + \overline{\delta \psi}_{i+1} \xi, & \theta &= \theta_i \\ \overline{\delta F}_a &= \overline{\delta F}_i (1 - \xi) + \overline{\delta F}_{i+1} \xi, & F_B &= F_i \\ \overline{\delta M}_a &= \overline{\delta M}_i (1 - \xi) + \overline{\delta M}_{i+1} \xi, & M_B &= M_i \\ \overline{\delta P}_a &= \overline{\delta P}_i, & P_B &= P_i \\ \overline{\delta H}_a &= \overline{\delta H}_i, & H_B &= H_i \end{aligned} \quad (2.11)$$

where u_i , θ_i , F_i , M_i , P_i and H_i are constant vectors at each node i , and all δ quantities are arbitrary. ξ varies from 0 to 1.

With these shape functions, the spatial integration in Eq. (2.10). can be performed explicitly to give

$$\begin{aligned} &\sum_{i=1}^N \{ \delta u_i^T f_{u_i} + \overline{\delta \psi}_i^T f_{\psi_i} + \overline{\delta F}_i^T f_{F_i} + \overline{\delta M}_i^T f_{M_i} + \overline{\delta P}_i^T f_{P_i} + \overline{\delta H}_i^T f_{H_i} + \delta u_{i+1}^T f_{u_{i+1}} + \\ &+ \overline{\delta \psi}_{i+1}^T f_{\psi_{i+1}} + \overline{\delta F}_{i+1}^T f_{F_{i+1}} + \overline{\delta M}_{i+1}^T f_{M_{i+1}} \} = \delta u_{N+1}^T \hat{F}_{N+1} + \overline{\delta \psi}_{N+1}^T \hat{M}_{N+1} - \\ &- \overline{\delta F}_{N+1}^T \hat{u}_{N+1} - \overline{\delta M}_{N+1}^T \theta_{N+1} - \delta u_1^T \hat{F}_1 - \overline{\delta \psi}_1^T \hat{M}_1 + \overline{\delta F}_1^T \hat{u}_1 - \overline{\delta M}_1^T \hat{\theta}_1 \end{aligned} \quad (2.12)$$

where the f_{u_i} , f_{ψ_i} , \dots , $f_{M_{i+1}}$ are the element functions explicitly integrated from the formulation.

Both γ and κ in each element function have to be replaced with a form that is a function of F_B and M_B using the inverse form of Eq. (2.9), along with the piezoelectric forcing vector $F_B^{(a)}$ and $M_B^{(a)}$. So does V_B and Ω_B with a form function of P_B and H_B . This substitution, which accounts for the presence of actuators embedded in the structure, leads to the following element functions:

$$\begin{aligned}
f_{\psi_i} &= -C^T C^{ab} M_i - \frac{\Delta l_i}{2} C^T C^{ab} \cdot [e_1 + r(F_i + F_i^{(a)}) + t(M_i + M_i^{(a)})] F_i + \\
&\quad + \frac{\Delta l_i}{2} (\tilde{\omega}_a C^T C^{ab} H_i + C^T C^{ab} \tilde{V}_i P_i) \frac{\Delta l_i}{2} (C^T C^{ab} H_i)^\circ - \bar{m}_i \\
f_{F_i} &= u_i - \frac{\Delta l_i}{2} [C^T C^{ab} \cdot [e_1 + \{r(F_i + F_i^{(a)}) + t(M_i + M_i^{(a)})\}] - C^{ab} e_1] \\
f_{M_i} &= \theta_i - \frac{\Delta l_i}{2} (\Delta + \frac{\tilde{\theta}_i}{2} + \frac{\theta_i \theta_i^T}{4}) C^{ab} \cdot \{t^T (F_i + F_i^{(a)}) + s(M_i + M_i^{(a)})\} \\
f_{\psi_{i+1}} &= C^T C^{ab} M_i - \frac{\Delta l_i}{2} C^T C^{ab} \cdot [e_1 + \{r(F_i + F_i^{(a)}) + t(M_i + M_i^{(a)})\}] F_i + \\
&\quad + \frac{\Delta l_i}{2} (\tilde{\omega}_a C^T C^{ab} H_i + C^T C^{ab} \tilde{V}_i P_i) \frac{\Delta l_i}{2} (C^T C^{ab} H_i)^\circ - \bar{m}_i \\
f_{F_{i+1}} &= -u_i - \frac{\Delta l_i}{2} \{C^T C^{ab} \cdot [e_1 + r(F_i + F_i^{(a)}) + t(M_i + M_i^{(a)})] - C^{ab} e_1\} \\
f_{M_{i+1}} &= -\theta_i - \frac{\Delta l_i}{2} (\Delta + \frac{\tilde{\theta}_i}{2} + \frac{\theta_i \theta_i^T}{4}) C^{ab} \cdot \{t^T (F_i + F_i^{(a)}) + s(M_i + M_i^{(a)})\}
\end{aligned} \tag{2.13}$$

where r , s and t are the components of the flexibility matrix expressed as

$$[K]^{-1} = \begin{bmatrix} r & t \\ t^T & s \end{bmatrix} \tag{2.14}$$

2.1.3 Aerodynamic Analysis

The aerodynamic loads used are as described in detail in Ref. [19]. The results are presented here. The theory calculates loads on a deformable airfoil undergoing large deformation in a subsonic flow. Certain aerodynamic parameters for the particular airfoil are required and are assumed to be known empirically or through a CFD analysis.

Let the mean chord line deformation of the airfoil cross section be described by $h(x_2, t)$ where x_2 is along the mean chord line. The frame motion along x_2 , x_3 -directions are, respectively, u_0 , $v(x_2, t)$. Let λ denote the induced flow due to free vorticity. Let

$L(x_2, t)$ denote the distribution of force perpendicular to the mean chord line. Let D be the drag on the airfoil. The integro-differential airloads equations can be converted into ordinary differential equations (ODEs) through a Glauert expansion. The ODEs are in terms of the expansion coefficients which are represented by a subscript n .

$$\begin{aligned} \frac{1}{2\pi\rho}\{L_n\} = & -b^2[M]\{\ddot{h}_n + \dot{v}_n\} - bu_0[C]\{\dot{h}_n + v_n - \lambda_0\} - u_0^2[N]\{h_n\} - \\ & - b[G]\{\dot{u}_0 h_n + \bar{u}_0 \zeta_n - u_0 v_n + u_0 \lambda_0\} \end{aligned} \quad (2.15)$$

$$\begin{aligned} \frac{1}{2\pi\rho}\{D_n\} = & -b\{\dot{h}_n + v_n - \lambda_0\}^T [S]\{\dot{h}_n + v_n - \lambda_0\} + b\{\dot{h}_n + \dot{v}_n\}^T [G]\{h_n\} - \\ & - u_0\{\dot{h}_n + v_n - \lambda_0\}^T [N - H]\{h_n\} + \{\dot{u}_0 h_n + \bar{u}_0 \zeta_n - u_0 v_n + u_0 \lambda_0\}^T [H]\{h_n\} \end{aligned} \quad (2.16)$$

where ρ , b are the air density and semichord respectively, and \bar{u}_0 is the velocity of the external bound vortex in the x_2 direction. The matrices denoted by $[N]$, $[C]$, $[G]$, $[S]$, $[H]$, $[M]$ are constant matrices whose expressions are given in Ref. [19].

The required airloads for lift and moment about mid chord are obtained as a linear combination of L_n . The inflow is obtained through the finite-state inflow theory [24]. The theory described so far is basically a linear, thin-airfoil theory. But the theory lends itself to corrections and modifications from experimental data. Thus, corrections such as thickness and Mach number can be incorporated very easily as described in Ref. [20]. It can also be extended to include dynamic stall effects according to the ONERA approach.

$$L_{T_n} = L_n + \rho u_T \Gamma_n \quad (2.17)$$

where

$$\begin{aligned} u_T = & \sqrt{u_0^2 + (v_0 + \dot{h}_0 - \lambda_0)^2} \\ \ddot{\Gamma}_n + \frac{u_T}{b} \eta \dot{\Gamma}_n + \left(\frac{u_T}{b}\right)^2 \omega^2 \Gamma_n = & -\frac{\omega^2 u_T^3 \Delta c_n}{b} - \omega^2 e u_T \frac{d}{dt}(u_T \Delta c_n) \end{aligned} \quad (2.18)$$

The parameters Δc_n , η , ω^2 , and e must be identified for a particular airfoil. The airloads are inserted into the Hamilton's principle to complete the aeroelastic model.

2.1.4 Solution of the Aeroelastic System

Eq. (2.12) yields a set of non-linear equations. These equations can be separated into structural (F_S) and aerodynamic (F_L) terms and written as

$$F_S(X, \dot{X}, \varepsilon) - F_L(X, Y, \dot{X}) = 0 \quad (2.19)$$

where X is the column matrix of structural variables, Y is a column matrix of inflow states and ε is the column matrix of magnitudes of the electrical field distribution shape. Similarly we can separate the inflow equations into an inflow component (F_I) and a downwash component (F_W) as

$$-F_W(\dot{X}) - F_I(Y, \dot{Y}) = 0 \quad (2.20)$$

The solutions of interest for the two coupled sets of equations (Eqs. (2.19) and (2.20)) can be expressed in the form

$$\begin{Bmatrix} X \\ Y \end{Bmatrix} = \begin{Bmatrix} \bar{X} \\ \bar{Y} \end{Bmatrix} + \begin{Bmatrix} \tilde{X}(t) \\ \tilde{Y}(t) \end{Bmatrix} \quad (2.21)$$

where $(\bar{\quad})$ is the steady-state solution and $(\tilde{\quad})$ denotes the small perturbation on it.

For the steady-state solution one gets \bar{Y} identically equal to zero (from Eq. (2.20)). Thus, one has to solve a set of non-linear equations given by

$$F_S(\bar{X}, 0, \varepsilon) - F_L(\bar{X}, 0, 0) = 0 \quad (2.22)$$

The Jacobian matrix of the above set of non-linear equations can be obtained analytically and is found to be very sparse [4]. Note that the presence of the actuation on the blade changes the original terms of the Jacobian in a similar manner it does in Eq. (2.12). The steady-state solution can be found very efficiently using Newton-Raphson method.

A dynamic stability (flutter) analysis about the steady-state can be performed once the solution is obtained. By perturbing Eqs. (2.19) and (2.20) about the calculated steady state using Eq.(2.21), the transient solution is obtained from

$$\begin{bmatrix} \frac{\partial F_S}{\partial X} & \frac{\partial F_L}{\partial X} & -\frac{\partial F_L}{\partial Y} \\ 0 & \frac{\partial F_L}{\partial Y} & \end{bmatrix}_{\substack{x=\bar{X} \\ y=0}} \begin{Bmatrix} \tilde{X} \\ \tilde{Y} \end{Bmatrix} + \begin{bmatrix} \frac{\partial F_S}{\partial \dot{X}} & \frac{\partial F_L}{\partial \dot{X}} & 0 \\ -\frac{\partial F_W}{\partial \dot{X}} & \frac{\partial F_I}{\partial \dot{Y}} & \end{bmatrix}_{\substack{x=\bar{X} \\ y=0}} \begin{Bmatrix} \dot{\tilde{X}} \\ \dot{\tilde{Y}} \end{Bmatrix} + \begin{bmatrix} \frac{\partial F_S}{\partial \varepsilon} & 0 \\ 0 & 0 \end{bmatrix}_{\substack{x=\bar{X} \\ y=0}} \begin{Bmatrix} \varepsilon \end{Bmatrix} = \begin{Bmatrix} 0 \\ 0 \end{Bmatrix} \quad (2.23)$$

Now assuming the dynamic modes to be of the form e^{st} , the above equations can be solved as an eigenvalue problem to get the modal damping, frequency and mode shape of the various modes:

$$\begin{aligned}\dot{x} &= \mathbf{A}x + \mathbf{B}u + \mathbf{G}w \\ y &= \mathbf{C}x + \mathbf{D}u\end{aligned}\quad (2.24)$$

where y is the output vector corresponding to any combination of three types of sensors distributed along the wing (accelerometers, bending and torsion strain gauges), u is the input vector corresponding to the electrical field applied to the piezoelectric actuators (where $u = \epsilon / \max(\epsilon)$), and w is the disturbance (gust).

The reduced state vector x is defined as

$$x = \begin{Bmatrix} \theta \\ \dot{\theta} \\ \lambda \end{Bmatrix}; \theta = \begin{Bmatrix} \theta_{11} \\ \theta_{21} \\ \theta_{31} \\ \vdots \\ \theta_{1n} \\ \theta_{2n} \\ \theta_{3n} \end{Bmatrix}; \lambda = \begin{Bmatrix} \lambda_{11} \\ \lambda_{21} \\ \vdots \\ \lambda_{51} \\ \lambda_{61} \\ \vdots \\ \lambda_{1n} \\ \lambda_{2n} \\ \vdots \\ \lambda_{5n} \\ \lambda_{6n} \end{Bmatrix}\quad (2.25)$$

where, again, θ are the Rodrigues parameters, λ are the inflow states, and n is the number of elements in which the wing is discretized. This reduced state vector is the result of assuming small (linear) deformations (with negligible axial deformation) about a fully non-linear steady-state.

2.2 Active Composite Beam Cross-Sectional Model

As presented in Section 2.1.2, the aeroelastic formulation requires the knowledge of the cross-sectional properties of the active wing. Therefore, a numerical analysis for modeling active composite beams with anisotropic actuation is presented here. This has been a major contributor to the present work and is presented in detail here. It is derived from three-dimensional electroelasticity, where the original problem is reduced via the variational asymptotic method. The resulting cross-sectional analysis is able to take into consideration passive and active anisotropic, non-homogeneous materials and to represent general (thin-walled, thick-walled, solid) cross-sectional geometries, requiring neither the costly use of 3-D finite element discretization nor the loss of accuracy inherent to any simplified representation of the cross section. The developed formulation is numerically implemented in VABS-A, and several numerical and experimental test cases are used to support validation of the proposed theory. The generality of the method and accuracy of the results should increase confidence at the design stage that the active beam structure will perform as expected and, consequently, should lower costs from experimental tests and further adjustments.

2.2.1 Previous Work

The technology of embedded piezoelectric actuators in a composite structure provides a new degree of design flexibility for advanced aircraft systems. The key to the technology is the ability to allow the structure to sense and react in a desired fashion, improving performance in the areas of structural vibration, acoustic signature, aeroelastic stability, and overall aircraft performance.

Due to their geometry, high-aspect ratio wings can often be treated as a beam, a one-dimensional (1-D) body. This idealization of the actual structure leads to a much simpler mathematical formulation than would be obtained if complete three-dimensional (3-D) elasticity formulation were used to model it. To do so, one has to find a way to capture the behavior associated with the two dimensions that are being eliminated by correctly accounting for geometry and material distribution over the cross section, which includes

the characterization of the active material as well. The process that takes the original 3-D body and represents it as a 1-D one is called “dimensional reduction.”

There has been a significant amount of work in the literature dealing with capturing the two-dimensional (2-D) effects, even though few do it in a systematic way. Among the leading efforts in cross-sectional modeling is the work presented in [26]. There, a finite-element-based non-homogeneous anisotropic initially curved and twisted beam theory is formulated from geometric non-linear, 3-D elasticity. The kinematics are derived for arbitrary warping (which includes out-of-plane as well as in-plane deformations) based upon the concept of decomposition of the rotation tensor. The 3-D strain energy based on this strain field is dimensionally reduced via the variational-asymptotical method [27]. The 3-D warping is calculated in terms of the 1-D strain measures and the functions in the strain energy become independent of the cross-sectional variables. The resulting equations govern both sectional and global deformation, as well as provide the 3-D displacement and strain fields in terms of beam deformation quantities. The formulation also naturally leads to geometrically exact, 1-D kinematical and intrinsic equilibrium equations for the beam deformation presented in Section 2.1.2.

Figure 2.2 shows an overview of the beam analysis. The developed theory was implemented numerically in a finite-element computer code called VABS (Variational-Asymptotical Beam Sectional Analysis). Correlations with experimental results and specialized analyses show excellent accuracy of the method. However, even though VABS can deal with cross sections that may have arbitrary geometry (solid or thin-walled, closed or open) and made of different materials, it only takes into account passive materials.

While good advances have been made in the area of *passive* cross-sectional modeling, the same cannot be said about cross sections with embedded orthotropic active layers. In fact, the latter concentrates on thin-walled beams, and most of the formulations are for single-cell active beams and are based on the passive beam model of Ref. [28] (see, for example, Refs. [29], [10], and [30]).

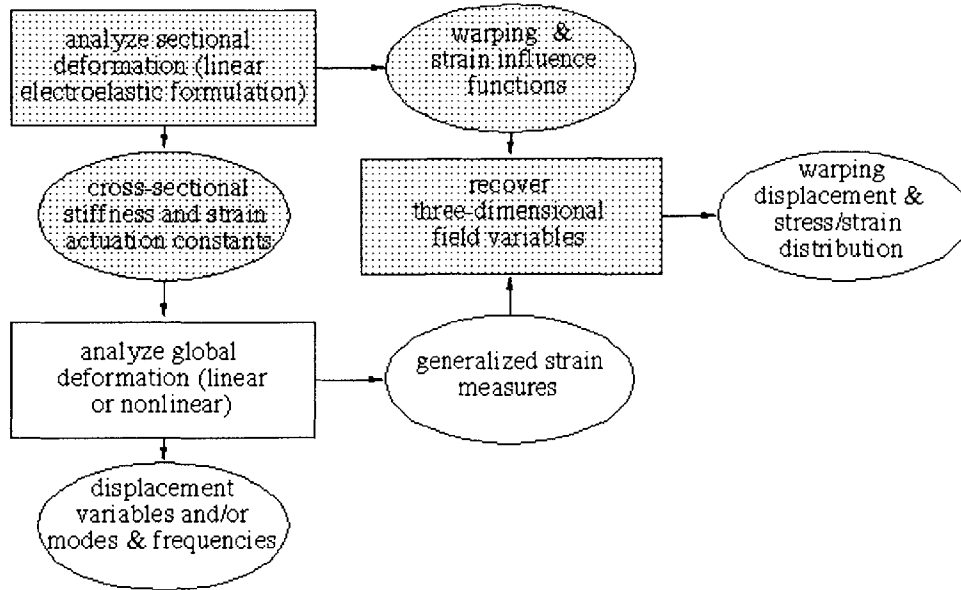


Figure 2.2 Overview of the proposed beam analysis (shaded areas represent the scope of this section).

The fundamental problem with those formulations is that there is no guarantee for consistent accuracy on the results due to lack of asymptotical correctness of the theory, a fact already established for passive composite cross-sectional analyses [26].

The first attempt in the literature to asymptotically analyze a multi-cell thin-walled composite beam with integral orthotropic active plies was presented in Ref. [4]. The variational-asymptotical method is used to formulate the stiffness constants of a two-cell cross section with the active plies consisting of piezoelectric fibers. This cross-sectional analysis is a particular case of the general framework established in Ref. [26]. It provides the expressions for the asymptotically-correct cross-sectional stiffness constants in closed form, facilitating design-trend studies. These stiffness constants are then used in a beam finite element discretization of the beam reference line. The exact intrinsic equations for the one-dimensional analysis of rotating beams considering small strains and finite rotations developed in Ref. [18] is extended to take into account the changes in the constitutive relation. Subject to external loads, active ply induced strains, and specific boundary conditions, the one-dimensional (beam) problem can be solved for displacements, rotations, and strains of the reference line. Finally, these results can be combined with information from the cross-sectional analysis in a set of recovering

relations for stress/strain distribution at each ply of the blade. For purely thin-walled beams, the asymptotic formulation of Ref. [4] was shown to present very good correlation with experimental results and numerical results from other specialized theories. However, the formulation breaks down when the cross section departs from being a thin-walled one. In practice, wings or helicopter blades can have thick walls and quite often have honeycomb or foam as integral part of the structure.

This section presents a flexible, general, and accurate formulation to deal with orthotropic active plies embedded in a composite construction within the same asymptotic framework for analyzing 3-D slender structures previously proposed in Refs. [4] and [26]. As pointed out before Ref. [33], the relation of the induced strain and the stiffness constants associated with the cross-sectional modeling is not uncoupled or trivial. It depends among other things on the warping field, which should be determined by the asymptotical procedure instead of being imposed *a priori*.

2.2.2 Formulation

In what follows, we replace the 3-D beam problem is replaced by an *approximate* 1-D one by taking advantage of the presence of certain small parameters in the modeling. The resulting 1-D strain energy per unit length is a function only of x_1 (length along a reference line r within an undeformed beam; x_2 and x_3 denote lengths along lines orthogonal to the reference line r). This dimensional reduction is done with the aid of the variational-asymptotical formulation (Refs. [27] and [26]). The kinematics of the beam are based on the general formulation of Ref. [34]. Local rotation, as defined therein, is taken to be of the order of the strain. Since only geometrically non-linear behavior is considered, the strain can be treated as small relative to unity without imposing any explicit restrictions on the magnitudes of the displacement of the reference line or the section rotation. The 3-D electroelastic constitutive behavior is assumed to be linear. Subject only to these restrictions, all possible deformations of beams are taken into account in the analysis and in the corresponding effects of an applied electric field.

2.2.2.1 Three-Dimensional Formulation

To start the asymptotical modeling process, we need to first define the 3-D formulation, the solution of which shall be considered the exact solution of the beam problem.

2.2.2.1.1 Strain Field

From Refs. [34] and [26], under the condition of small local rotation, Jaumann strain components can be expressed by

$$\Gamma = \frac{1}{h} \Gamma_h \nu + \Gamma_\epsilon \in + \Gamma_R \nu + \Gamma_l \nu' \quad (2.26)$$

where ν is the 3-D general warping field, and Γ_h , Γ_ϵ , Γ_R and Γ_l are linear (matrix) operators defined as

$$\Gamma_h = \begin{bmatrix} 0 & 0 & 0 \\ \frac{\partial}{\partial \zeta_2} & 0 & 0 \\ \frac{\partial}{\partial \zeta_3} & 0 & 0 \\ 0 & \frac{\partial}{\partial \zeta_2} & 0 \\ 0 & \frac{\partial}{\partial \zeta_3} & 0 \\ 0 & 0 & \frac{\partial}{\partial \zeta_3} \end{bmatrix}$$

$$\Gamma_\epsilon = \frac{1}{\sqrt{g}} \begin{bmatrix} 1 & 0 & -\zeta_3 & \zeta_2 \\ 0 & \zeta_3 & 0 & 0 \\ 0 & -\zeta_2 & 0 & 0 \\ 0 & 0 & 0 & 0 \\ 0 & 0 & 0 & 0 \\ 0 & 0 & 0 & 0 \end{bmatrix} \quad (2.27)$$

$$\Gamma_R = \frac{1}{\sqrt{g}} \left[\tilde{k} + k_1 I \left(\zeta_3 \frac{\partial}{\partial \zeta_2} - \zeta_2 \frac{\partial}{\partial \zeta_3} \right) \right]$$

$$\Gamma_l = \frac{1}{\sqrt{g}} \begin{bmatrix} I \\ 0 \end{bmatrix}$$

Again, $(\tilde{\epsilon})_{nm} = -e_{nmk}(\tilde{\epsilon})_k$. The column matrix ϵ represents the 1-D measures of deformation

$$\epsilon = \begin{Bmatrix} \gamma \\ h\kappa \end{Bmatrix} \quad (2.28)$$

where γ is the average cross-sectional extensional strain (the axial force strain measure) defined as

$$\gamma = \mathbf{R}' \cdot \mathbf{B} - 1 \quad (2.29)$$

with \mathbf{R} being the position vector to the cross-sectional reference point in the deformed beam, and \mathbf{B} is the orthogonal reference triad in the deformed state (see Figure 2.3). The column matrix $\kappa = [\kappa_1 \ \kappa_2 \ \kappa_3]^T$ contains the so-called moment strain measures

$$\kappa_n = K_n - k_n \quad (2.30)$$

where k is the initial curvature vector. The metric determinant g can be calculated as

$$\sqrt{g} = 1 - x_2 k_3 + x_3 k_2 \quad (2.31)$$

where $x \equiv \{x_2, x_3\}$ are cross-sectional local Cartesian coordinates which vary in the prescribed domain S , with area $|S|$. The characteristic size of the domain S is denoted by h and the dimensionless coordinates $\zeta \equiv \{\zeta_2 \equiv x_2/h, \ \zeta_3 \equiv x_3/h\}$ are introduced.

The small parameter $\tilde{\epsilon}$ can be now specified as

$$\tilde{\epsilon} \equiv \max \|\epsilon\| \quad (2.32)$$

A few non-linear terms in the strain field, which couple v and ϵ , have been neglected in Eq. (2.26) because a physically linear beam theory is to be developed. The form of the strain field is of great importance because it is now linear in ϵ , v and its derivatives. This is the only point where $\tilde{\epsilon}$ as a small parameter needs to be taken into account.

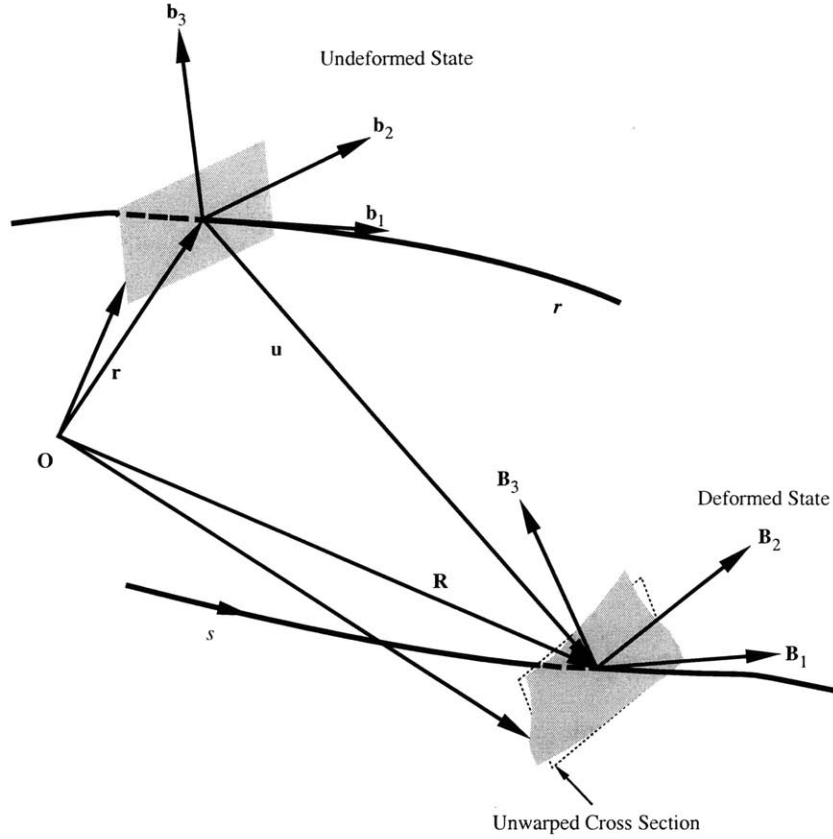


Figure 2.3 Kinematics of a slender (beam) structure.

2.2.2.1.2 Energy Functional of an Active Beam

Consider the linear 3-D electroelastic constitutive relation in the coordinate frame attached to the piezoelectric poling direction [35]

$$\begin{Bmatrix} \hat{Z} \\ \mathcal{D} \end{Bmatrix} = \begin{bmatrix} D^E & -(e)^T \\ e & \in^\Gamma \end{bmatrix} \cdot \begin{Bmatrix} \hat{\Gamma} \\ \varepsilon \end{Bmatrix} \quad (2.33)$$

where \hat{Z} is the 3-D Jaumann stress, conjugate of the 3-D Jaumann (mechanical) strain $\hat{\Gamma}$; \mathcal{D} is the electrical displacement, and ε is the electrical field. Also, D^E is the material stiffness matrix at constant (zero) electrical field, \in^Γ is the piezo-dielectric matrix at constant strain, and e is the piezoelectric field-stress coupling matrix. The latter is related to the piezoelectric field-strain coupling matrix d through the relation:

$$e = dD^E \quad (2.34)$$

Since the mechanical properties are normally expressed in the material frame, and later in the global frame \mathbf{r} , a transformation matrix \mathcal{J} is introduced that relates the poling frame to the global frame such that the electroelastic constitutive relation, Eq. (2.33), can be rewritten as

$$\begin{Bmatrix} \mathbf{Z} \\ \mathcal{D} \end{Bmatrix} = \begin{bmatrix} \mathcal{J}^T D^E \mathcal{J} & -\mathcal{J}^T e^T \\ e \mathcal{J} & \epsilon^\Gamma \end{bmatrix} \cdot \begin{Bmatrix} \Gamma \\ \epsilon \end{Bmatrix} \quad (2.35)$$

so that the piezoelectric constants, \mathcal{D} , and ϵ are still defined in the poling frame.

The energy density for an active beam per unit length can be written as [36]

$$U = \frac{1}{2} \langle \mathbf{Z}^T \Gamma \rangle - \frac{1}{2} \langle \mathcal{D}^T \epsilon \rangle \quad (2.36)$$

where the notation

$$\langle \bullet \rangle = \int_S \bullet \sqrt{g} dx_2 dx_3 = h^2 \int \bullet \sqrt{g} d\zeta_2 d\zeta_3 \quad (2.37)$$

is used throughout the formulation.

It is important to state at this point that the non-mechanical strain (coming from the piezoelectric effect) is considered to be of the same order as the strain, *i.e.*, of order $\tilde{\epsilon}$.

2.2.2.2 Small Parameters

Before one moves further on the asymptotical method, a definition of the small parameters present in the problem is necessary. There are four characteristic parameters in the considered theory, two of which, h and $\tilde{\epsilon}$, have already been introduced. The others are the characteristic length l , over which the deformation state varies in the longitudinal direction, and the characteristic length of the initial curvature and twist $R = 1/\max\|\mathbf{k}\|$. Let us consider the situation in which the parameters h , l , R (even though initially twisted or curved beams are not the subject of this work) and ϵ are present. The parameter ϵ does not need to be considered small any more, since the main problem has become linear with respect to the unknown functions $v_n(x, \zeta)$ and the 1-D strain measure ϵ . As a small parameter, $\tilde{\epsilon}$ has already been taken into account when deriving Eq. (2.26).

The warping $v_n(x, \zeta)$ is expanded as a series with respect to the small parameter h/l and h/R . Since both of them have the same numerator, the expansion in those parameters

is the same as the expansion in h only, and, therefore, both is simply represented by h (in spite of its dimension).

2.2.2.3 Discretization

To reduce the original 3-D problem to a 1-D one, the 3-D warping field v must be approximated as function of 1-D variables only. This approximation should carry the information of the geometry and material distribution of the cross section. In order to asymptotically evaluate this approximation, no closed form solution is available for an arbitrary cross-sectional geometry [26]. Therefore, the finite element method is used for this solution. The problem may be solved numerically by discretizing it with respect to the cross-sectional coordinates ζ_α , where $\alpha=2,3$.

Considering the finite element discretization, the unknown functions $v_n(x, \zeta)$ can be represented as the product of a shape function matrix $S(\zeta_\alpha)$ and a column matrix of nodal values of $v(x, \zeta)$, denoted as $V(x)$.

$$v(x, \zeta) = S(\zeta) \cdot V(x) \quad (2.38)$$

Using Eqs. (2.26) and (2.33) into Eq. (2.36), one obtains:

$$\begin{aligned} 2U = & \left(\frac{1}{h}\right)^2 V^T E V + 2 \left(\frac{1}{h}\right) V^T (D_{h\epsilon} \epsilon + D_{hR} V + D_{hl} V' - D_{hv} \bar{\epsilon}) + \\ & + (1) (\epsilon^T D_{\epsilon\epsilon} \epsilon + V^T D_{RR} V + V'^T D_{ll} V' + 2V^T D_{R\epsilon} \epsilon + 2V'^T D_{l\epsilon} \epsilon + \\ & + 2V^T D_{Rl} V' - 2\epsilon^T D_{\epsilon v} \bar{\epsilon} - V^T D_{Rv} \bar{\epsilon} - V'^T D_{lv} \bar{\epsilon}) - \bar{\epsilon}^T D_{vv} \bar{\epsilon} \end{aligned} \quad (2.39)$$

in which the following definitions were introduced

$$\begin{aligned} E &= \langle [\Gamma_h S]^T D[\Gamma_h S] \rangle & D_{\epsilon\epsilon} &= \langle [\Gamma_\epsilon]^T D[\Gamma_\epsilon] \rangle \\ D_{h\epsilon} &= \langle [\Gamma_h S]^T D[\Gamma_\epsilon] \rangle & D_{hR} &= \langle [\Gamma_h S]^T D[\Gamma_R S] \rangle \\ D_{hl} &= \langle [\Gamma_h S]^T D[\Gamma_l S] \rangle & D_{R\epsilon} &= \langle [\Gamma_R S]^T D[\Gamma_\epsilon] \rangle \\ D_{l\epsilon} &= \langle [\Gamma_l S]^T D[\Gamma_\epsilon] \rangle & D_{RR} &= \langle [\Gamma_R S]^T D[\Gamma_R S] \rangle \\ D_{Rl} &= \langle [\Gamma_R S]^T D[\Gamma_l S] \rangle & D_{ll} &= \langle [\Gamma_l S]^T D[\Gamma_R S] \rangle \end{aligned} \quad (2.40)$$

which are due purely to the mechanical properties, and

$$\begin{aligned}
D_{hv} &= \langle [\Gamma_h S]^T D d\bar{\epsilon} \rangle & D_{\epsilon v} &= \langle [\Gamma_\epsilon]^T D d\bar{\epsilon} \rangle \\
D_{Rv} &= \langle [\Gamma_R S]^T D d\bar{\epsilon} \rangle & D_{lv} &= \langle [\Gamma_l S]^T D d\bar{\epsilon} \rangle \\
D_{vv} &= \langle [D d\bar{\epsilon}]^T D d\bar{\epsilon} \rangle
\end{aligned} \tag{2.41}$$

which contain the electrical properties of the material as well (subindex v denotes association with electric fields). Here, $\bar{\epsilon}$ represents the electric field distribution within the domain of integration, and $\bar{\epsilon}$ is the magnitude of such distribution shape.

2.2.2.4 Warping Field for a Prismatic Beam

Even though the formulation presented above can handle initial twist and curvature effects in the structure, in what follows we consider only the case of prismatic beams. Therefore, all the terms on the energy that are function of h/R (the D matrices with at least one of the subscripts R) are neglected.

According to the variational asymptotical procedure, in order to get an approximation, one should retain only the leading terms in the energy expression. These ‘‘leading’’ terms are so with respect to the small parameter that contains the unknown functions and the leading intersection terms between the unknown function and the rest of the functional (for more details see Ref. [27]).

We are then left with the following expression

$$2U = \left(\frac{1}{h}\right)^2 V^T E V + 2 \left(\frac{1}{h}\right) V^T D_{h\epsilon} \epsilon - V^T D_{hv} \bar{\epsilon} \tag{2.42}$$

This functional must be minimized with respect to the variable V , subject to the constraints

$$V^T H \Psi_{cl} = 0 \tag{2.43}$$

where

$$H = \langle S^T S \rangle \tag{2.44}$$

and Ψ_{cl} is a matrix with four columns, each corresponding to one of the constraints defined in Ref. [37]. The set of columns Ψ_{cl} is determined by the kernel (null-space) of the matrix E , and has the physical meaning of possible rigid-body motion associated with each of the beam degrees of freedom. This implies that:

$$E\Psi_{cl} = 0 \quad (2.45)$$

Let us suppose that the set of columns of Ψ_{cl} is normalized such that

$$\Psi_{cl}^T H \Psi_{cl} = I \quad (2.46)$$

The Euler equation for the minimization problem defined by Eqs. (2.42) and (2.43) is given by

$$\left(\frac{1}{h}\right)EV + D_{h\epsilon} \in -D_{hv} \bar{\epsilon} = H\Psi_{cl} \mu \quad (2.47)$$

where μ/h is the column matrix of Lagrange multipliers associated with Eq. (2.43). By pre-multiplying Eq. (2.47) by Ψ_{cl}^T , one can show that

$$\mu = \Psi_{cl}^T (D_{h\epsilon} \in -D_{hv} \bar{\epsilon}) \quad (2.48)$$

Subsequently, Eq. (2.47) can be rewritten as

$$\left(\frac{1}{h}\right)EV = -(I - H\Psi_{cl} \Psi_{cl}^T) (D_{h\epsilon} \in -D_{hv} \bar{\epsilon}) \quad (2.49)$$

The matrix E possesses a zero eigenvalue of multiplicity four, and thus its inverse does not exist. However, let us introduce the matrix E_{cl}^+ with the following properties [37]

$$\begin{aligned} EE_{cl}^+ &= I - H\Psi_{cl} \Psi_{cl}^T \\ E_{cl}^+ E &= I - \Psi_{cl} \Psi_{cl}^T H \\ E_{cl}^+ EE_{cl}^+ &= E_{cl}^+ \end{aligned} \quad (2.50)$$

The solution of Eq. (2.49) is then represented by

$$V = -hE_{cl}^+ (D_{h\epsilon} \in -D_{hv} \bar{\epsilon}) = h(V_0 + V_0^{(a)}) \quad (2.51)$$

which explicitly shows the dependence of the warping field on the applied electric field, which is what the $V_0^{(a)}$ term represents. The structural-only term of the warping (V_0) is the same as obtained previously [26].

2.2.2.5 Stiffness and Actuation Constants

By substituting the above solution into the discretized energy density, Eq. (2.40), and keeping only terms with the lowest order, which are of order $h^0 \equiv 1$, one obtains

$$2U = \epsilon^T K \epsilon + 2\epsilon^T F^{(a)} - \bar{\epsilon}^T B^{(a)} \bar{\epsilon} \quad (2.52)$$

where the beam stiffness matrix K is

$$K = D_{\epsilon\epsilon} - D_{h\epsilon}^T E_{cl}^+ D_{h\epsilon} \quad (2.53)$$

and the actuation vector is

$$F^{(a)} = -(D_{\epsilon v} - D_{h\epsilon}^T E_{cl}^+ D_{hv}) \bar{\epsilon} \quad (2.54)$$

The matrix associated with the quadratic term for the electric field ($\bar{\epsilon}$) is found to be

$$B^{(a)} = D_{vv} + D_{hv}^T E_{cl}^+ D_{hv} \quad (2.55)$$

but it plays no role on the actuation problem under consideration here.

Therefore, the active beam constitutive relation is written as:

$$\begin{Bmatrix} F_1 \\ M_1 \\ M_2 \\ M_3 \end{Bmatrix} = \begin{bmatrix} K_{11} & K_{12} & K_{13} & K_{14} \\ K_{21} & K_{22} & K_{23} & K_{24} \\ K_{31} & K_{32} & K_{33} & K_{34} \\ K_{41} & K_{42} & K_{43} & K_{44} \end{bmatrix} \begin{Bmatrix} \gamma \\ \kappa_1 \\ \kappa_2 \\ \kappa_3 \end{Bmatrix} - \begin{Bmatrix} F_1^{(a)} \\ M_1^{(a)} \\ M_2^{(a)} \\ M_3^{(a)} \end{Bmatrix} \quad (2.56)$$

2.2.3 Finite Element Implementation: VABS-A

The theoretical development presented above has been numerically implemented in VABS, referred here as VABS-A to indicate its ability to handle anisotropic actuation. All VABS-A solutions are based on discretizing the cross section with 6-node isoparametric elements. The finite element implementation of this framework needs the cross-section to be discretized for input. A multi-cell airfoil-shape cross section mesh generator coded in Fortran was developed in-house for that objective. It generates 6-node element meshes for airfoils with any number of spars. It handles both the interior and exterior for symmetric airfoils and the outer skin for non-symmetrical. VABS-A is implemented in FORTRAN 77 and all the runs take less than 1.5 minutes (CPU time) on a Pentium II machine.

2.2.4 Validation

To validate VABS-A, several cases are considered where other numerical or experimental results are available. Even though the formulation is not restricted to this,

the integral actuation in the study cases is achieved through the use of active fiber composites (AFC) with interdigitated electrodes [38] (see Figure 2.4). This actuator concept provides a feasible way of integrally actuating the structure instead of the direct use of piezoceramic crystals, providing higher levels of actuation authority. Basic material characterization and proof of concept of an integral twisted-actuated rotor blade have been under investigation at MIT's Active Materials and Structures Laboratory ([39], [40], [4] and [41]).

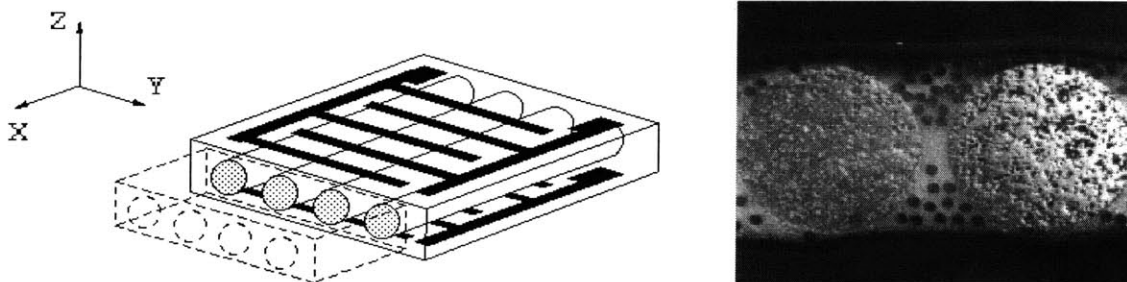


Figure 2.4 Active Fiber Composite: (a) mode of operation, showing axial extension along fibers and contraction transverse to fibers; (b) SEM photo of the cross section

For all the cases, actuation is obtained by using active fiber composites packs embedded in the composite construction. The asymptotic theory presented in Ref. [4] is used to support the numerical validation of the current formulation. It has been tested against experimental results and it correlates fairly well for thin-walled closed cross sections (a key assumption on the derivation of that formulation). For the experimental results, three different experiments conducted at MIT will provide the needed data associated with the global behavior of the beam.

2.2.4.1 Active Box-Beam Cases

Due to the nature of the asymptotic formulation, the present theory and the one developed in Ref. [4] should coincide at the limit when the wall thickness goes to zero. Therefore, as a starting point on the validation of the new formulation, two active box-beam cases were selected for numerical evaluation of the two main actuation mechanisms: axial force and twist moment.

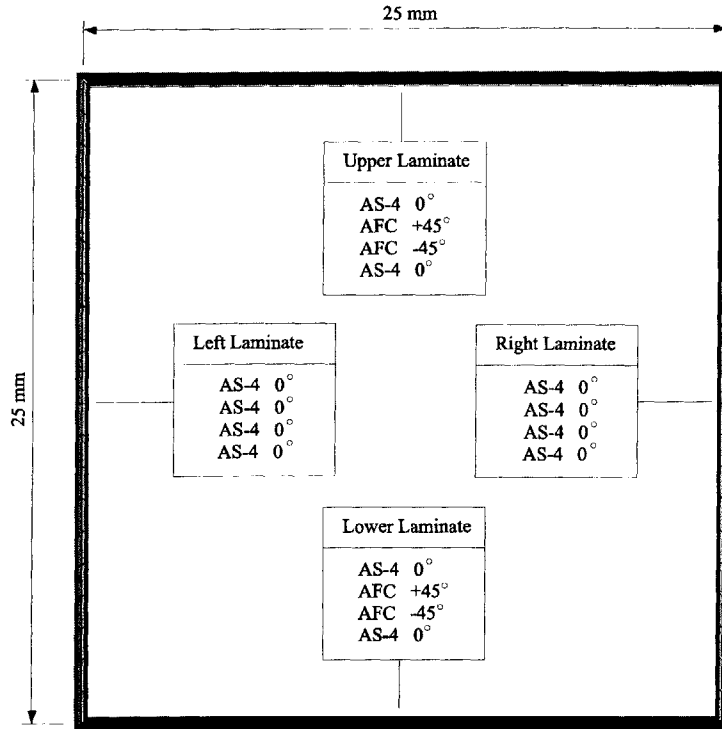


Figure 2.5 Geometry and material distribution of the box-beam BB1 numerical test case

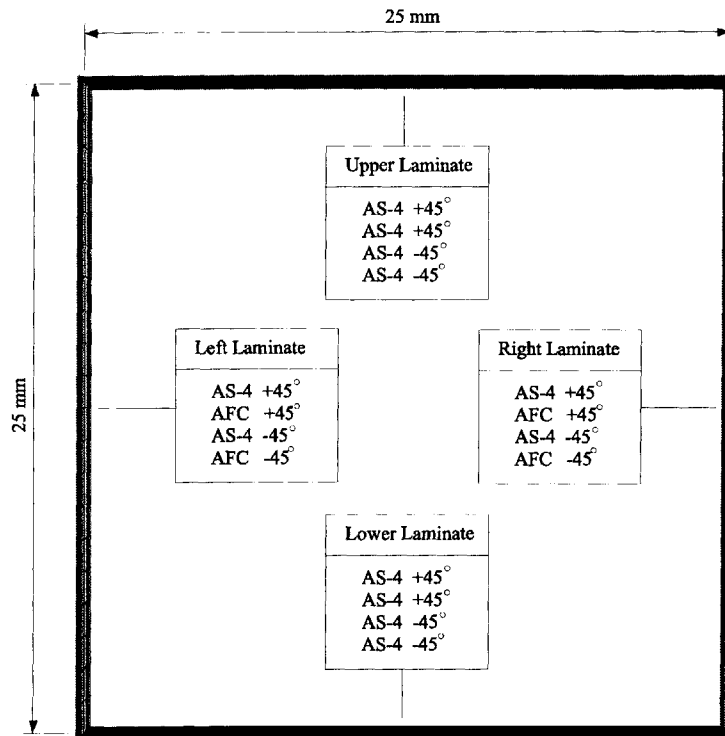


Figure 2.6 Geometry and material distribution of the box-beam BB2 numerical test case

Table 2.1 Material properties for the numerical box-beam cases (“L” direction is along the fibers and “N” is normal to the laminate).

	AS4/3506-1	AFC
E_L (GPa)	142	42.2
E_T (GPa)	9.8	17.5
G_{LT} (GPa)	4.8	5.5
ν_{LT}	0.3	0.354
Thickness (mm)	0.127	0.127
d_{11} (pm/V)	-	381
d_{12} (pm/V)	-	-160
electrode dist. (mm)	-	1.143

Consider the two box-beam described in Figures 2.5 and 2.6, named BB1 and BB2, respectively. The material properties used in these cases are given in Table 2.1. For both cases, a constant excitation of 2800 V was applied to the AFCs with +45° orientation, and -1200V to the AFCs with -45° orientation.

Using 320 elements (2400 degrees of freedom) to discretize these box-beams, VABS-A results for both the stiffness matrix and actuation vector can be found in Tables 2.2 and 2.3. Also in these tables are corresponding results extracted from Ref. [4].

Table 2.2 Non-zero stiffness and actuation constants for box-beam BB1.

	VABS-A	Ref.4	%Diff
K_{11} (N)	5.518E+06	5.518E+06	0.00
K_{12} (N m)	-5.246E+00	0.000E+00	-
K_{22} (N m ²)	5.468E+01	5.425E+01	0.79
K_{33} (N m ²)	6.294E+02	6.291E+02	0.05
K_{44} (N m ²)	4.745E+02	4.742E+02	0.06
$F_1^{(a)}$ (N/m)	3.457E+01	3.501E+01	-1.27
$M_1^{(a)}$ (N m/m)	1.678E+00	1.719E+00	-2.44

Table 2.3 Non-zero stiffness and actuation constants for box-beam BB2.

	VABS-A	Ref.4	%Diff
K_{11} (N)	9.924E+05	9.925E+05	-0.01
K_{12} (N m)	4.672E+03	4.670E+03	0.04
K_{22} (N m ²)	9.710E+01	9.627E+01	0.85
K_{33} (N m ²)	7.526E+01	7.494E+01	0.43
K_{44} (N m ²)	7.852E+01	7.821E+01	0.39
$F_1^{(a)}$ (N/m)	8.757E+01	8.712E+01	0.51
$M_1^{(a)}$ (N m/m)	1.382E+00	1.378E+00	0.29

As one can see, the agreement is excellent with the exception of a small extension-twist coupling neglected by the thin-walled assumption in Ref. [4].

2.2.4.2 Simple Active NACA 0012 Wing

The second selected test case is a NACA 0012 airfoil-shape cross section with piezoelectric actuators attached at the upper and lower surfaces (see Figure 2.7). This is one of the model beams fabricated and tested using AFC actuators [10]. The complete wing has a span of 0.45 m (beyond the clamping area at the root), with an active length of 0.372 m. In each pack of AFC, the piezoelectric (PZT-5H) fibers are aligned in +45° in order to maximize the actuation force in twist. Material properties for this case are presented in Table 2.4.

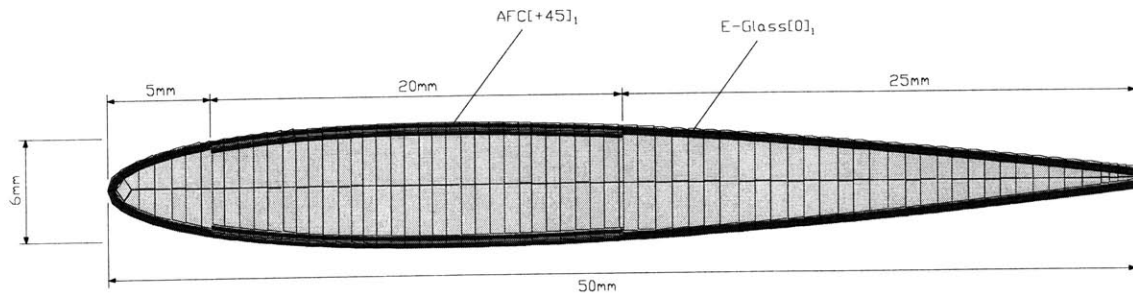


Figure 2.7 Geometry and material distribution of the simple active NACA 0012 cross section case.

The cross section has been discretized with 384 elements (2958 d.o.f.). The predicted stiffness coefficients and forcing vector induced by an electric field of $-1800\text{V}/1.114 \times 10^{-3} \text{ m}$ are given in Table 2.5.

A good correlation is shown when comparing those constants with the ones obtained using the thin-walled asymptotic formulation. The discrepancies verified in the stiffness constants, again, are within the expected due to the thin-wall assumption present in Ref. [4]. If one drives the wall thickness to zero, the two formulations will coincide.

Table 2.4 Material properties used in the Simple Active NACA 0012 wing Q_{ij} are the laminate reduced stiffnesses of the actuator pack—“L” direction is along the fibers and “N” is normal to the laminate).

E-Glass (Style 120 Fabric)	E_L (GPa)	14.8
	E_T (GPa)	13.6
	G_{LT} (GPa)	1.9
	ν_{LT}	0.19
	Ply thickness (mm)	0.2
AFC (PZT-5H)	Q_{11} (GPa)	32.8
	Q_{12} (GPa)	6.26
	Q_{22} (GPa)	17.3
	Q_{66} (GPa)	5.5
	d_{11} (pm/V)	381
	d_{12} (pm/V)	-160
	Ply thickness (mm)	0.17

Table 2.5 Non-zero stiffness and actuation constants for simple active NACA 0012 wing (N, N m, N m^2 for stiffness constants, and N/m, N m/m for the actuation constants).

	VABS-A	Ref.4	%Diff
K_{11} (N)	7.416E+05	7.508E+05	-1.24
K_{12} (N m)	4.225E+01	4.024E+01	4.76
K_{14} (N m)	1.470E+02	1.501E+02	-2.11
K_{22} (N m^2)	1.660E+00	1.450E+00	12.70
K_{33} (N m^2)	3.413E+00	3.175E+00	6.97
K_{44} (N m^2)	1.451E+02	1.465E+02	-0.96
$F_1^{(a)}$ (N/m)	-3.156E+01	-3.249E+01	2.95
$M_1^{(a)}$ (N m/m)	-1.001E-01	-1.038E-01	-3.70

Considering the global behavior of the wing, Figure 2.8 shows the tip twist results for VABS-A, the thin-walled analysis of Ref. [4], and the thin-walled analysis and experimental data from Ref. [10] as function of the applied voltage. As one can see, all the theoretical results are in close agreement among each other, and with fair agreement with the experiments. For these theoretical results, the piezoelectric constants (in d matrix) are obtained for high-voltage fields, and used throughout the analyses, even for low-voltage fields (corresponding to low voltages in Figure 2.8). Due to the non-linearity of the piezoelectric behavior, this approach is expected to overpredict actuation as verified from the results. However, no further material characterization was available for a more precise comparison.

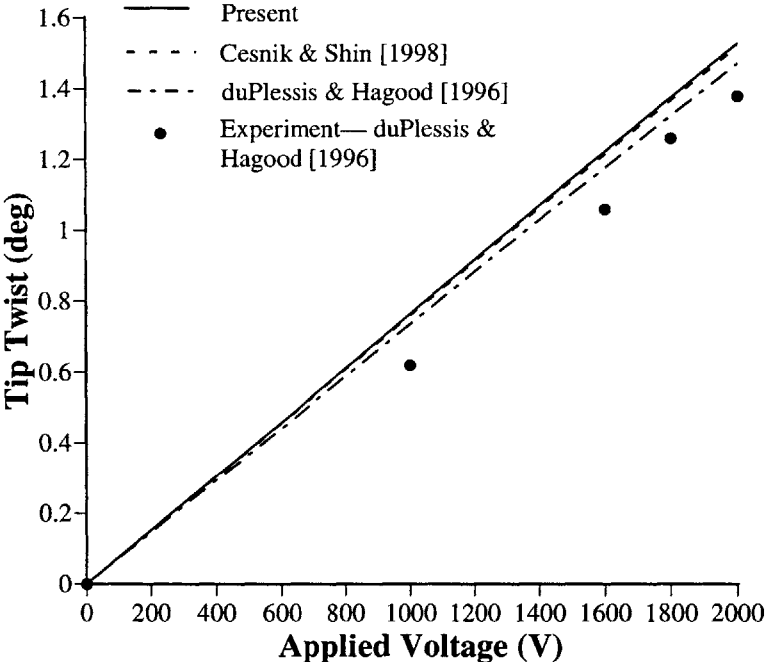


Figure 2.8 Tip twist induced by the applied voltage for the simple active NACA 0012 cross section case.

2.2.4.3 ATR Prototype Blade

As part of a joint program between NASA Langley/Army Research Laboratory and MIT, a prototype blade for the active twist rotor (ATR) system has been designed, built, and preliminary bench tests were conducted [41]. The cross-sectional analysis was

conducted using the active multi-cell thin-walled formulation of Ref. [4], and the final cross-sectional design is shown in Figure 2.9. The airfoil shape is a NACA 0012. As one can see, the main blade structure is composed of E-Glass, S-Glass, and piezoelectric fiber composites, the properties of which are given in Table 2.6. Also, the front and rear cells are filled with Rohacell 71 to facilitate its manufacturing.

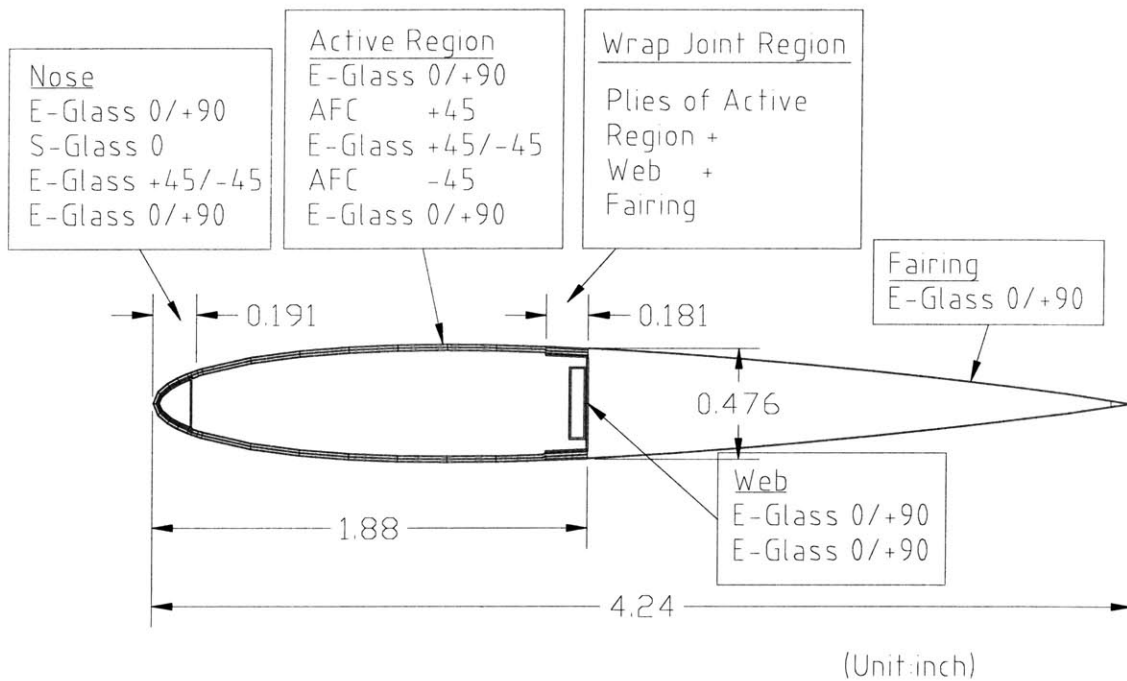


Figure 2.9 Schematic diagram of the final ATR blade section design. Dimensions are in inches.

Two subcases of this ATR prototype blade are studied here. First, the front spar without the fairing is characterized and tested. Second, the full blade including the fairing is studied.

2.2.4.3.1 Front Spar

Considering only the front spar from Figure 2.8 and not including the foam inside it, the cross section is discretized using 336 elements for a total of 2448 d.o.f., and the corresponding VABS-A results are presented in Table 2.7, along with the ones based on

the thin-walled formulation of Ref. [4]. In addition, results for VABS-A modeling the foam inside the spar with a total of 393 elements (2709 d.o.f.) are included (the formulation of Ref. [4] is limited to thin-walled sections, and therefore cannot represent the foam). From these results, one can see that there is a good correlation between the thin-walled approximation and the present formulation on the stiffness constants as well as on the actuation constants. The discrepancies are within the expected range and are associated with the extra restriction of thin-walled beams in Ref. [4]. Also, the inclusion of the foam in the model has some effect on stiffening the structure and, consequently, increasing the actuation twist moment $M_1^{(a)}$ and reducing the actuation force $F_1^{(a)}$. However the effects are small and do not change the resulting induced twist rate (see Figure 2.11).

Table 2.6 Material properties used in the ATR prototype blade (Q_{ij} are the laminate reduced stiffnesses of the actuator pack—“L” direction is along the fibers and “N” is normal to the laminate).

E-Glass (Style 120 Fabric)	E_L (GPa)	19.3
	E_T (GPa)	19.3
	G_{LT} (GPa)	4.1
	ν_{LT}	0.148
	Ply thickness (mm)	0.114
S-Glass (Uni-tape)	E_L (GPa)	43.4
	E_T (GPa)	12.0
	G_{LT} (GPa)	3.6
	ν_{LT}	0.28
	Ply thickness (mm)	0.229
AFC (PZT-5H)	Q_{11} (GPa)	33.6
	Q_{12} (GPa)	7.54
	Q_{22} (GPa)	16.6
	Q_{66} (GPa)	5.13
	d_{11} (pm/V)	309
	d_{12} (pm/V)	-129
	Ply thickness (mm)	0.203
Foam (Rohacell 71)	E	90.0
	G	28.0

Experimental tests were conducted on this spar for torsional stiffness and twist actuation, and results are presented in Figures 2.9 and 2.10, respectively. As one can see from Figure 2.9, the thin-walled approximation (Ref. [4]) correlates well with a more complete analysis presented by VABS-A (labeled as “VABS-A w/o foam”), but both are about 20% lower than the experimental result. By incorporating more details on the model (the first one being the effect of the foam), the result from VABS-A shows a much better correlation with the experimental result, with a discrepancy of about 11% (notice that the experimental result has a variation of $\pm 5\%$ [41]). This indicates that VABS-A is capable of processing the details that will improve the representation of the structure. For further improvements, components like the ballast weights on the nose and web should be included and this is beyond the scope of the present work.

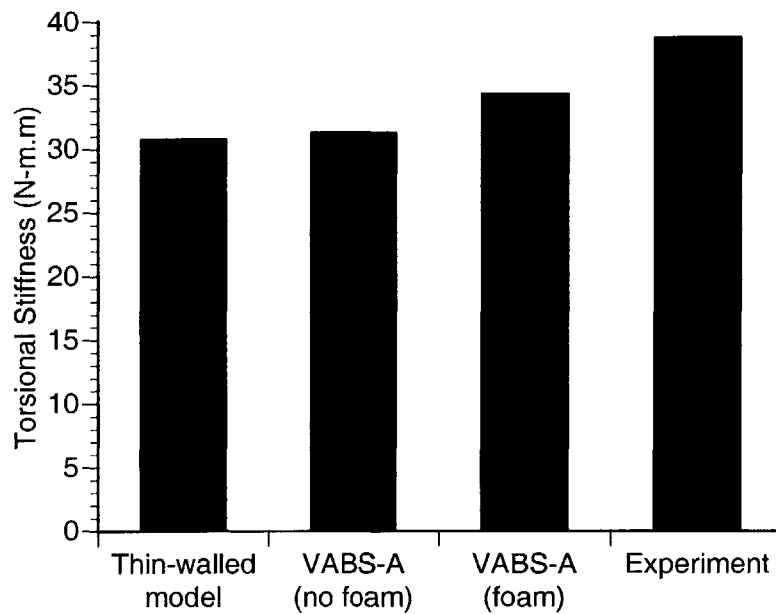


Figure 2.10 Torsional stiffness results for the ATR spar (only)-Experimental result has $\pm 5\%$ deviation.

Regarding the actuation due to induced twist deformation, Figure 2.11 shows the results for the ATR spar for a 2000 Vpp excitation. Due to a series of electrical difficulties with the AFC packs [41], the bar labeled “Experiment” are extrapolated results considering that all packs would be working. As one can see, all three theoretical results are basically the same, and the inclusion of the foam does not affect the actuation

twist rate. However, all of the theoretical results are basically two-times higher than the measured experimental result. The exact reason of the discrepancy is still under investigation, and this makes a further comparison with this data extremely hard. There are few things, however, that could help understand this discrepancy.

Table 2.7 Non-zero stiffness and actuation constants for ATR spar (N, N m, N m² for stiffness constants, and N/m, N m/m for the actuation constants).

	Ref.4	VABS-A w/o foam	VABS-A with foam
K_{11} (N)	1.637E+06	1.377E+06	1.416E+06
K_{12} (N m)	0.000E+00	2.454E+01	2.472E+01
K_{14} (N m)	4.007E+02	1.432E+03	2.480E+03
K_{22} (N m ²)	3.622E+01	3.131E+01	3.434E+01
K_{24} (N m ²)	0.000E+00	1.748E-02	8.202E-02
K_{33} (N m ²)	4.023E+01	3.681E+01	3.712E+01
K_{44} (N m ²)	1.020E+03	3.161E+02	3.249E+02
$F_1^{(a)}$ (N/m)	7.264E+01	6.935E+01	6.842E+01
$M_1^{(a)}$ (N m/m)	1.714E+00	1.572E+00	1.761E+00
$M_3^{(a)}$ (N m/m)	5.171E-01	-6.329E-02	-4.753E-03

First, the piezoelectric properties used for the predictions are based on a linearization at a higher field (with an applied voltage of 4000 Vpp) than the one possible to be reached in the experiments, and, therefore, overestimated. Also, the piezoelectric properties are characterized based on free strain conditions. It is still not known what non-linear force-stroke characteristics these new AFCs present, and preliminary indications show that they can potentially be large. Finally, due to a sequence of pack failures in the actual prototype blade (only 19 out of the original 24 were working after a sequence of bench tests), it is possible that some packs lost their original electric properties, causing a degraded overall performance.

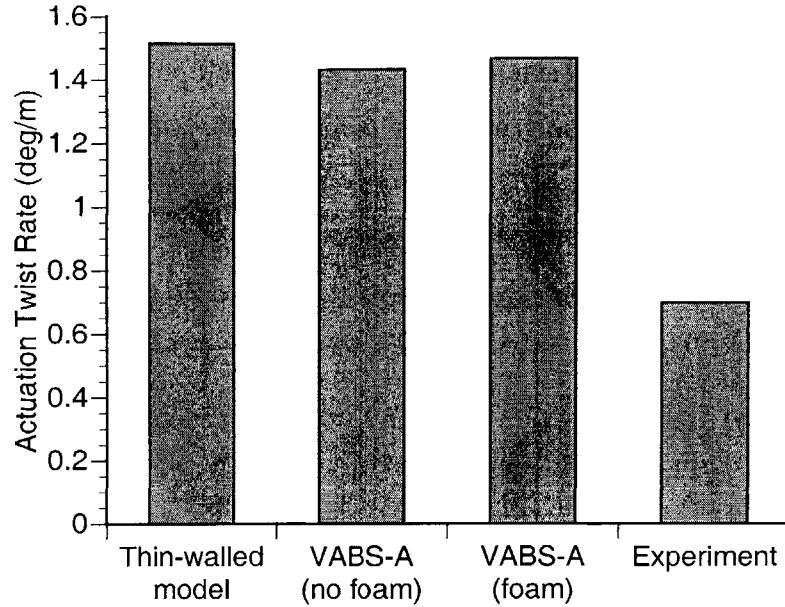


Figure 2.11 Actuation twist rate results for the ATR spar (only) for a 2000 Vpp.

2.2.4.3.2 Full Blade

The complete ATR cross section was discretized with 604 elements for a total of 4851 d.o.f. after adding the fairing to the spar described previously, without the core foam being modeled. For the case with the foam core in the model, a total of 789 elements (5691 d.o.f.) were used. The theoretical results for all the non-zero stiffness components and actuation constants are presented in Table 2.8.

As one can see, these results follow similar trends to the isolated spar. Particularly, the torsional stiffness correlation when foam is added to the model improves significantly, and the difference between experimental and theoretical results is approximately 5% (see Figure 2.12).

Table 2.8 Non-zero stiffness and actuation constants for ATR prototype full blade (N, N m, N m² for stiffness constants, and N/m, N m/m for the actuation constants).

	Ref.4	VABS-A w/o foam	VABS-A with foam
K_{11} (N)	1.637E+06	1.633E+06	1.712E+06
K_{12} (N m)	0.000E+00	2.467E+01	2.694E+01
K_{14} (N m)	4.007E+02	6.487E+02	2.023E+04
K_{22} (N m ²)	3.622E+01	3.684E+01	4.277E+01
K_{24} (N m ²)	0.000E+00	1.780E-01	5.478E-01
K_{33} (N m ²)	4.023E+01	4.078E+01	4.136E+01
K_{44} (N m ²)	1.020E+03	9.735E+02	1.279E+03
$F_1^{(a)}$ (N/m)	7.264E+01	6.931E+01	6.844E+01
$M_1^{(a)}$ (N m/m)	1.714E+00	1.654E+00	1.940E+00
$M_3^{(a)}$ (N m/m)	5.171E-01	4.575E-01	1.289E+00

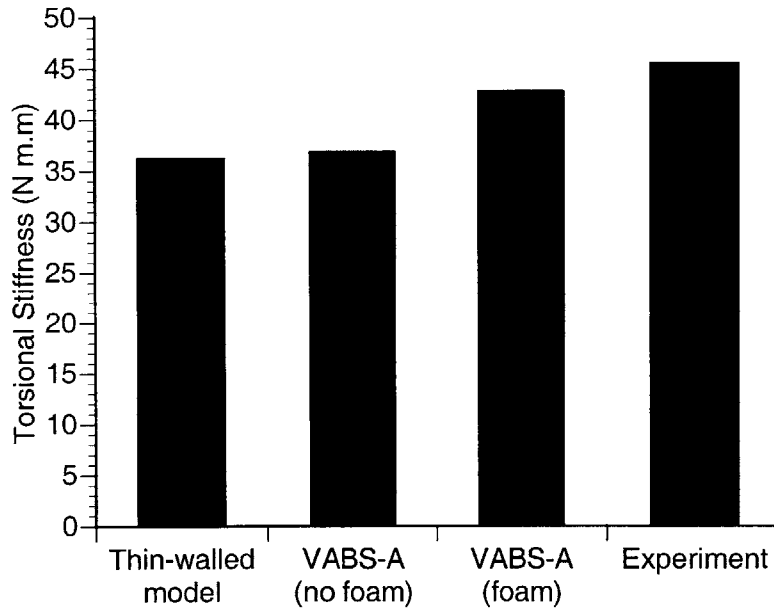


Figure 2.12 Torsional stiffness results for the complete ATR blade-Experimental results has $\pm 5\%$ deviation.

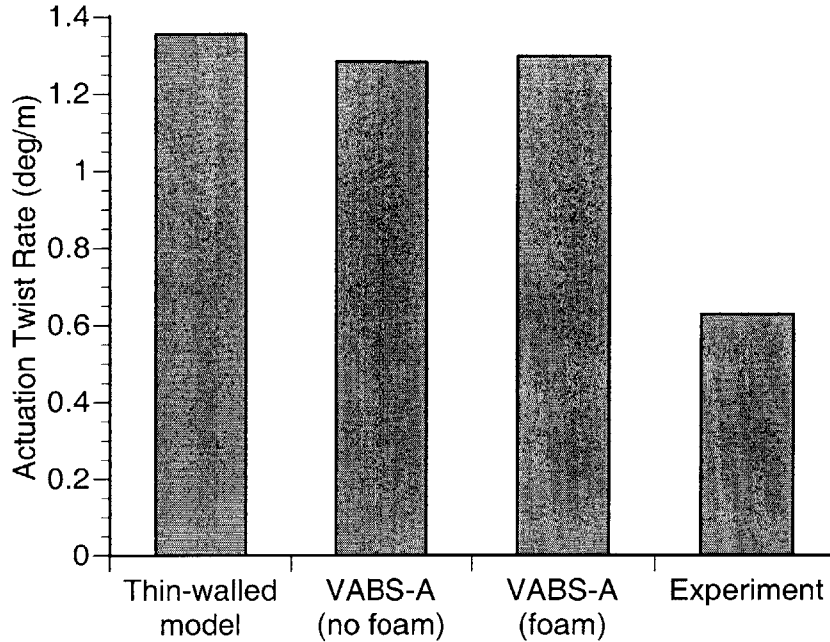


Figure 2.13 Actuation twist rate results for the complete ATR blade.

The twist actuation results are shown in Figure 2.13, and the exact cause of discrepancy between the theoretical results and the experimental one is still under investigation (see discussion above for the ATR spar).

A remarkable result is that, even though the foam affects the stiffness and actuation constants, it does not (theoretically) change much the induced (active) twist rate. The mechanism for this to happen is for the foam to be compliant compared to the walls, such that the “local stiffness” on the active part of the structure is not significantly changed (mathematical discussion on this issue is presented in Ref [42]). A graphical way of seeing this is by looking at the warping mode associated with the actuation, $V_0^{(a)}$, defined in Eq (2.51). The result of the warping modes associated with extension, torsion, two bendings, and the actuation are shown in Figures 2.14 and 2.15 for the models without foam and including foam, respectively. As one can see, they are virtually the same, particularly the two main warping modes for this actuation mechanism, namely the torsional warping (mode 2) and the actuation warping (mode 5).

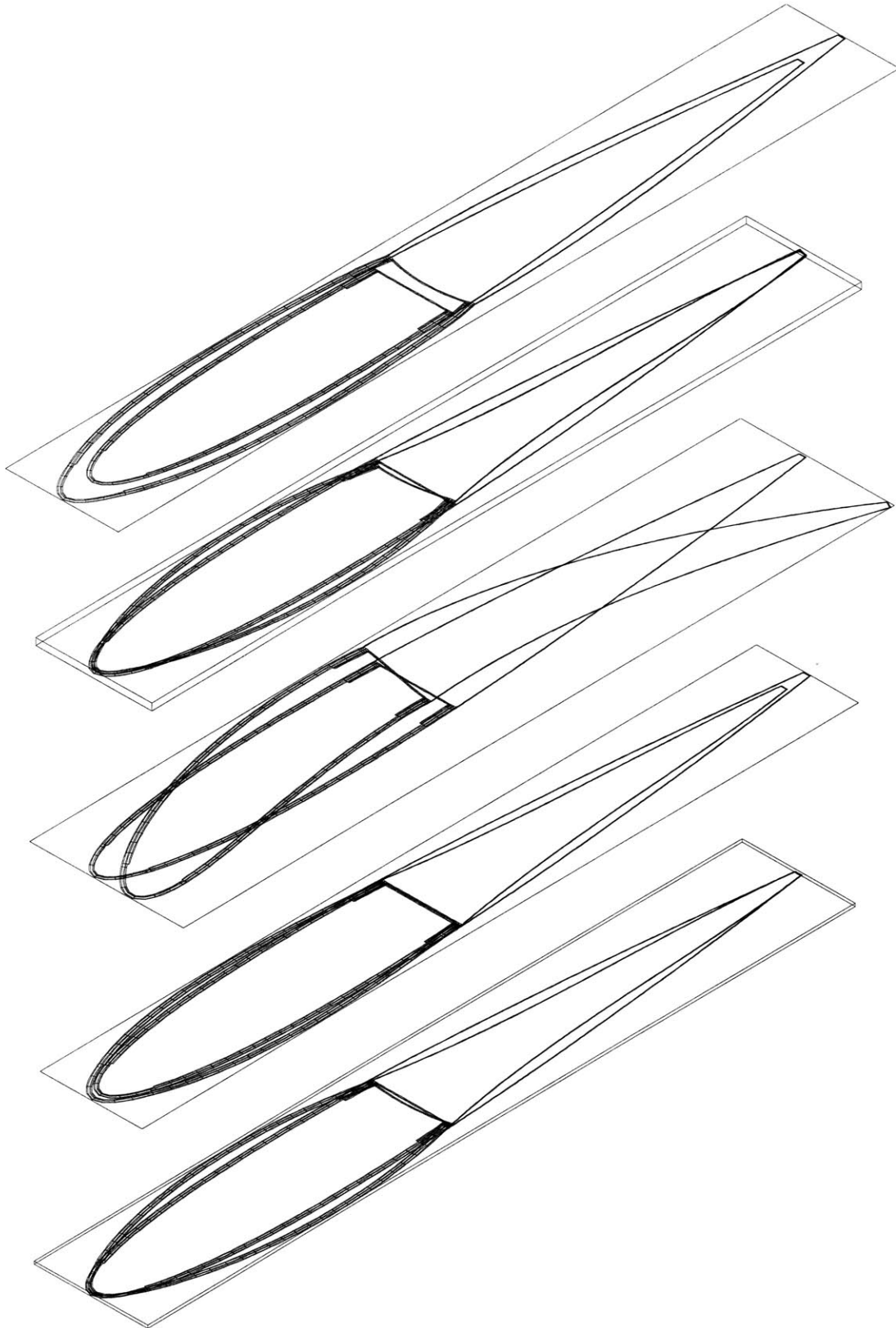


Figure 2.14 Warping modes for the ATR blade model *without including* the foam core (different magnifications were used to facilitate visualization).

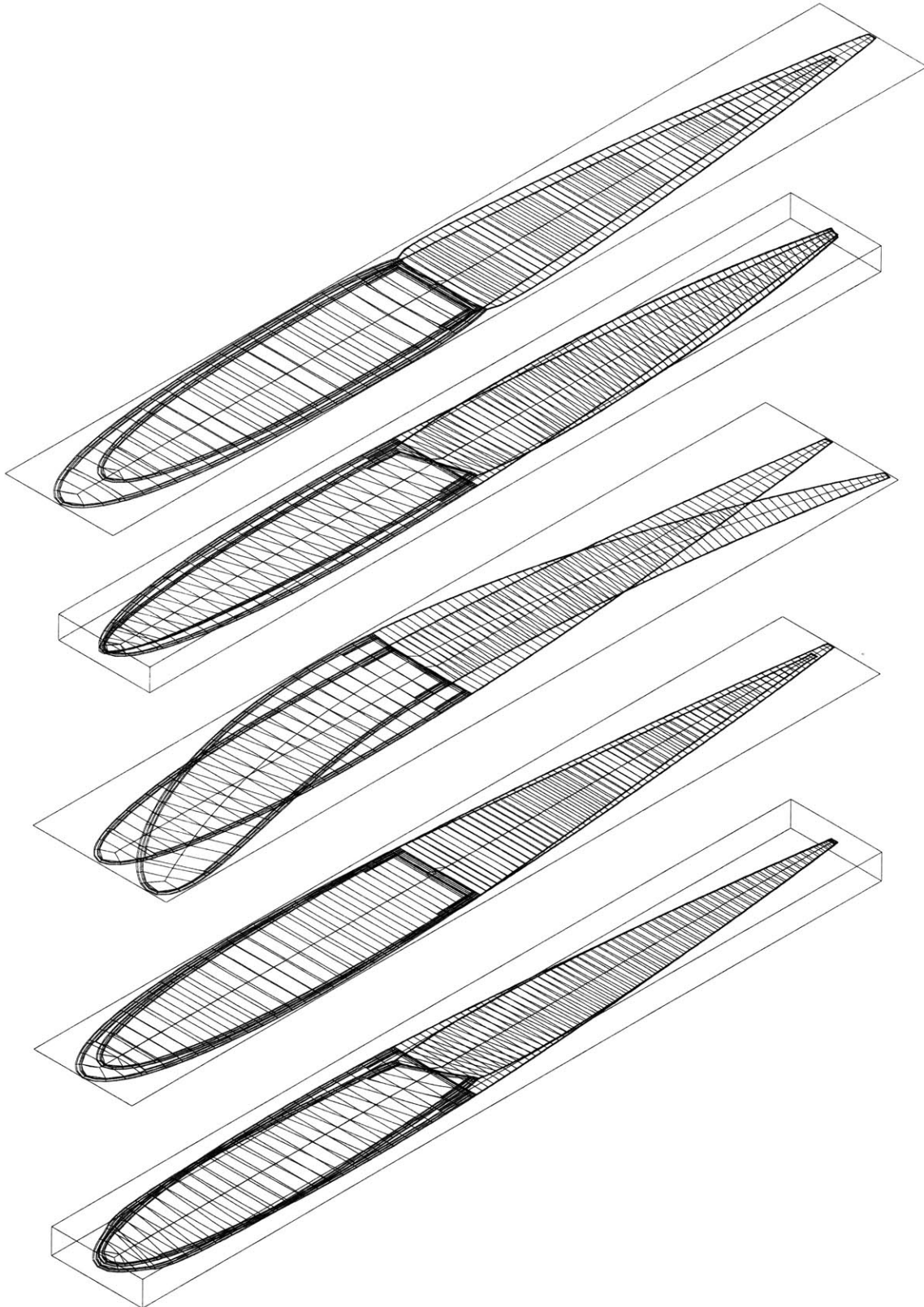


Figure 2.15 Warping modes for the ATR blade model *including* the foam core (different magnifications were used to facilitate visualization).

2.2.4.4 Mach-Scaled CH47-D Active Blade Section

Finally, consider the 1/6th Mach scaled CH-47D blade built and tested at MIT [39]. Particularly, let us consider the blade section that runs from the root to 0.54 radius as shown in Figure 2.16 (along with the detailed cross-section layup).

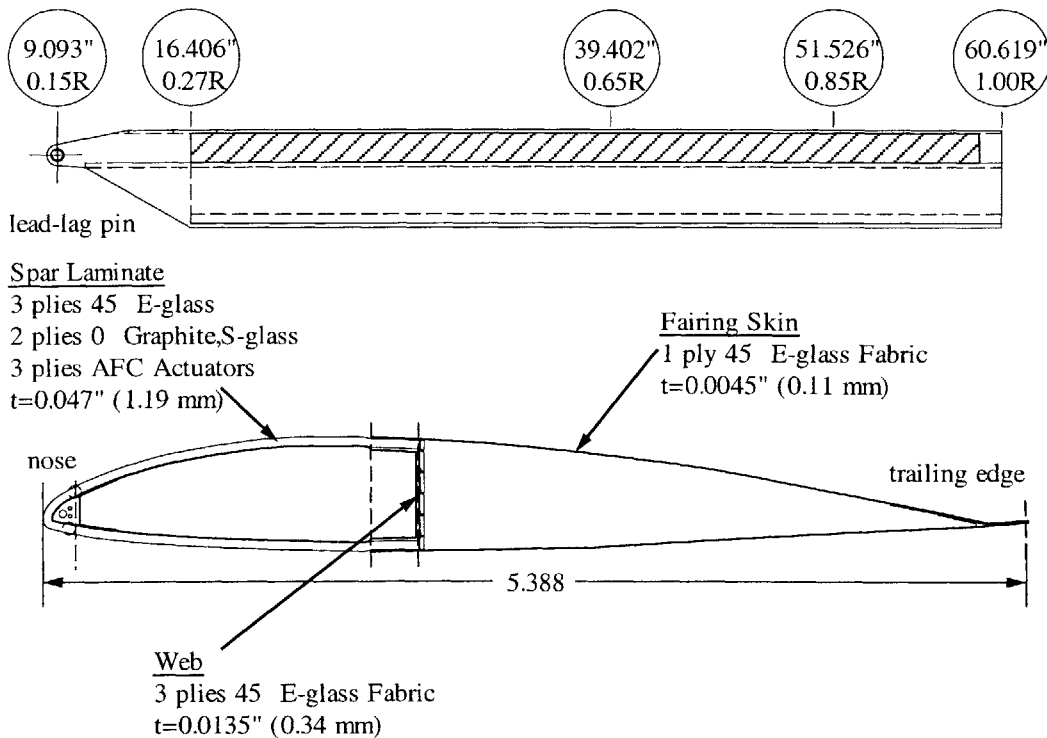


Figure 2.16 1/6th Mach-scaled active CH47-D blade

Similar to the ATR blade described above, the CH-47D blade section was built in two steps so one had access to first test the front D-spar and once the fairing was attached, the full blade. Both cells are filled with foam, being Rohacell 300 WF (high density/high strength foam) for the front D-spar, and Rohacell 71 IG for the fairing. The experimental setup, and blade material properties are described in details in Ref. [39]. The maximum twist at the end (0.54R) was measured corresponding to a maximum applied voltage of $4000 V_{pp}$ and only 10 out of the 12 packs working. Active twist rate results of the experimental test, the theoretical thin-walled analyses of Refs. [10] and [4], and the present analysis are presented in Table 2.9. For VABS-A results, a finite element mesh with 629 elements (4299 d.o.f.) for the D-spar and with 827 elements (6252 d.o.f.)

for the full blade were used. The foam could not be modeled for this case due to limitations on the automatic mesh generator for the interior regions when dealing with non-symmetric airfoils.

Table 2.9 Peak-to-peak twist actuation results for the 1/6th Mach-scaled CH47-D active blade-based on 54% span and $4000 V_{PP}/800 V_{DC}$

	D-Spar Only	D-Spar+Fairing
Ref.4	3.13 deg/m	2.65 deg/m
Ref.10	3.13 deg/m	-
VABS-A	3.05 deg/m	2.25 deg/m
Experiment	2.46 deg/m	2.06 deg/m

As one can see, all the theoretical results overpredict the twist actuation, particularly in the case of the isolated spar. But better than the other ones, VABS-A captures the spar tip twist actuation within 24% and the full blade within 10%, which is a remarkable correlation, even if by including the foam the tip twist actuation may not change much. Due to the flexibility of the finite-element formulation, more details could have been added to the model in order to more realistically represent the blade. This, however, is not a trivial task for an automatic mesh generator, and future mesh generation for this particular configuration could be done in a CAD environment. Then one could conclude on the influence of the foam core, flex circuit, ballast weight, and other construction details of the blade on the actuation performance.

Chapter 3

Aeroelastic Control Design

This chapter addresses a particularly challenging task for the aeroelastician: the control of the aerodynamic surface. Every element that shapes the control problem within the aeroelastic framework as introduced in Chapter 1 is presented next. The LQR is introduced first as a fundamental building block of the LQG. The LQG is more realistic than the LQR and is presented after. The appropriate formulation necessary to introduce the sensing as well as the disturbance into the model are presented next. Finally, several useful tools to help the designer in identifying the working point of the wing as well as tools to quantify that performance close up the chapter.

3.1 The LQR Regulator

The Linear Quadratic Regulator (LQR) is presented hereafter as a basic element of the Linear Quadratic Gaussian Regulator (LQG), which is the subject of the following section. The LQR in its own is useful to determine a design weight *a priori*, as is described in detail later on.

Figure 3.1 shows the schematics of the LQR regulator. The state space formulation that describes the plant is the following:

$$\dot{x}(t) = A \cdot x(t) + B \cdot u_e(t) \quad (3.1)$$

where x is the state vector and u_e is the input to the plant. In essence, the LQR provides a control vector $u(t)$ such that a given performance index J is minimized:

$$J = \int_0^{\infty} L(x, u) dt \quad (3.2)$$

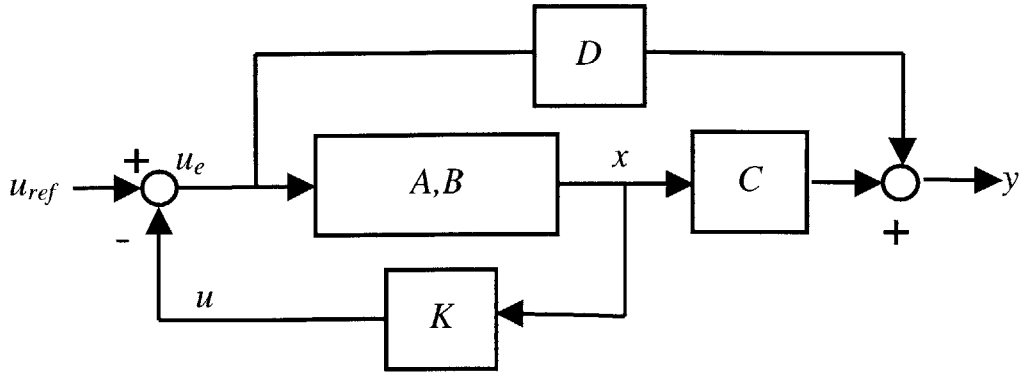


Figure 3.1 Linear Quadratic Regulator (LQR) Diagram

A usual choice is [57]

$$J = \int_0^{\infty} (x^T \cdot Q \cdot x + u^T \cdot R \cdot u) dt \quad (3.3)$$

where R and Q are positive-definite Hermitian matrices. This poses a least-squares minimization problem, which results in the input related to the state vector through a constant gain matrix K :

$$u(t) = -K \cdot x(t) \quad (3.4)$$

The matrix K is found by solving

$$K = R^{-1} B^T P \quad (3.5)$$

where P is the solution of the following Riccati equation:

$$A^T \cdot P + P \cdot A - P \cdot B \cdot R^{-1} \cdot B^T \cdot P + Q = 0 \quad (3.6)$$

The state space representation of the complete general system (i.e., plant plus regulator) is given by

$$\begin{aligned} \dot{x} &= A \cdot x + B \cdot u_e \\ y &= C \cdot x + D \cdot u_e \end{aligned} \quad (3.7)$$

where $u_{ref} - u = u_e$. The regulator expressed by Eq. (3.4) can be rewritten as

$$u_e = u_{ref} - K \cdot x \quad (3.8)$$

Substituting Eq. (3.8) into Eq. (3.7) results in

$$\begin{aligned}\dot{x} &= A \cdot x + B \cdot (u_{ref} - K \cdot x) \\ y &= C \cdot x + D \cdot (u_{ref} - K \cdot x)\end{aligned}\tag{3.9}$$

or after regrouping terms,

$$\begin{aligned}\dot{x} &= (A - B \cdot K) \cdot x + B \cdot u_{ref} \\ y &= (C - D \cdot K) \cdot x + D \cdot u_{ref}\end{aligned}\tag{3.10}$$

which is the global state space representation sought, with the new stability matrix

$$\bar{A} = A - B \cdot K\tag{3.11}$$

The LQR may seem a reasonable closed-loop regulator, but unfortunately it is far from being optimal in a real flying wing scenario. In particular, the LQR

- assumes that the complete state vector x is known for feedback,
- has no knowledge of any disturbance affecting the system nor does it account for one in its formulation, and
- does not take into account any noise in the sensing or affecting the states, or the sensor readings.

With these limitations in mind, another type of regulator must be used for the problem under consideration in this thesis.

3.2 The LQG Regulator

The Linear Quadratic Gaussian regulator (LQG) does not have the shortcomings of the LQR, providing a much more realistic controller in a model where arbitrary discrete sensing is present. It accounts for random noise (w) as shown in the block diagram in Figure 3.2.

The state space equation that describes the plant is now

$$\begin{aligned}\dot{x}(t) &= A \cdot x(t) + B \cdot u_e(t) + G \cdot w(t) \\ y(t) &= C \cdot x(t) + D \cdot u_e(t) + H \cdot w(t) + v(t)\end{aligned}\tag{3.12}$$

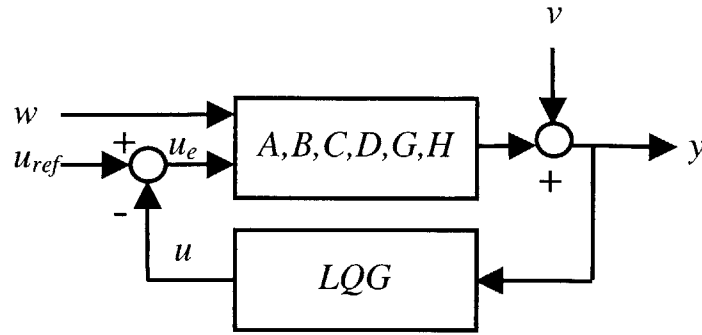


Figure 3.2 Linear Quadratic Gaussian Diagram

where x is the state vector, u_e is the input to the plant, w is the process noise and v is the disturbance noise. w and v are zero mean white noise processes with uncorrelated spectral density matrices Q and R .

As mentioned above, this is a more realistic scenario in which there is no complete knowledge of the plant states. The LQG combines a LQR with a Kalman filter to estimate those states based on measurements affected by noise. The estimation algorithm satisfies two criteria:

- The expected value of the estimate is equal to the expected value of the state;
- The estimation algorithm minimizes the expected value of the square of the estimation error.

The dynamics of the estimation state \hat{x} yielded by the Kalman filter are equal to

$$\dot{\hat{x}} = A \cdot \hat{x} + B \cdot u_e + L \cdot (y - C \cdot \hat{x} - D \cdot u) \quad (3.13)$$

where L is equal to

$$L = P \cdot C^T \cdot R^{-1} \quad (3.14)$$

and P is obtained by solving the Riccati equation

$$\dot{P} = A \cdot P + P \cdot A^T + G \cdot Q \cdot G^T - P \cdot C^T \cdot R^{-1} \cdot C \cdot P \quad (3.15)$$

The Kalman filter can then be expressed in state space formulation as

$$\begin{aligned}\dot{\hat{x}} &= [A - L \cdot C - (B - L \cdot D) \cdot K] \cdot \hat{x} + L \cdot y \\ \hat{y} &= -C \cdot \hat{x} + D \cdot u\end{aligned}\quad (3.16)$$

The LQG regulator is formed by combining the Kalman filter with the constant gain matrix K obtained in the LQR regulator, which satisfies

$$u = -K \cdot \hat{x} \quad (3.17)$$

The state space formulation of the regulator can then be obtained by combining Eqs. 3.16 and 3.17:

$$\begin{aligned}\dot{\hat{x}} &= A_K \cdot \hat{x} + B_K \cdot y \\ u &= -C_K \cdot \hat{x} - D_K \cdot y\end{aligned}\quad (3.18)$$

Substituting the second equation in Eq. (3.12) in the second one in Eq. (3.18) and assuming the reference input u_{ref} equal to zero results in

$$u = -C_K \cdot \hat{x} - D_K \cdot C \cdot x - D_K \cdot D \cdot u - D_K \cdot H \cdot w \quad (3.19)$$

This result is substituted in the first equation in Eq (3.12), yielding

$$\begin{aligned}\dot{x} &= A \cdot x - B \cdot C_K \cdot \hat{x} - B \cdot D_K \cdot C \cdot x - B \cdot D_K \cdot D \cdot u - B \cdot D_K \cdot H \cdot w + G \cdot w \\ \dot{\hat{x}} &= (A - B \cdot D_K \cdot C) \cdot x - (B \cdot C_K) \cdot \hat{x} - (B \cdot D_K \cdot D) \cdot u + (G - B \cdot D_K \cdot H) \cdot w\end{aligned}\quad (3.20)$$

Similarly, the second equation in Eq. (3.12) is substituted in the first equation in Eq. (3.18) to obtain

$$\dot{\hat{x}} = A_K \cdot \hat{x} + B_K \cdot C \cdot x + B_K \cdot D \cdot u + B_K \cdot H \cdot w \quad (3.21)$$

All there is left to be done for the new matrices A and B is to write Eqs. (3.20) and (3.21) in state space form:

$$\begin{Bmatrix} \dot{x} \\ \dot{\hat{x}} \end{Bmatrix} = \begin{bmatrix} A - B \cdot D_K \cdot C & -B \cdot C_K \\ B_K \cdot C & A_K \end{bmatrix} \cdot \begin{Bmatrix} x \\ \hat{x} \end{Bmatrix} + \begin{bmatrix} -B \cdot D_K \cdot D \\ B_K \cdot D \end{bmatrix} \cdot u + \begin{bmatrix} G - B \cdot D_K \cdot H \\ B_K \cdot H \end{bmatrix} \cdot w \quad (3.22)$$

For matrices C and D a similar procedure is followed. Eq. (3.19) is substituted in the second equation in Eq. (3.12) and written in state space form yielding

$$y = [C - D_K \cdot C \quad -D \cdot C_K] \cdot \begin{Bmatrix} x \\ \hat{x} \end{Bmatrix} - (D \cdot D_K \cdot D) \cdot u + (H - D \cdot D_K \cdot H) \cdot w \quad (3.23)$$

Finally, rearranging Eqs. 3.22 and 3.23, the complete system (plant plus regulator) can be written as

$$\begin{aligned}
\begin{Bmatrix} \dot{x} \\ \dot{\hat{x}} \end{Bmatrix} &= \begin{bmatrix} A - B \cdot D_K \cdot C & -B \cdot C_K \\ B_K \cdot C & A_K \end{bmatrix} \cdot \begin{Bmatrix} x \\ \hat{x} \end{Bmatrix} + \begin{bmatrix} G - B \cdot D_K \cdot H & -B \cdot D_K \cdot D \\ B_K \cdot H & B_K \cdot D \end{bmatrix} \begin{Bmatrix} w \\ u \end{Bmatrix} \\
y &= [C - D_K \cdot C \quad -D \cdot C_K] \cdot \begin{Bmatrix} x \\ \hat{x} \end{Bmatrix} - \begin{bmatrix} H - D \cdot D_K \cdot H \\ D \cdot D_K \cdot D \end{bmatrix} \begin{Bmatrix} w \\ u \end{Bmatrix}
\end{aligned} \tag{3.24}$$

3.3 Structural and Aerodynamic Modes

Knowledge of the structural and aerodynamic modes is key to the design. Firstly, it allows to determine which two modes coalesce in flutter. Secondly, it establishes the most critical gust frequency the wing will encounter at any configuration. And thirdly, it provides the essential information for optimal sensor placement.

The structural and the aerodynamic modes result from solving the following eigenvalue problem:

$$Ax = \mu x \tag{3.25}$$

where A is the corresponding matrix in the state space formulation as in Eq. (3.12), and x is the state vector as in Eq. (2.25). A useful way to present the resulting eigenvectors is to plot them in terms of the wing displacements u and rotations θ and the inflow states λ rather than in their original state representation $x = f(\theta, \dot{\theta}, \lambda)$. The following steps accomplish this.

The cross-sectional strain γ is defined as

$$\gamma = \begin{Bmatrix} \gamma_{11} \\ 2\gamma_{12} \\ 2\gamma_{13} \end{Bmatrix} \tag{3.26}$$

It is a function of the rotations θ and the displacements u , which can be represented as

$$\gamma = f(u, \theta) = 0 \Rightarrow u = f(\theta) \tag{3.27}$$

Once these equations are linearized (assuming small deformations) and the extensional strain is neglected, the displacements can be expressed in terms of the rotations as

$$\begin{aligned}
u_1^i &= 0 \\
(u_3^{i+1} - u_3^i) &= -\frac{\Delta l}{2}(\theta_2^i + \theta_2^{i+1}) \\
(u_2^{i+1} - u_2^i) &= \frac{\Delta l}{2}(\theta_3^i + \theta_3^{i+1})
\end{aligned} \tag{3.28}$$

where the subscripts are the direction of u or θ and the superscripts stand for the finite element number of the discretization. Δl is the distance between contiguous elements in the discretization. This allows to write the displacements as a function of the Rodrigues parameters:

$$u = T_{u\theta} \cdot \theta \tag{3.29}$$

where $T_{u\theta}$ is the matrix mapping the rotations to the displacements. The conversion can be completed then as

$$\begin{Bmatrix} u \\ \theta \\ \lambda \end{Bmatrix} = \begin{bmatrix} T_{u\theta} & 0 & 0 \\ I & 0 & 0 \\ 0 & 0 & I \end{bmatrix} \begin{Bmatrix} \theta \\ \dot{\theta} \\ \lambda \end{Bmatrix} \tag{3.30}$$

The structural modes can be visualized by plotting u and θ . The aerodynamic modes can be visualized by plotting λ . This has been done in Matlab and actual examples of the output are presented in Chapter 4.

3.4 Sensing

The two types of sensor that are considered in the wing are introduced in this section, along with the equations that allow their modeling in the state space formulation. The best placement of the sensors is treated next.

3.4.1 Sensor Types

As mentioned above, there are two kinds of sensors considered in this study. The first type, the strain gauge, provides local strain information. The other type, the accelerometer, provides kinetic information. These two sensors are small enough in their real form to be attached to a wing, which allows their distribution along the structure in

high numbers if necessary. The best placement of the sensing devices is studied in later sections.

Strain gauges: The strain gauges measure the local strain in the direction of the gauge. Clever placement and orientation of the strain gauges can allow for bending or torsional curvature measurements. It is shown here how to obtain the bending curvature from the placing of two gauges at 0° (the same holds for the twist curvature placing the two strain gauges at $\pm 45^\circ$).

Figure 3.3 shows a longitudinal section (along the beam axis, x_1) of a beam and two strain gauges, one on the top and the other on the bottom.

From elasticity theory, the curvature measured by each of the gauges can be written as

$$\begin{aligned}\epsilon_{1u} &= -\kappa_2 \cdot h_1 \\ \epsilon_{1l} &= \kappa_2 \cdot h_2\end{aligned}\tag{3.31}$$

where ϵ denotes the strain, κ the curvature and h_1 and h_2 the distance from the neutral axis to the top and bottom of the section respectively.

Combining these two equations results in

$$\epsilon_{1l} - \epsilon_{1u} = \kappa_2 \cdot (h_2 + h_1)\tag{3.32}$$

Since h_2+h_1 is a known quantity, the curvature can be expressed in terms of the strain measured by the gauges:

$$\kappa_2 = \frac{\epsilon_{1l} - \epsilon_{1u}}{h_2 + h_1}\tag{3.33}$$

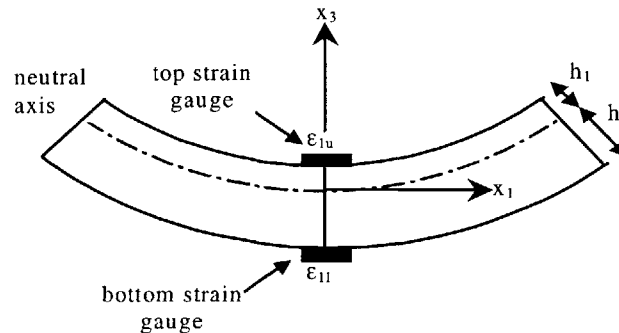


Figure 3.3 Placement of two strain gauges at 0° in a non-symmetric longitudinal cross-section

Accelerometers: Differentiating Eq. (3.29) twice yields

$$\ddot{u} = T_{u\theta} \cdot \ddot{\theta} \quad (3.34)$$

The only thing left to know is how to express $\ddot{\theta}$ in terms of the state vector x , the input u and the disturbance w . From the reduced state space representation, the following equation holds:

$$\begin{Bmatrix} \dot{\theta} \\ \ddot{\theta} \\ \dot{\lambda} \end{Bmatrix} = \begin{bmatrix} A_1 \\ A_2 \\ A_3 \end{bmatrix} \begin{Bmatrix} \theta \\ \dot{\theta} \\ \lambda \end{Bmatrix} + \begin{bmatrix} B_1 \\ B_2 \\ B_3 \end{bmatrix} u + \begin{bmatrix} G_1 \\ G_2 \\ G_3 \end{bmatrix} w \quad (3.35)$$

Then,

$$\ddot{\theta} = A_2 \cdot \begin{Bmatrix} \theta \\ \dot{\theta} \\ \lambda \end{Bmatrix} + B_2 \cdot u + G_2 \cdot w \quad (3.36)$$

Combining Eqs. (3.34) and (3.36) yields

$$\ddot{u} = T_{u\theta} \cdot A_2 \cdot \begin{Bmatrix} \theta \\ \dot{\theta} \\ \lambda \end{Bmatrix} + T_{u\theta} \cdot B_2 \cdot u + T_{u\theta} \cdot G_2 \cdot w \quad (3.37)$$

which expresses the acceleration in terms of x , u and w .

All the sensor information is written to a file that the Matlab implementation then reads. This file has as many entries as elements in the wing discretization. For every element, a series of three flags tells which type of sensor (bending strain gauge, torsion strain gauge or accelerometer, or a combination of the three) is embedded in the element.

3.4.2 Sensor Placement

Knowledge of the different structural modes is key to the sensible placement of the gauges. There are two kinds of sensors: accelerometers and strain gauges. In order to increase modal observability, the sensors have been placed along the span after a modal analysis. The first three bending modes and the first three torsion modes can be computed for a wing. The shape of the mode indicates where the curvature of the structure (and hence the measured strain) is maximum. Placing the strain gauges at these maxima should provide enough information with a minimal set of gauges. The accelerometers

should be placed where the modal amplitude has a maximum. For the first bending mode, the best location should be the tip element, where the displacement (and therefore the acceleration) is greater.

A practical way to obtain the maximum curvature locations is to numerically derive the mode shape obtained as described in Section 3.3. The disadvantage of this direct approach is that the mode shapes obtained will be a simple linear interpolation of the discrete values associated with the relatively small number of nodes used in the finite element discretization of the wing. This is particularly problematic when one tries to numerically evaluate the second derivative of the nodes required for the curvature calculation. To overcome this problem, an approximation to the modes can be computed using the influence coefficients of a cantilever wing both for bending and torsion. Refer to Appendix B for a detailed explanation.

3.5 Gust model

The gust model adopted as the system disturbance w is a simple harmonic disturbance embedded in the atmosphere described in Refs. [50] and [45] as

$$w = \frac{w_{\max}}{2} \left[1 - \cos\left(\frac{2\pi(-U_{\infty}t)}{x_G}\right) \right] \quad (3.38)$$

where U_{∞} is the flight speed. Figure 3.4 more clearly describes the model and the different parameters.

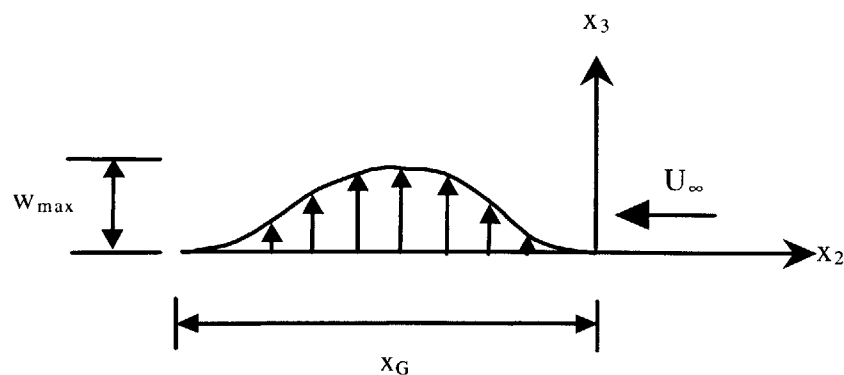


Figure 3.4 1-Cosine gust model

When the undisturbed wing encounters this disturbance model, it begins to oscillate. For a stable system, once it has advanced through the gust, it settles down in some time which is one of the performance parameter used to evaluate gust alleviation.

3.6 Cost Calculation and Normalization

It is intuitive that different actuation and sensor configurations in a wing result in different performances. What is more: a certain actuation distribution may effectively reduce excessive wing displacements at the expense of higher power consumption. Clearly, a way to normalize actuation and response is necessary in order to compare different configurations. The concept that is to be introduced next provides a consistent way to compare the performance of different configurations.

3.6.1 Formulation

A rational way to evaluate the performance is by normalizing the cost minimization functional presented in Eq. (3.3) and which is written again with an additional weighting term ρ :

$$J = \int_0^{\infty} (x^T \cdot Q \cdot x + \rho \cdot u^T \cdot R \cdot u) dt \quad (3.39)$$

There are two contributors to this cost function: the *state* cost (J_s) and the *control* cost (J_c):

$$J_s = \int_0^{\infty} (x^T \cdot Q \cdot x) dt \quad (3.40)$$

$$J_c = \int_0^{\infty} (u^T \cdot R \cdot u) dt \quad (3.41)$$

Defining Q as

$$Q = \begin{bmatrix} M & 0 \\ 0 & K \end{bmatrix} \quad (3.42)$$

results in the state cost being the integral with respect to time of the total energy of the

system, i.e., strain energy and kinetic energy. The control cost happens to be the actuation input to the system integrated over time.

3.6.1.1 Cost Functions for a LQR Regulator

A way to compute the improper integrals in Eqs. (3.40) and (3.41) has to be devised in order for the whole normalization procedure to be implemented on a digital computer. The method uses the Lyapunov equation.

The Lyapunov's Second Method studies the asymptotic stability of $\dot{x} = A \cdot x$ (Ref. [49]). If A and x are real, then a positive-definite Hermitian matrix P is chosen and the following function V is defined:

$$V(x) = x^T \cdot P \cdot x \quad (3.43)$$

The time derivative of the function is then

$$\dot{V}(x) = (A \cdot x)^T \cdot P \cdot x + x^T \cdot P \cdot (A \cdot x) = x^T \cdot (A^T \cdot P + P \cdot A) \cdot x = \dot{x}^T \cdot P \cdot x + x^T \cdot P \cdot \dot{x} \quad (3.44)$$

The following matrix \bar{Q} is also defined:

$$\bar{Q} = -(A^T \cdot P + P \cdot A) \quad (3.45)$$

and then $\dot{V}(x)$ becomes

$$\dot{V}(x) = -x^T \cdot Q \cdot x \quad (3.46)$$

For asymptotic stability $\dot{V}(x)$ is required to be negative definite (since $V(x)$ was chosen as positive definite), or alternatively, Q has to be positive definite. In fact it is more practical to choose a positive-definite matrix Q and examine whether P is positive-definite from

$$A^T \cdot P + P \cdot A = -Q \quad (3.47)$$

Eq. (3.47) is the *Lyapunov Matrix Equation*. The matrices A and Q have to be determined next so that the Lyapunov equation matches the present problem. A state space representation of a plant with full state feedback is given by

$$\begin{aligned} \dot{x} &= A \cdot x + B \cdot u \\ u &= -K \cdot x \end{aligned} \quad (3.48)$$

which can be combined as

$$\dot{x} = A \cdot x - B \cdot K \cdot x = (A - B \cdot K) \cdot x \quad (3.49)$$

In other words, the A matrix sought, which is renamed \bar{A} , is equal to

$$\bar{A} = A - B \cdot K \quad (3.50)$$

The matrix Q is obtained by rewriting Eq. (3.39) using the last equation in Eq. (3.48) as follows:

$$J = \int_0^{\infty} (x^T \cdot Q \cdot x + u^T \cdot R \cdot u) dt = \int_0^{\infty} x^T \cdot (Q + K^T \cdot R \cdot K) \cdot x \cdot dt \quad (3.51)$$

By direct comparison between Eqs. (3.46) and (3.51), \bar{Q} is found to be

$$\bar{Q} = Q + K^T \cdot R \cdot K \quad (3.52)$$

and therefore, Eq. (3.47) (the Lyapunov matrix equation) can be written as

$$(A - B \cdot K)^T \cdot P' + P' \cdot (A - B \cdot K) = -(Q + K^T \cdot R \cdot K) \quad (3.53)$$

and P' can be obtained by solving this equation. Furthermore, the cost function can be written as

$$J = \int_0^{\infty} x^T \cdot (Q + K^T \cdot R \cdot K) \cdot x \cdot dt = -x^T \cdot P' \cdot x \Big|_0^{\infty} = -x^T(\infty) \cdot P' \cdot x(\infty) + x^T(0) \cdot P' \cdot x(0) \quad (3.54)$$

But since $x(\infty) \rightarrow 0$,

$$J = \int_0^{\infty} x^T \cdot (Q + K^T \cdot R \cdot K) \cdot x \cdot dt = x^T(0) \cdot P' \cdot x(0) = \text{trace}(x(0) \cdot x^T(0) \cdot P') \quad (3.55)$$

Similarly, we can also set up the Lyapunov equation using the identity matrix I instead of Q , which is completely valid because the only requirement is for Q to be positive-definite:

$$(A - B \cdot K)^T \cdot P + P \cdot (A - B \cdot K) = -I \quad (3.56)$$

In this case,

$$J_I = \int_0^{\infty} x^T \cdot I \cdot x \cdot dt = x^T(0) \cdot P \cdot x(0) = \text{trace}(x(0) \cdot x^T(0) \cdot P) \quad (3.57)$$

Multiplying Eq. (3.57) by $(Q + K^T \cdot R \cdot K)$ yields

$$\int_0^{\infty} x^T \cdot (Q + K^T \cdot R \cdot K) \cdot x \cdot dt = \text{trace}(x(0) \cdot x^T(0) \cdot P \cdot (Q + K^T \cdot R \cdot K)) \quad (3.58)$$

Comparing Eqs. (3.55) and (3.58) one obtains

$$P' = P \cdot (Q + K^T \cdot R \cdot K) \quad (3.59)$$

There are several LQR-like controllers designs that include gust, but how to consistently include it is unclear. There is one based on the assumption of a white noise disturbance to the system (with no gust state equation) [47]. For this model, the cost function J for the white noise disturbance is written independently of any initial conditions:

$$J = \text{trace}(P') \quad (3.60)$$

Similarly, using the result in Eq. (3.59),

$$J = \text{trace}(P \cdot (Q + K^T \cdot R \cdot K)) \quad (3.61)$$

$$J_s = \text{trace}(P \cdot Q) \quad (3.62)$$

$$J_c = \text{trace}(P \cdot K^T \cdot R \cdot K) \quad (3.63)$$

3.6.1.2 Cost Functions for a LQG Regulator

Using a similar derivation to the one employed above for a LQR regulator, the different costs can be calculated as

$$J = \text{trace}(P_2 \cdot Q + P_1 \cdot P_2 \cdot \sigma_2 \cdot P_2) \quad (3.64)$$

$$J_s = \text{trace}((P_2 + P_3) \cdot Q) \quad (3.65)$$

$$J_c = \text{trace}(P_3 \cdot P_1 \cdot \sigma_1 \cdot P_1) \quad (3.66)$$

where P_1 and P_2 result from solving the following Riccati equations

$$A^T \cdot P_1 + P_1 \cdot A - P_1 \cdot \sigma_1 \cdot P_1 + Q = 0 \quad (3.67)$$

$$A \cdot P_2 + P_2 \cdot A^T - P_2 \cdot \sigma_2 \cdot P_2 + G = 0 \quad (3.68)$$

while P_3 results from solving the following Lyapunov equation

$$(A - \sigma_1 \cdot P_1) \cdot P_3 + P_3 \cdot (A - \sigma_1 \cdot P_1)^T = -P_2 \cdot \sigma_2 \cdot P_2 \quad (3.69)$$

and the following definitions are introduced

$$\sigma_1 = B \cdot R^{-1} \cdot B^T \quad (3.70)$$

$$\sigma_2 = C^T \cdot H^{-1} \cdot C \quad (3.71)$$

3.6.2 Implementation

The purpose of the term ρ in Eq. (3.39) is to penalize one cost term more than the other in the minimization process. Essentially, it determines whether one allows large oscillations at the expense of little control power involved or otherwise. Using this term we can normalize the state as well as the control costs, which we denote J_s and J_c .

$$\begin{aligned} J_s &= J_s \\ J_c &= \frac{J_c}{\rho} \end{aligned} \tag{3.72}$$

Plotting these normalized costs is an effective way to compare the performance of different configurations. Fixing one of the performance parameters (actuation orientation or number of active regions) yields a curve close to a hyperbola, as shown in Figure 3.5.

This behavior is completely expected. Wing oscillations can be limited at the expense of high control authority. On the other hand, setting low power consumption results in high displacements. The present analysis framework allows to simultaneously plot these hyperbolas for an arbitrary change in a wing configuration parameter. Actual examples are presented in Chapter 4.

The state cost vs. control cost plot is the key to manage the energy requirements. At this design point, the exact meaning of the control (actuation) energy is somewhat arbitrary. For instance, the exact calibration of the sensors is unknown, and it is determined by the real hardware. Since the regulator uses the information from the sensors to set the required voltage to the actuators, this may get scaled once the actual sensor parameters are entered into the system.

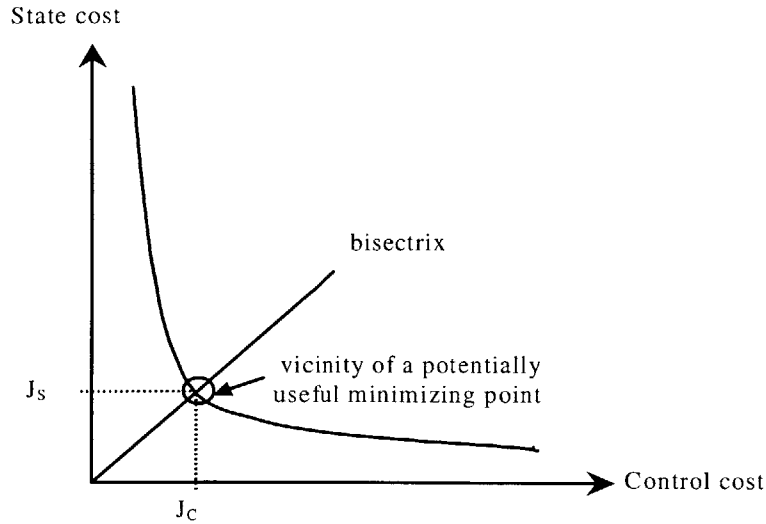


Figure 3.5 Locus of the points that minimize the total energy of the system

Without a firm limitation on the state or control costs, a potentially useful operating point lies in the vicinity of the intersection between the bisectrix of the quadrant and the hyperbola itself, as shown in Figure 3.5. It is a valid preliminary design point, which should be refined as the exact configuration parameters are known. This point determines the minimum equally weighted state and control cost (J_S and J_C respectively). These two values are all there is to be known to determine the weighting parameter ρ in Eq. (3.39) (see Section 3.6.1).

3.7 Transfer Function Sinusoidal Disturbance to Normalized Voltage Magnitude

An important tool for the design is the ability to tell how much authority the controller requires to reject a certain sinusoidal disturbance of given amplitude and frequency. In fact during conceptual design, even more useful than plotting the required voltages in the time domain (which is done in the simulation), is to plot them in the frequency domain. The Bode plot displays the magnitude of the normalized actuation voltage signal with respect to the frequency of the sinusoidal disturbance exciting the wing. Obviously, one Bode plot results for every active region in the structure.

3.7.1 Formulation

The goal is to find the appropriate transfer function between the sinusoidal disturbance affecting our model and the voltage thus required by *every* active region for a given configuration of the actuators.

In Section 3.2 the LQG was already introduced. The starting point is its state space representation in Eq. (3.24), which simplifies to:

$$\begin{cases} \dot{\hat{x}} \\ \hat{x} \end{cases} = A_T \cdot \begin{cases} x \\ \hat{x} \end{cases} + B_T \cdot \begin{cases} w \\ u \end{cases} \\ y = C_T \cdot \begin{cases} x \\ \hat{x} \end{cases} + D_T \cdot \begin{cases} w \\ u \end{cases} \quad (3.73)$$

Since the objective is to obtain the transfer function T_{uw} as

$$T_{uw} = \frac{u}{w} \quad (3.74)$$

everything has to be expressed in terms of u and w .

By definition of the LQG, the input is related to the state vector estimation as

$$u = -C_K \cdot \hat{x} \quad (3.75)$$

and the matrix C can then be altered so that y , the output, becomes u , the input:

$$\bar{C} = [0 \quad -C_K] \quad (3.76)$$

Since the disturbance w is actually a scalar, B_T can also be split as shown below, where the columns are denoted as \bar{G} and \bar{B} respectively,

$$B_T = \begin{bmatrix} b_{11} & b_{12} & \cdots & b_{1m} \\ b_{21} & b_{22} & \cdots & b_{2m} \\ b_{31} & b_{32} & \cdots & b_{3m} \\ \vdots & \vdots & \ddots & \vdots \\ b_{n1} & b_{n2} & \cdots & b_{nm} \end{bmatrix} = \begin{bmatrix} & b_{12} & \cdots & b_{1m} \\ & b_{22} & \cdots & b_{2m} \\ \bar{G} & b_{32} & \cdots & b_{3m} \\ & \vdots & \ddots & \vdots \\ & b_{n2} & \cdots & b_{nm} \end{bmatrix} = [\bar{G} \quad \bar{B}]$$

where n is the dimension of the state vector x and m is $\dim(w) + \dim(u_{ref}) = 1 + \dim(u_{ref})$. The state space representation of the plant plus the regulator can be written as

$$\begin{aligned} \begin{Bmatrix} \dot{x} \\ \dot{\hat{x}} \end{Bmatrix} &= A_T \cdot \begin{Bmatrix} x \\ \hat{x} \end{Bmatrix} + \bar{B} \cdot u + \bar{G} \cdot w \\ u &= \bar{C} \cdot \begin{Bmatrix} x \\ \hat{x} \end{Bmatrix} \end{aligned} \quad (3.77)$$

or equivalently, in vector notation,

$$\begin{aligned} \dot{x} &= A_T \cdot x + \bar{B} \cdot u + \bar{G} \cdot w \\ u &= \bar{C} \cdot x \end{aligned} \quad (3.78)$$

The second equation is substituted in the first equation to obtain

$$\dot{x} = A_T \cdot x + \bar{B} \cdot \bar{C} \cdot x + \bar{G} \cdot w \quad (3.79)$$

and x is isolated using the Laplace Transform, assuming that $x(0) = 0$:

$$\begin{aligned} s \cdot x - A_T \cdot x &= \bar{B} \cdot \bar{C} \cdot x + \bar{G} \cdot w \\ (s \cdot I - A_T - \bar{B} \cdot \bar{C}) \cdot x &= \bar{G} \cdot w \\ x &= (s \cdot I - A_T - \bar{B} \cdot \bar{C})^{-1} \cdot \bar{G} \cdot w \end{aligned} \quad (3.80)$$

This last result is substituted into the last equation in Eq. (3.78), yielding

$$u = \bar{C} \cdot (s \cdot I - A_T - \bar{B} \cdot \bar{C})^{-1} \cdot \bar{G} \cdot w \quad (3.81)$$

and the transfer function can be readily obtained by dividing this last equation by w :

$$T_{uw} = \frac{u}{w} = \bar{C} \cdot (s \cdot I - A_T - \bar{B} \cdot \bar{C})^{-1} \cdot \bar{G} \quad (3.82)$$

The voltage applied to the actuators is provided as peak-to-peak values (see section 2.3.2.1). As a result, the active forces and moments are output per maximum voltage. This means that the output u obtained by means of Eq. (3.81) is already normalized. Therefore, u varies from -1 to $+1$, a value of $+1$ meaning that maximum positive voltage is required for the actuation.

3.7.2 Implementation

Plotting in the frequency domain allows the user to detect which gust frequencies would require more actuation power at a glance. It can even provide clues on which modes have low controllability. The current implementation in Matlab produces plots as the ones shown in Figure 3.6.

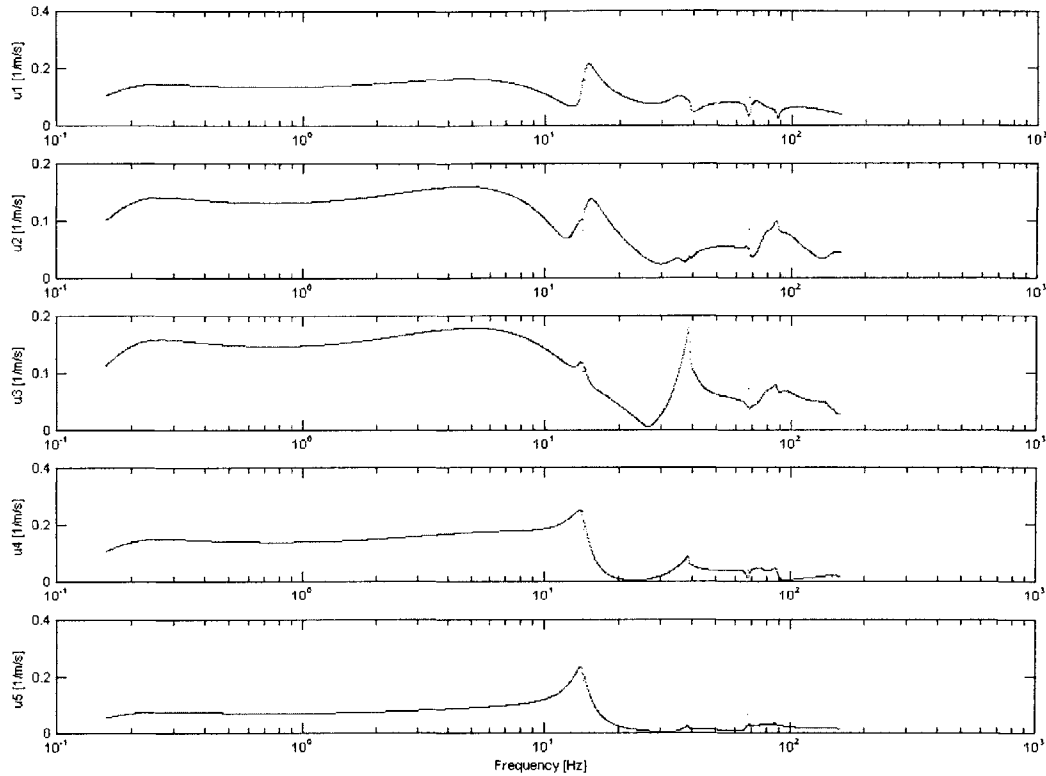


Figure 3.6 Bode plot of the transfer function sinusoidal disturbance to normalized voltage.

3.8 Stability Cost and Pole-Zero Mapping

Two fundamental tools in the stability analysis are developed in this section: a measure of the control power required for stability and a pole-zero mapping for visual flutter identification.

3.8.1 Stability Cost

The measure for stability is the stability control cost, which is the minimum cost necessary to render the plant stable. When every dimension in the process noise and the sensor noise vectors is assumed to be affected by uncorrelated white noise, setting $G=I$, $H=I$, $Q=0$ and $R=I$ in Eq. (3.63) will yield the root mean square value of the stability control cost (Ref. [47]):

$$J_c = \text{trace}(P \cdot K^T \cdot K) \quad (3.83)$$

3.8.2 Pole Zero Mapping

The open loop matrix A determines the open loop poles and zeros of the plant. By plotting those poles, a typical behavior can be observed. At zero airspeed any wing is inherently stable. As the speed increases, some of the poles may enter the right semi-plane, rendering the system unstable (see Figure 3.7).

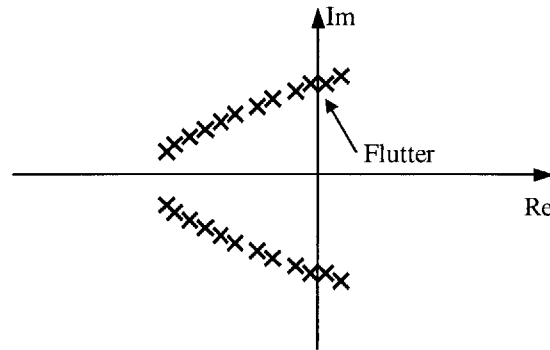


Figure 3.7 Flutter onset detection by pole movement tracking

The present analysis implementation (also coded in Matlab) is able to plot this pole variation with airspeed in the real-imaginary axes plane, which allows to detect the onset of flutter easily. In addition, the closed loop poles of the \bar{A} matrix corresponding to the complete system (plant plus regulator) Eq. (3.11) can be plotted to check the stability of the controller. Numerical examples are given in Chapter 4.

3.9 Stall Detection

Controlling the wing poses a number of challenges, the most important of which are mode uncertainties and non-linearities. During the preparation of this thesis work, an attempt was made to control the wing to improve aerodynamic performance while preventing or reducing the effects of stall. This included the detection of lift and moment through pressure sensors. This work is included here as a feasible method to detect and control non-linear stall

3.9.1 Formulation

One approach to control the non-linear system is to use a describing function, in which approximate gain and phase of the non-linearity is found for a sinusoidal input to the plant [58]. This results in a quasi-linear model of the system, which is a function of the vibration amplitude. By designing a linear controller that is stable for all possible quasi-linear models, a stable close-loop system should result.

A more direct approach is to try to control the non-linear effect directly. The approach for doing so is shown in Figure 3.8.

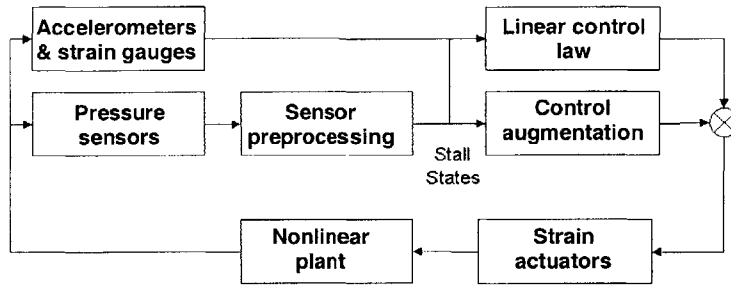


Figure 3.8 Diagram of a stall detection and control model

One of the features of the method is that pressure sensors are the means by which the lift and moment affecting each station at every time are estimated. Those two measurements are used to detect the stall forming a parity signal, which indicate the existence of it. The parity signal is generated as follows. It is observed that, in the linear range, lift and moment are linear dynamic functions of angle of attack, so

$$\begin{aligned}\bar{L}(s) &= G_L(s)\bar{\alpha}(s) \\ \bar{M}(s) &= G_M(s)\bar{\alpha}(s)\end{aligned}\tag{3.84}$$

where $\bar{L}(s)$, $\bar{M}(s)$ and $\bar{\alpha}(s)$ are the Laplace transforms of the lift, moment and angle of attack, $L(t)$, $M(t)$ and $\alpha(t)$. $G_L(s)$ and $G_M(s)$ are transfer functions determined by Theodorsen theory. However, when the wing or part of it stalls, the magnitude of the lift fails to follow a linear behavior and its application point moves along the chord. This introduces variations in the moment, which subsequently diverges from the linear moment to be expected had the airfoil remained in the linear region.

This difference in moment is what it is detected by means of constructing the stall parity function. When the wing is stalled, the parity function is non-zero, and increases its magnitude as the plant goes deeper into non-linearities. The parity signal is given by

$$\bar{P}(s) = G_1(s)\bar{L}(s) - G_2(s)\bar{M}(s) \quad (3.85)$$

where G_1 and G_2 are chosen so that

$$G_1(s)G_L(s) = G_2(s)G_M(s) \quad (3.86)$$

Then, so long as the wing is unstalled and Eq. (3.84) holds,

$$\bar{P}(s) = 0 \Rightarrow p(t) = 0 \quad (3.87)$$

When the wing is stalled, Eq. (3.84) no longer holds, and generally $p(t)$ is non-zero.

3.9.2 Simulation results

In order to be able to present some theoretical results, the real plant has been replaced with a fully non-linear model of it, consisting of the ONERA stall model and a series of inflow states to model the aerodynamic lags. This model should be representative enough of the real airfoil, and the parity function behavior can be computed from it. The overall plant was implemented in Simulink and is depicted in Figure 3.9. The aerodynamics block and the lift stall detection model have been included in full detail too (Figures 3.26 and 3.27). The moment stall detection block is analogous to the lift one.

Next, the airfoil is commanded to follow a sinusoidal motion. The angle of attack is gradually increased from 0° to 60° peak to peak 1 Hz oscillations (well beyond stall). It remains then oscillating at constant amplitude for 20 seconds, time at which the oscillations are brought down to $\pm 10^\circ$ oscillations (below stall).

The results have been plotted in Figure 3.12. The spikes in the Parity Function when the airfoil stalls are self-evident, and could therefore be used for stall detection.

3.9.3 Control design using the parity signal

Given the parity signal, there are two control options. First, linear feedback could be applied, designed to add damping to the system. This additional term would reduce the

optimality of the controller with respect to other objectives, such as improving performance, but would stabilize, say, stall flutter.

The second option is to use the parity signal as a stall indicator to trigger a switch between a linear to a nonlinear controller. Whenever a stall is indicated, a non-linear control response would be initiated to reduce the average angle of attack, alleviating stall, again perhaps at the expense of other objectives.

Both of these options are beyond the scope of the current work, but should be pursued in the future.

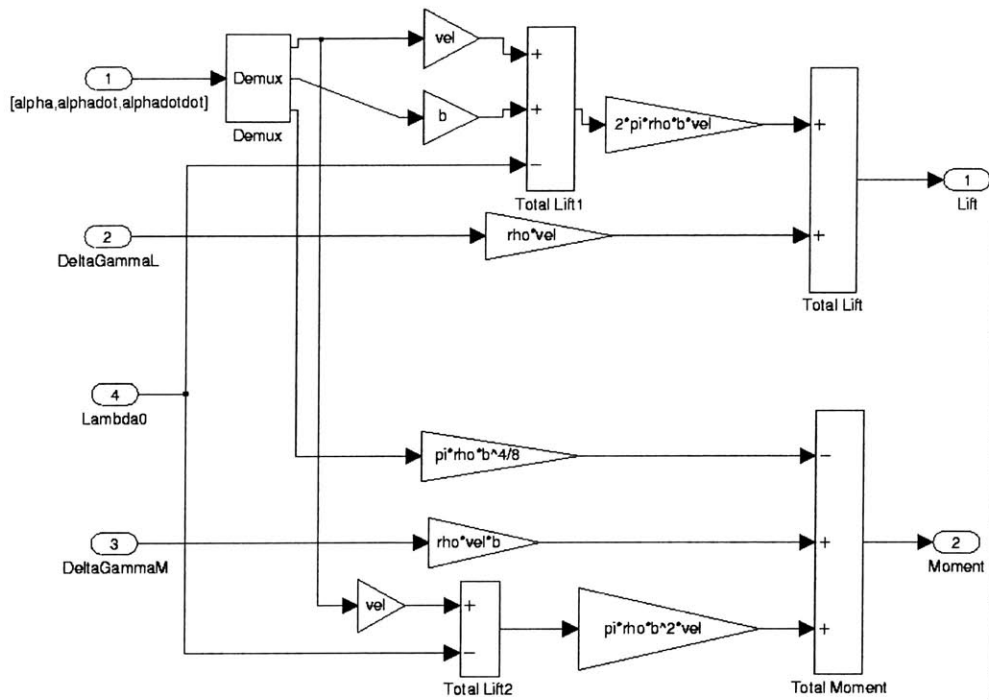


Figure 3.10 Simulink block of the aerodynamics model

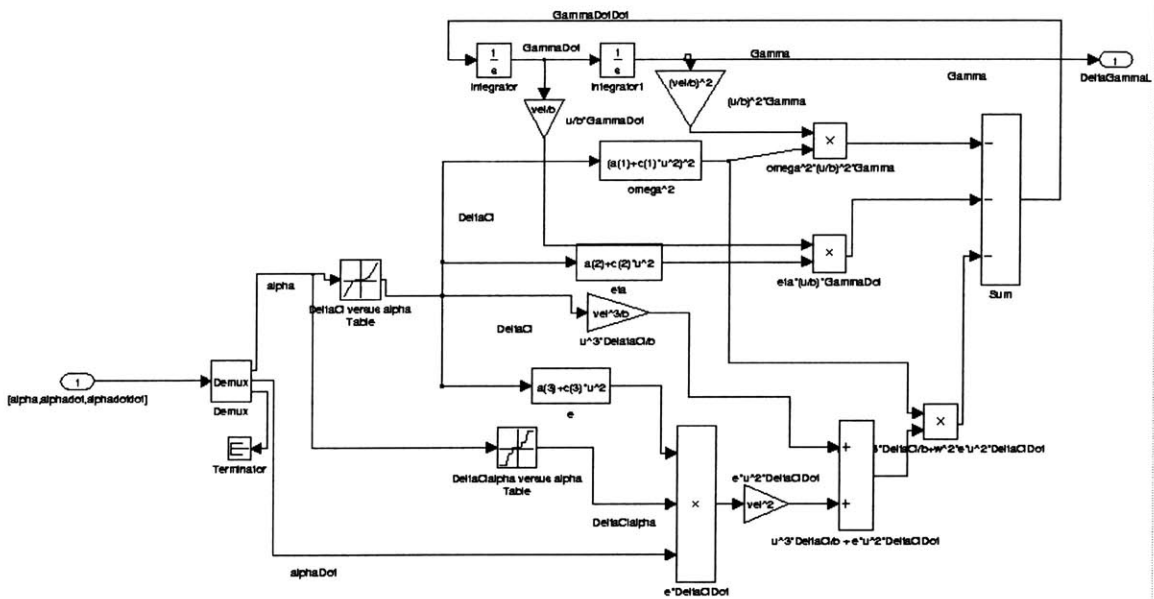


Figure 3.11 Simulink block of the lift stall model

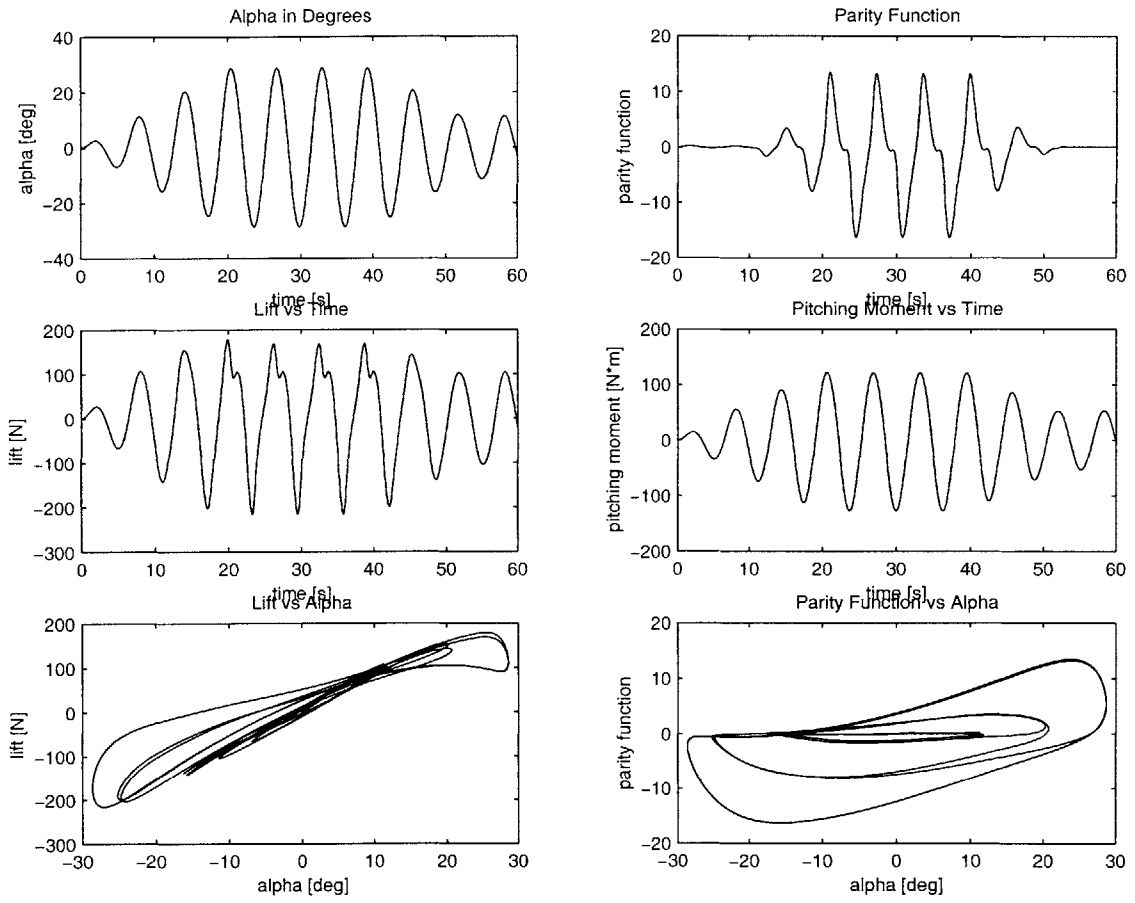


Figure 3.12 Generation of the parity function.

Chapter 4

Results

In this chapter, the viability of the framework as an effective aeroelastic analysis and tailoring tool is demonstrated. A wind-tunnel model representative of UAV wings is selected and different LQG controllers are designed and simulated at set flight velocities. Simulation of the resulting aeroelastic systems are run to study the impact of parameter variation in flight performance, namely angle of attack, actuation orientation and grouping, and sensor location and type. A normalized control cost denoting the actuation energy and a normalized state cost denoting the total energy of the wing are the selected performance parameters. Finally, a simple robustness checked is performed on the LQG regulator.

4.1 A Proposed Wind Tunnel Model Wing

Typical High Altitude Long Endurance (HALE) vehicles fly under $M=0.5$ and tend to have a tapered wing with a half aspect ratio between 8 and 15 (Refs. [43] and [44]). Typical examples are the Lockheed Martin/Boeing DarkStar and Aurora's Theseus and Perseus among others. A wing concept that allows for the investigation of all the relevant phenomena of interest that are representative of present and future UAV wings is presented here.

The wing for this study is a proposed wind tunnel model geometrically and dynamically representative of existing and potential new HALE UAV wings. The model is tapered (taper ratio 1:2) through 75% of the wing (Figure 4.1) for aerodynamic performance.

The most prominent features of this wind tunnel model are the following:

- Presents non-linear aeroelastic characteristics due to large structural deflections.
- Presents flutter at subsonic speed.
- Fits in the NASA Langley Transonic Dynamics Tunnel with the appropriate clearances (for future experimental test).

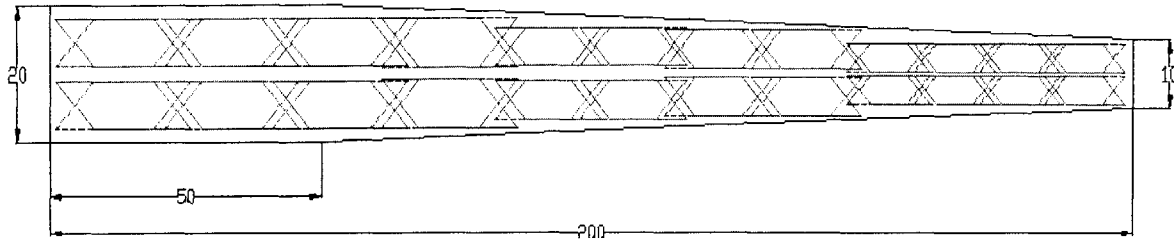


Figure 4.1 Planform diagram of the proposed wing design showing the distribution of the actuation (dimensions in cm).

Key parts in the cross-sectional design are the cross-sectional shape, including number of spars and location, and the composite lay-up. The decision was to have a single spar at 40% chord, helping to reach the torsional rigidity that would help in flutter.

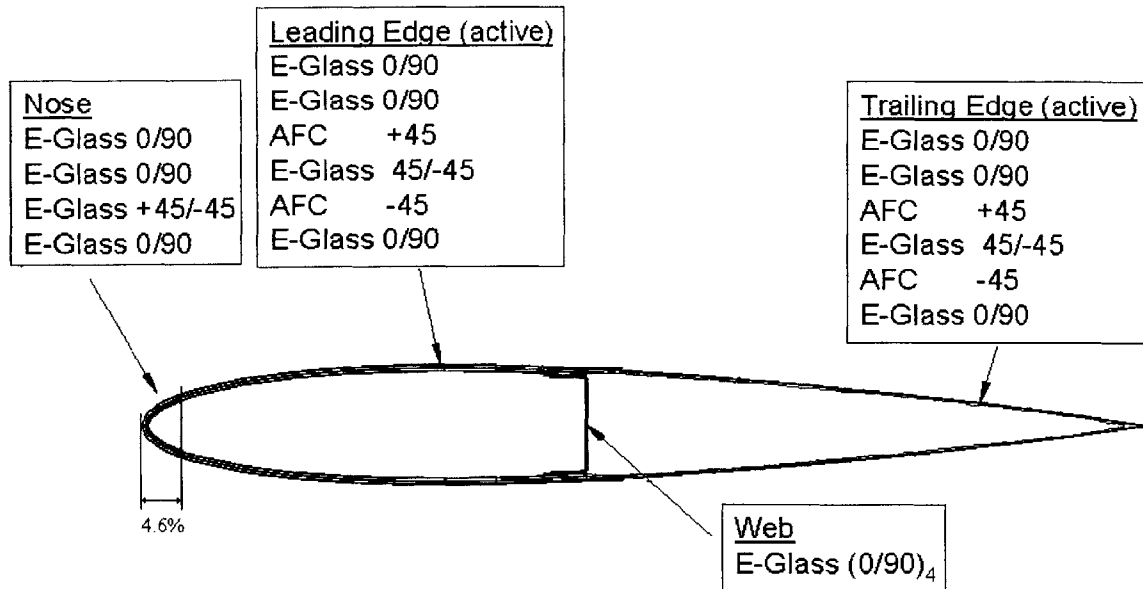


Figure 4.2 Lay-up of the wind tunnel model's cross-section (NACA 0014)

This one-spar construction is in fact used in certain UAVs, as in the case of Aurora’s Perseus. The spar placement and composite lay-up were optimized for low maximum stress and best aeroelastic performance. The airfoil shape used for design was the NACA 0014, approximating the NACA 6514 that is representative of high-altitude flight, presently in use by some of the HALE vehicles. The lay-up of the airfoil is depicted in Figure 4.2. The lay-up shows the actuators placed at $\pm 45^\circ$, but their lay-up angle will be varied from 0° to the $\pm 45^\circ$ shown in order to investigate the effect of their orientation on the aeroelastic performance of the wing. The different cross sections have been discretized using 6-node isoparametric elements. The resulting meshes range from 1993 nodes and 823 elements at the root to 1021 nodes and 422 elements at the tip. Detailed cross sectional stiffness, mass and actuation properties are detailed in Appendix A. Note that the stiffness properties change with the actuator orientation since they are an integral part of the structure.

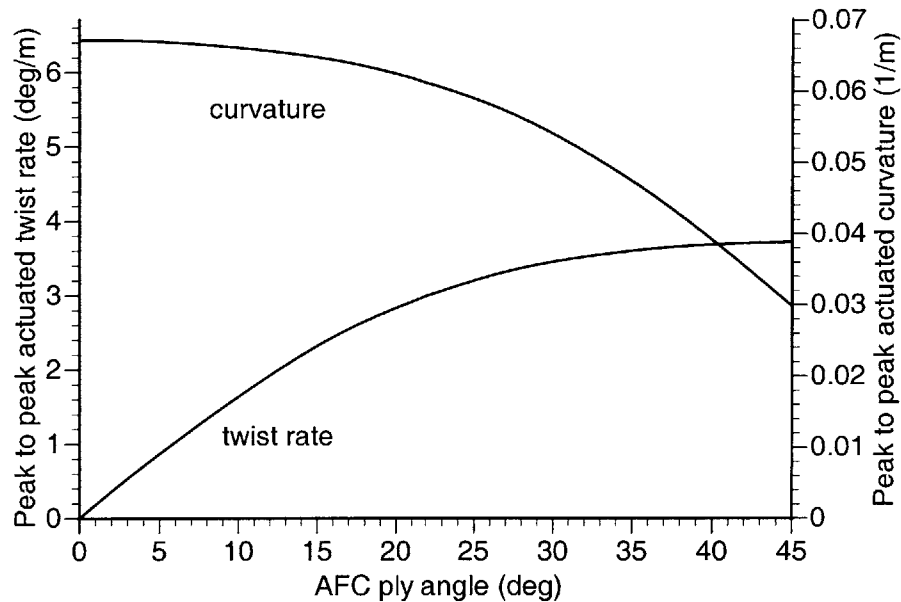


Figure 4.3 Maximum actuation for twist and bending as function of the AFC actuator ply angle.

The integral actuation in the study cases is achieved through the use of active fiber composites (AFC) with interdigitated electrodes (see Section 2.2.4), as used to validate VABS-A in Chapter 2. The AFC packs are embedded in the composite construction, and they provide a feasible way of integrally actuating the structure with high levels of

actuation authority. Figure 4.3 shows the maximum values of both induced twist rate and bending curvature that is expected from the configuration shown in Figure 4.2. This actuation anisotropy will be explored for performance enhancement.

Finally, the discretization along the span of the wing is done using 10 finite elements based on previous convergence study [54].

4.2 Open Loop Performance

The present section uses the open loop response to point out the special attributes of an aerolastic plant. The differences have to do with the non-linearity in the structure and in the flow, and above all, the onset of instability as airspeed is increased.

4.2.1 The Effect of Airspeed

One of the key performance parameters is the airspeed at which the wing presents flutter. A very convenient way to obtain this information is to plot the variation of the poles of the plant with increasing airspeed making use of the theoretical formulation and subsequent Matlab implementation developed in Section 3.8.2. At zero speed, the plant is stable. As the wing flies faster it reaches a point where a pair of poles enter the right half plane (where the real part of the eigenvalues become positive). As a preliminary study, consider the dynamic stability of the proposed active wing in an open loop configuration for the actuation oriented at $\pm 45^\circ$ and the root angle of attack set at 2° (see the plot in Figure 4.4). The following step is to identify which mode corresponds to every branch in the figure. The first 20 modes for zero airspeed are plotted in Figures 4.33 and 4.34. Table 4.1 summarizes the first 12 modes with the lowest frequency.

Figure 4.5 indicates that some of the modes have already some coupling due to the wing set at 2° root angle of attack. Table 4.1 also shows these interactions. As the speed increases, the modes become more coupled due to the aeroelastic interaction. Consider for instance the case of the wing with the AFCs oriented at $\pm 45^\circ$. The exact flutter speed for that configuration is 43.4 m/s. This is a typical case of frequency coalescence flutter [45], as can be seen in Figure 4.4. The fact yet to determined is what two modes coalesce in the instability. Figure 4.7 shows the 10 modes with the lowest frequency for the wing

flying at flutter speed. By direct comparison of the frequency of the modes in Figures 4.32 and 4.34 one can deduce that the unstable mode is the first chordwise bending which is clearly coupled with the first torsion mode coalescing with the second flatwise bending mode, at a 14.3 Hz frequency. The flutter frequency for the $\pm 22^\circ$, and 0° actuator orientations at the 2° angle of attack are 16.7 Hz and 18.0 Hz, respectively. The flutter type and modes are the same as the ones discussed for the $\pm 45^\circ$ actuator orientation.

Table 4.1 Structural modes for zero airspeed, 2° angle of attack and AFCs at $\pm 45^\circ$

Hz	Mode
2.9	1st Bending
14.0	2nd Bending
14.7	1st Chordwise Bending
38.1	3rd Bending/1st Torsion
41.8	1st Torsion/3rd Bending
67.5	2nd Chordwise Bending
81.0	4th Bending/2nd Torsion
91.3	2nd Torsion
148.8	3rd Torsion
157.2	5th Bending
170.1	3rd Chordwise Bending
228.3	4th Torsion

One of the challenges then is to design a LQG regulator around the plant that renders the wing stable above flutter speed and that effectively rejects gust disturbances, both above and below flutter. The sections that deal with the closed loop performance show that such an accomplishment may be feasible.

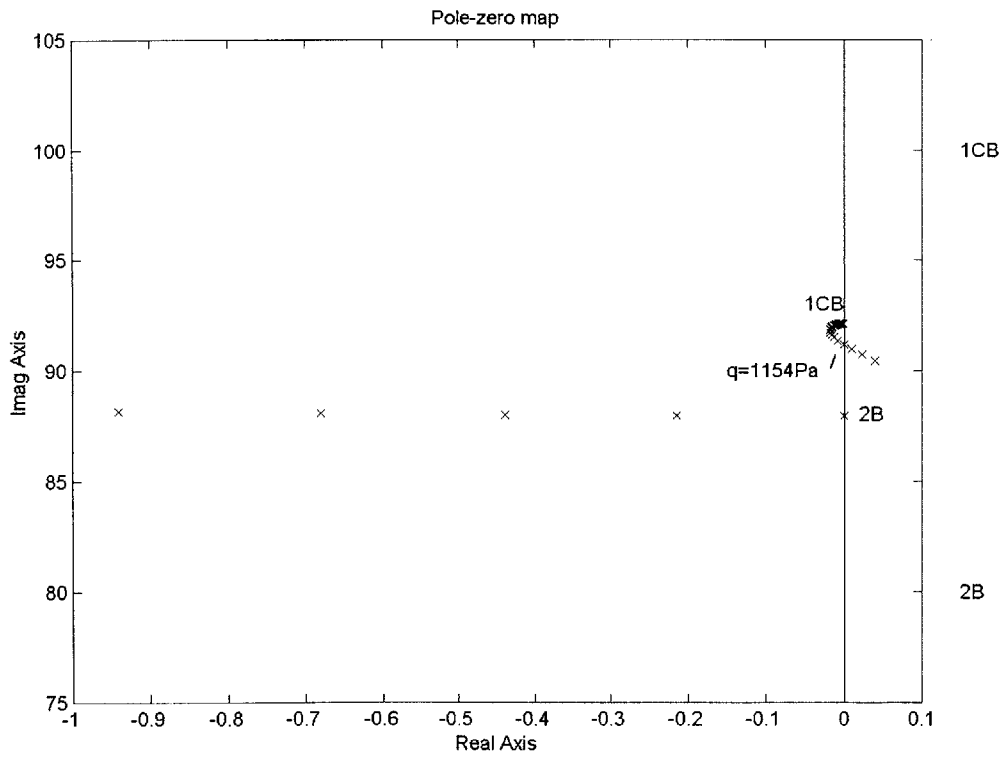
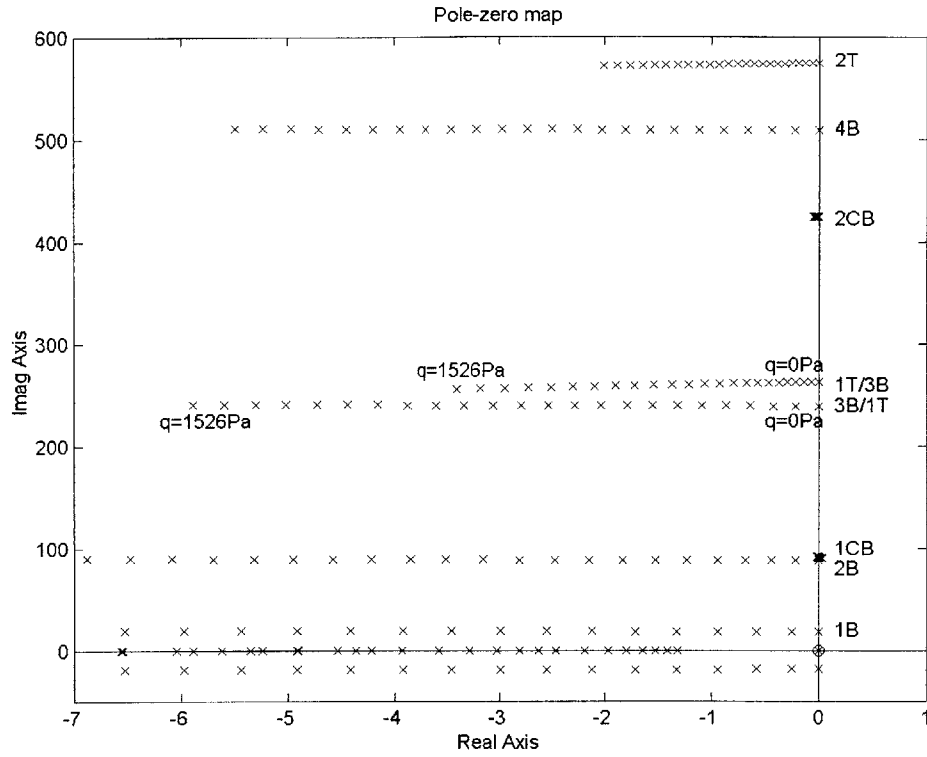


Figure 4.4 Open loop pole variation of the plant with airspeed (zoomed below)

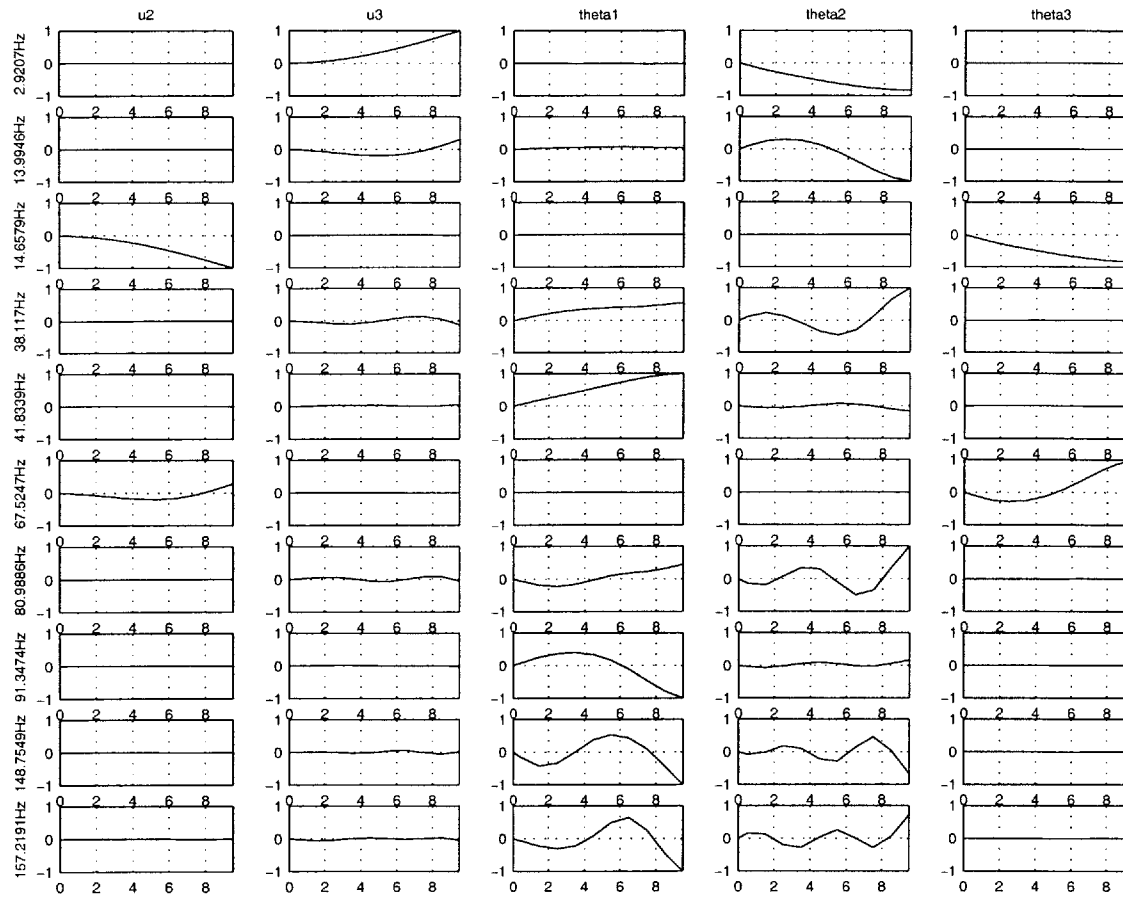


Figure 4.5 Open loop structural modes at zero speed, 2° angle of attack and AFCs oriented at $\pm 45^\circ$ (modes 1 to 10).

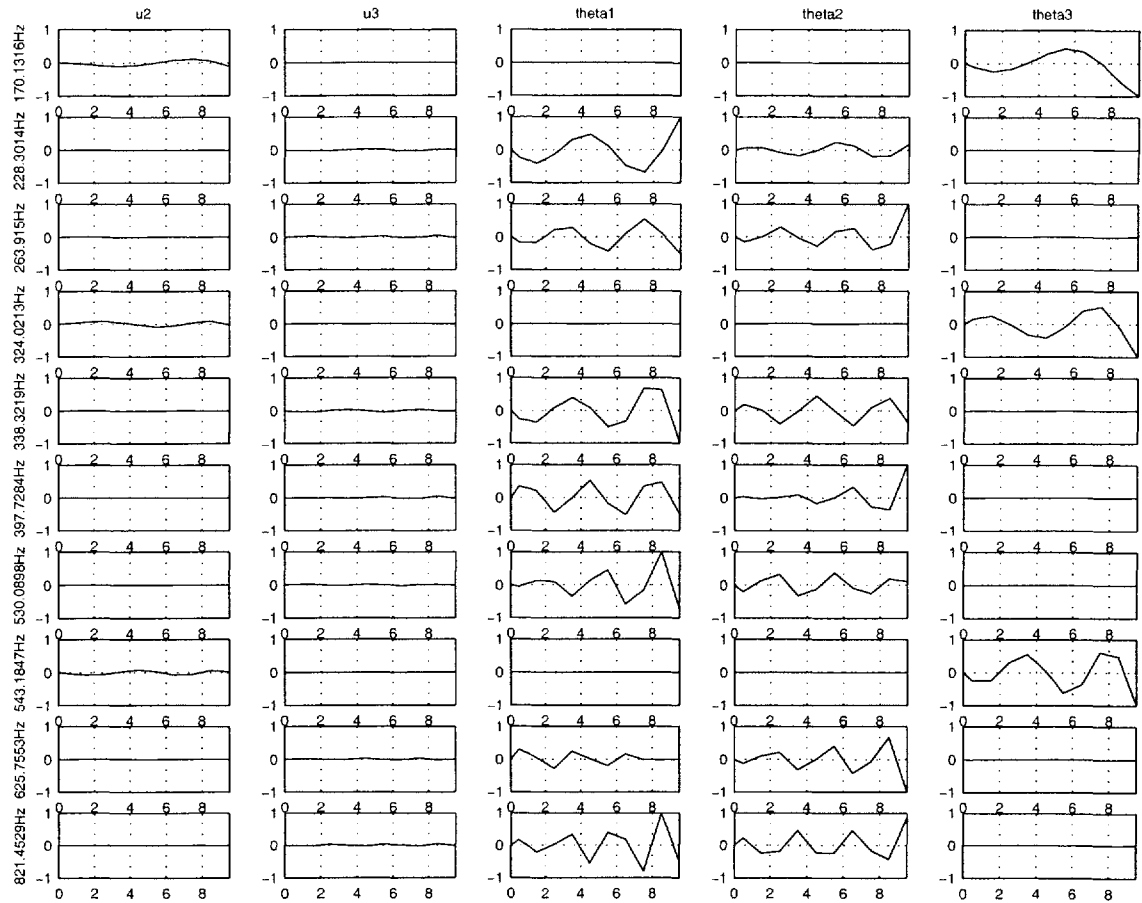


Figure 4.6 Open loop structural modes at zero speed, 2° angle of attack and AFCs oriented at $\pm 45^\circ$ (modes 11 to 20).

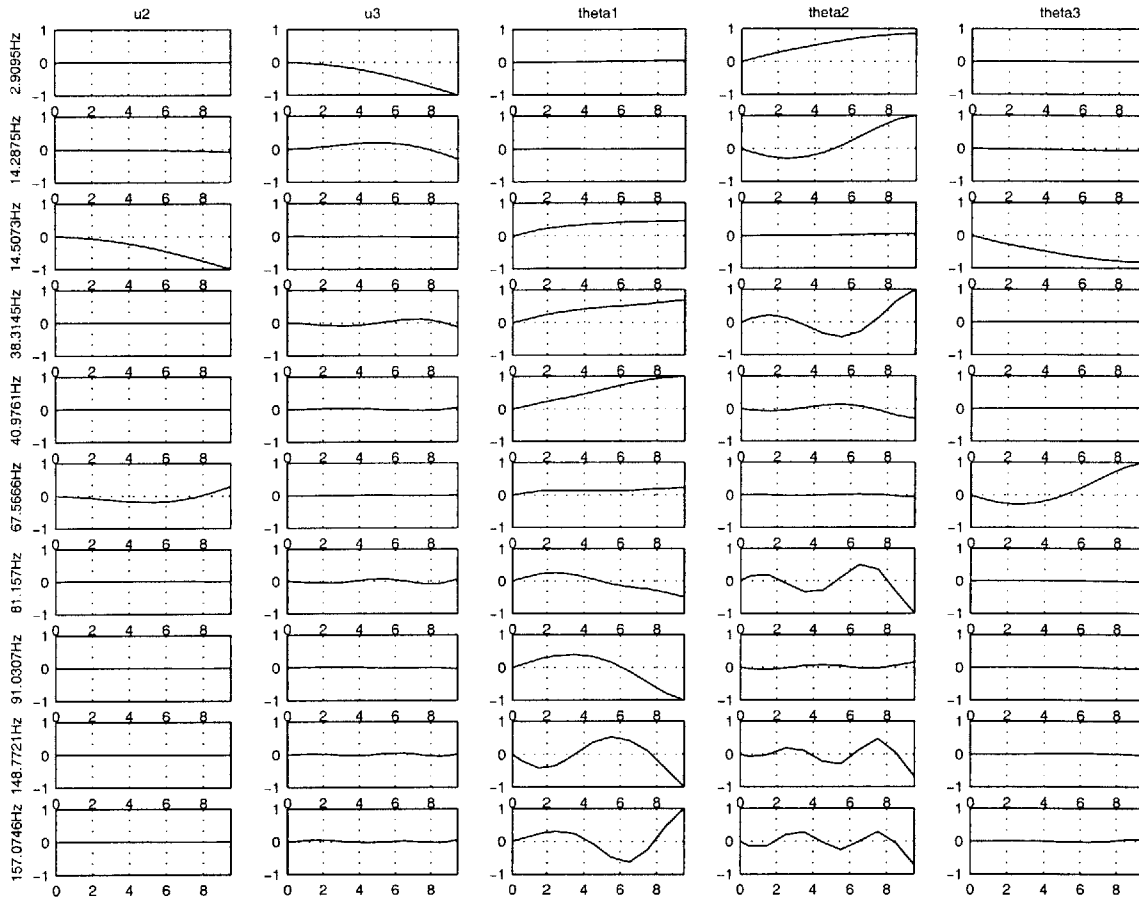


Figure 4.7 Open loop structural modes at flutter speed, 2° angle of attack and AFCs oriented at $\pm 45^\circ$ (modes 1 to 10).

4.2.2 The Effect of Angle of Attack

The aeroelastic characteristics of the open loop system is function of the “steady-state” loading, reflected here as the root angle of attack. A detailed discussion of the impact of this parameter in the passive aeroelastic stability of a flexible wing is presented in Ref. [54]. Figure 4.8 exemplifies the variation of flutter speed and flutter frequency with angle of attack for the $\pm 45^\circ$ actuation orientation case. As the angle of attack increases, so do the loads on the wing and the corresponding deflections, and the geometric non-linearities lead to frequency coalescence at lower velocities and thus to a

decrease in flutter speed. In fact, there is a jump clearly observable in the flutter frequency plot at very low angles of attack. The reason for this jump is the change in the two modes that coalesce in flutter. At zero root angle of attack, the modes coalescing are the first torsion mode and the third bending mode. At any other angle of attack, the unstable modes about the nonlinear steady condition are the first chordwise bending/first torsion (together) and second flatwise bending modes. Therefore, the case studies that follow will be set to 2° angle of attack as a representative instability mode.

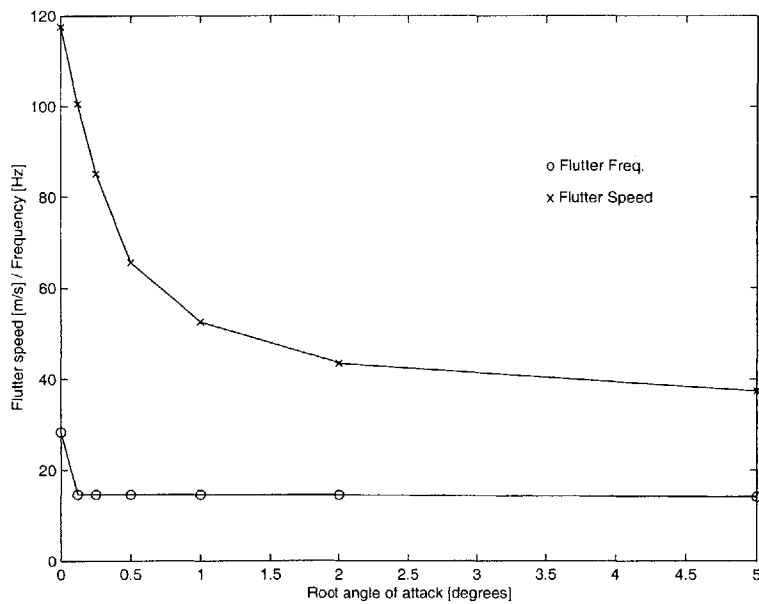


Figure 4.8 Effect of non-linear steady state on flutter

4.3 Closed Loop Performance

The present low-order active model allows to analyze different configurations dynamically. The following sections investigate how the LQG regulator performs on different wing configurations. In particular, they investigate the effect of changes in airspeed, angle of attack, actuation orientation, number of control regions and sensor type and placement. The configuration varies from section to section depending on the effect being investigated. A reasonable arrangement of the different configuration parameters is

set *a priori* at the beginning of every section. The different analysis parameters that are investigated are the following

- The actuators orientation is chosen based in the static actuation results for the previous configuration in terms of induced twist rate and bending curvature (see Figure 4.3). Based on the figure, the actuators are placed at three different orientations: 0° , which provides maximum (flatwise) bending actuation, $\pm 45^\circ$ (labeled '45T'), which provides maximum torsion actuation, and $\pm 22^\circ$, which represents a balanced twist-bending actuation. These last two cases, the $\pm 45^\circ$ and the $\pm 22^\circ$ orientation, can be actually actuated in bending or in torsion by varying the shape of the electric field applied to the AFC at each cross-section of the wing. These two additional configurations are also tried. They are labeled '45T' and '22T' when actuated in torsion, and '45B' and '22B' when actuated in bending.

- The number of active zones range from one (covering the full span of the wing) to 10, which implies that every element in the discretization can be actuated independently.

- Combinations of the three different types of sensors are studied too: bending strain gauges, torsion strain gauges, and accelerometers in the flatwise direction.

The performance is measured in two different ways. First, a stability analysis is carried out to determine under what circumstances the LQG regulator renders the plant stable. Secondly, the capacity of the LQG regulator to reject a gust affecting the wing is studied. The wing is flown above flutter speed for stability and at two speeds for gust alleviation (one above flutter and the other below flutter).

4.3.1 Stabilizing the plant by determining the weighting parameter ρ

Section 3.6 described how to obtain a design point that minimizes the total energy of the system. A simple configuration case flown above flutter is set up now in order to get a numerical example of the formulation presented there. Once the working point has been determined, a regulator will be designed to stabilize the plant. The configuration is the following:

- The wing is flown above flutter speed (15% over flutter speed).

- The root angle of attack is set to 2° .
- It was shown in the previous section that the mode going unstable under these conditions is the first chordwise bending /first torsion mode coupled with the second flatwise bending one. For this reason, the actuators are oriented at $\pm 45^\circ$ in order to maximize torsion control (there is no direct controllability on the chordwise bending modes), but all orientations will be plotted in the state cost vs. control cost plot to demonstrate the procedure.
- The number of active regions is set to 10, that is, every element is an independently actuated zone. This guarantees the maximum possible controllability within the current discretization.
- One sensor of each type is placed at the center of every element, that is, a bending strain gauge, a torsion strain gauge, and an accelerometer.

The resulting curves after the appropriate numerical calculation for this configuration is presented in Figure 4.9.

With the proper scaling as explained in Section 3.6, the intersection of the bisectrix and the hyperbolas determine a potentially good minimum energy design point. The resulting value of ρ after the appropriate iteration is then used in the LQG regulator . ρ is set to unity for this example. This design point does not imply that the potential and kinetic energy in the system are a minimum, but rather that it is the most cost-effective solution. In other words, it minimizes both the total energy in the wing and the actuation energy. This procedure is the one used in the following sections to establish a working point for the regulator.

A regulator will be designed next using this design point for the sample configuration to show that the plant can be rendered stable above flutter. Evidently, the plant is stable for airspeeds below flutter and unstable otherwise without any regulator (see Figure 4.4). Now that the speed is set at 49.91 m/s (15% over flutter speed) for the $\pm 45^\circ$ actuation orientation case under study here, the LQG regulator should render those poles stable.

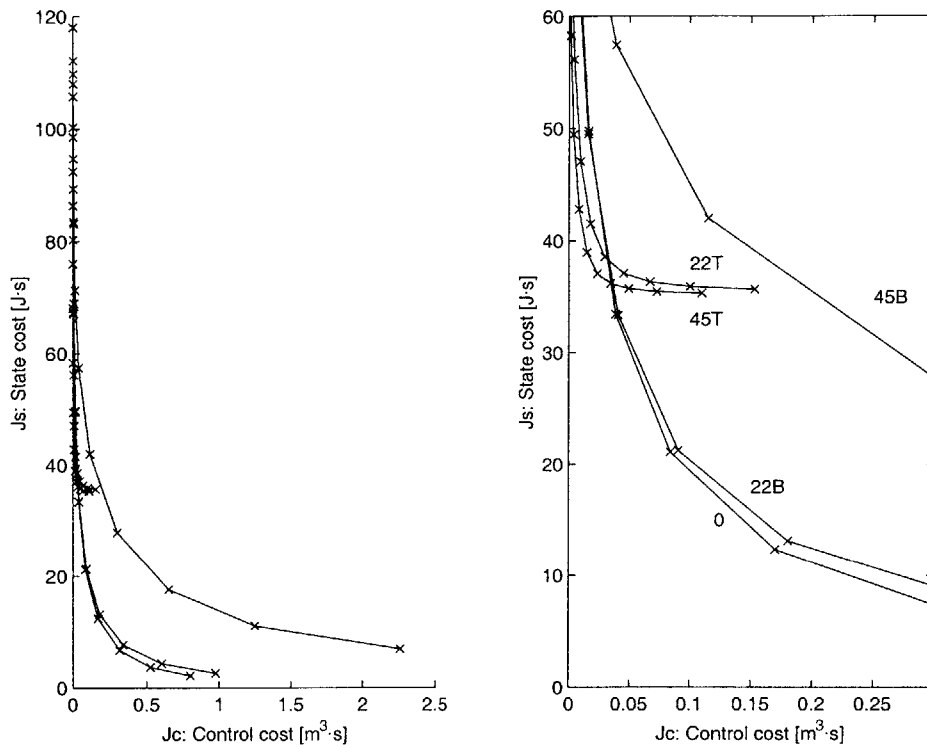


Figure 4.9 State cost vs. control cost plot for a configuration flown at 15% over the flutter speed and at 2° root angle of attack.

Figure 4.10 explicitly shows the closed loop poles (which are now stable) against the open loop poles plotted in Figure 4.4, from flutter speed to 15% above flutter in 2.5% intervals. The symbol 'x' denotes the open loop poles and the symbol '◇' denotes the closed loop poles. The plant is stable under the LQG for speeds above flutter. The following section deals with the real cost implied in turning the plant stable for the three orientations.

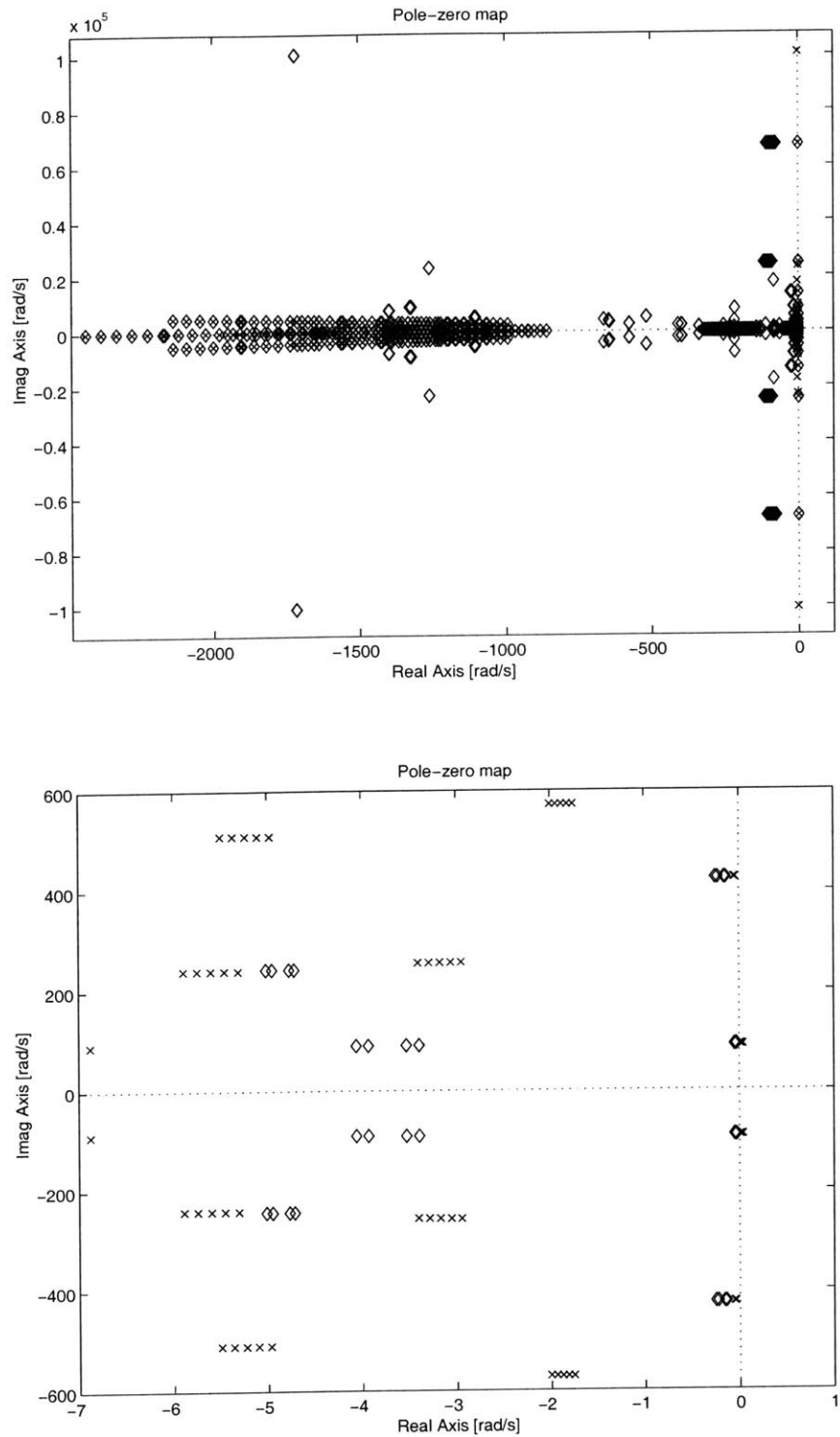


Figure 4.10 Open loop (x) - closed loop (\diamond) pole map of the $\pm 45^\circ$ actuator orientation at 2° root angle of attack from flutter speed (43.4 m/s) to 15% above flutter (49.9 m/s) in 2.5% intervals (zoomed below).

4.3.2 The Effect of Actuation Orientation

The parameter most intimately related with the active structure is the orientation of the anisotropic strain actuation. Consider the dynamic stability of the proposed active wing in an open loop configuration. Due to the embedded nature of the strain actuators, these become an integral part of the structural wing, that is, by varying the orientation of the AFCs, besides changing the actuation characteristics, the (passive) wing stiffness constants change. This results in a variation of the flutter speed for each case, as mentioned in the previous section. Table 4.2 presents the flutter speed for each configuration of the actuators.

Table 4.2 Flutter velocities for the different orientation of the AFC lamination angle for a root angle of attack of 2° .

AFC Orientation	Flutter Speed [m/s]
0°	49.6
$\pm 22^\circ$	46.8
$\pm 45^\circ$	43.4

In what follows, the effect of actuation orientation on both stability enhancement and gust alleviation will be investigated for the proposed wind tunnel model. The gust study will be conducted both above and below flutter speeds. To account for the changes in the flutter speed for the different active configurations, the velocities are normalized with respect to the corresponding flutter speed. Therefore, in what follows, conditions above and below the flutter speed are set to $\pm 15\%$ of the corresponding flutter speed, respectively.

Finally, the control cost J_c has to also be normalized so that the different velocity settings, which correspond to different flow energies, can be factored when comparing costs of different LQG designs. The normalization adopted in this study is given by

$$(J_C)_{normalized} = \frac{J_C}{\bar{k}\rho_\infty u_0^2} \quad (4.1)$$

where $\bar{k}\rho_\infty = 1 \frac{kg}{m^3}$ is just an adjustment constant, and u_0 is the (uniform flow) flying speed.

The relative performance between three orientation angles is studied: 0° , $\pm 22^\circ$ in bending actuation, (22B), $\pm 22^\circ$ in torsion actuation (22T), $\pm 45^\circ$ in bending actuation (45B), and $\pm 45^\circ$ in torsion actuation (45T). The 0° orientation maximizes the forcing bending moment on the structure while $\pm 45^\circ$ actuated in torsion maximizes the twist. The rest of the performance parameters are set as follows:

- The root angle of attack is set to 2° to simulate a realistic operating condition.
- The number of active regions is set to 10, that is, every element is an independently actuated zone.
- One sensor of each type is placed in every element, that is, a bending strain gauge, a torsion strain gauge, and an accelerometer.

4.3.2.1 The Effect of Actuation Orientation on Stability

Section 3.8.1 showed how to quantify the amount of control required for stability (the *stability* cost). That formulation is used to compare the relative performance of all the orientations. The result is shown in Figure 4.11. Placing the piezoelectric actuators at $\pm 45^\circ$ and actuating them in torsion (“45T” curve) proves to be the most effective way of stabilizing the plant. At that orientation, maximum twist authority is available from the given set of AFC actuators, and the normalized stability control cost is the lowest. Therefore, by orienting the actuators at lower angles than $\pm 45^\circ$ and exciting them for twist actuation, the authority will be lower and the control cost higher, requiring more actuation power. This is verified for the $\pm 22^\circ$ being actuated in torsion (labeled “22T” in Figure 4.11). Since the 0° orientation in torsion does not produce any net twist actuation (Figure 4.3), it is not shown in the plot. However, since the unstable mode is also composed of bending deformation, an alternative actuation mode is possible for stabilization of the plant. Even though not as efficient as the “45T,” having maximum bending actuation from the AFC at 0° (“0” curve in Figure 4.11) presents a reasonable

option for stabilizing this plant within the defined speed regime. In fact, this bending actuation is equivalent in terms of control cost to the “22T.”

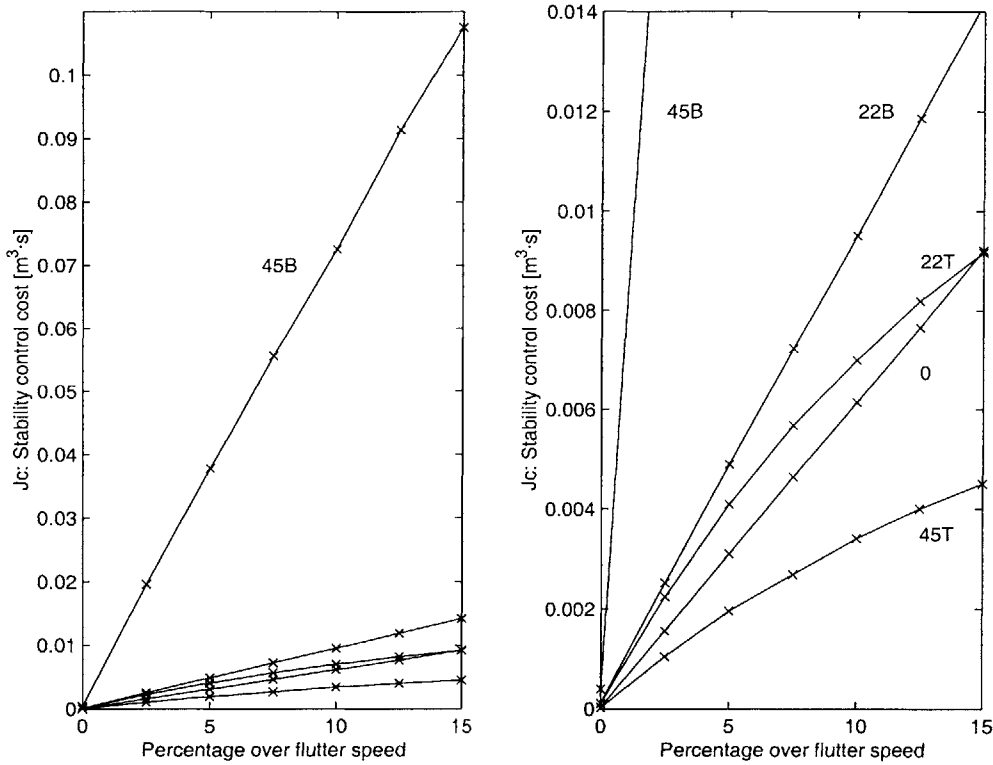


Figure 4.11 Normalized stability control cost vs. percentage over flutter speed for the wing flying at 2° root angle of attack (zoomed on the right) for different actuator orientations.

Similarly as explained above, by orienting the strain actuators to angles different than 0° will reduce the bending authority. This can be seen on the results of $\pm 22^\circ$ and $\pm 45^\circ$ actuated in bending, labeled “22B” and “45B,” respectively.

4.3.2.2 The Effect of Actuation Orientation on Gust Alleviation

The first step is to set a gain for the regulator. Unfortunately, the optimum gain is linked to the nature of the disturbance (essentially its frequency). The current wing under study is a scaled model of a representative wing typically 8 times larger. A typical gust scale length varies from 15 m to 150 m (Ref. [50]). Since the wing is flying close to 50 m/s, a simple calculation yields a frequency bandwidth between 0.3 and 3.5 Hz. From the power spectral density of real gusts, it can be inferred that their low frequency content is high (Ref. [50]). Since the gust model adopted is a single-frequency one, a reasonably low gust frequency of 3 Hz roughly matching the first bending mode of all configurations is chosen as the excitation frequency. The amplitude of the disturbance is set to 5 m/s for the $\pm 45^\circ$ case, and will be corrected for the other cases accordingly so the normalized gust amplitude by the flying speed is a constant. Table 4.3 summarizes the gust magnitudes for each configuration, and Figure 4.14. shows the gust profile.

The previous section detailed how to determine the working point of the regulator by inspection of hyperbolic curves as the ones depicted in Figure 4.9. This design point yields an acceptable performance point for any frequency. Since the disturbance frequency is now set (3 Hz), the performance of the regulator for that particular frequency can be improved by refining the weight ρ through iteration. This iteration process implies determining the weight for which the disturbance can be rejected without saturation of the actuators. A very convenient way to do this is to use the sinusoidal-disturbance-to-voltage transfer function Bode plot provided by the proposed framework (see Section 3.7). The resulting transfer function for the $\pm 45^\circ$ orientation at 15% over flutter speed for all 10 actuation regions is shown in Figure 4.12. Figure 4.13 shows the same type of plot for the 0° orientation. Both plots correspond to the optimum weight for the 3 Hz disturbance.

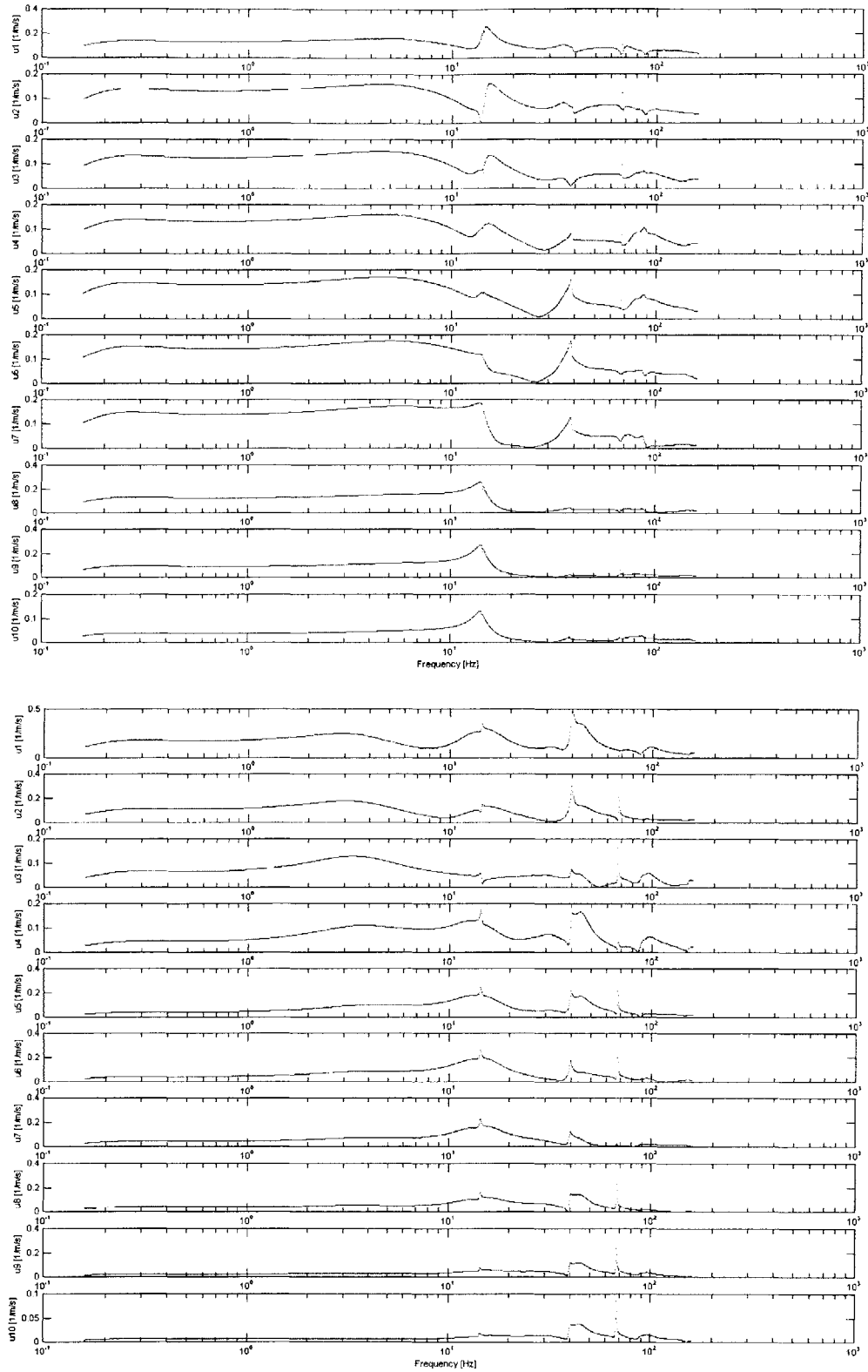


Figure 4.12 Sinusoidal disturbance to voltage T.F. for $\pm 45^\circ$ actuation orientation actuated in torsion (above) and bending (below), at 2° root angle of attack and 15% above flutter.

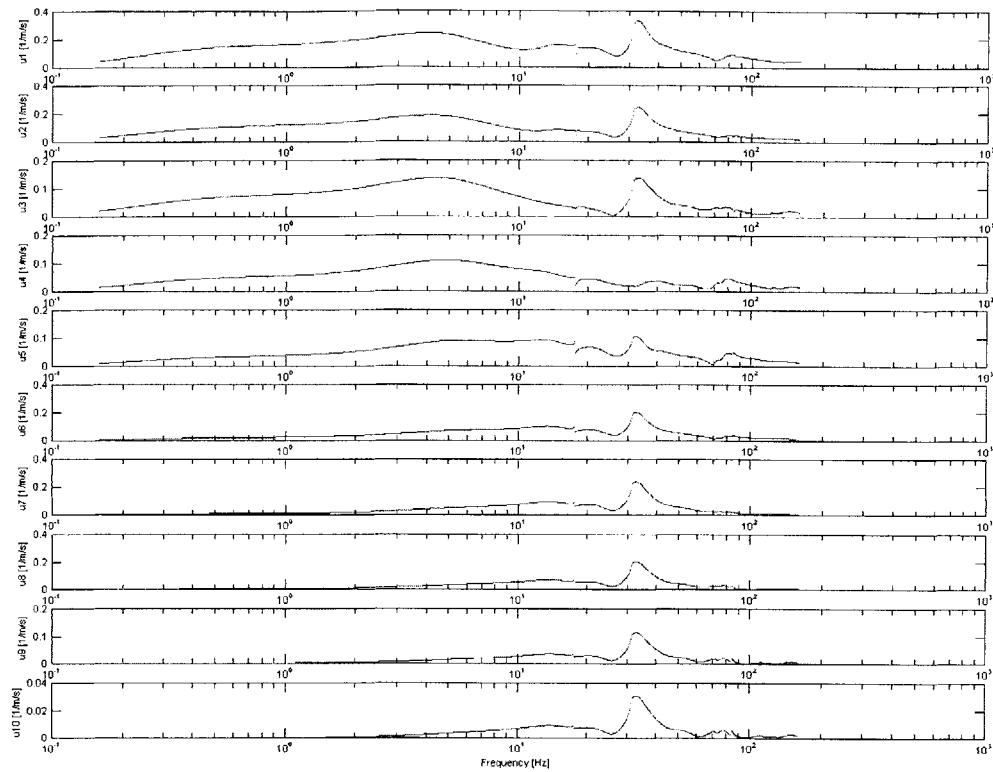


Figure 4.13 Sinusoidal disturbance to voltage T.F. for the 0° actuation orientation actuated in bending at 2° root angle of attack and 15% above flutter.

The Bode plots provide valuable information on the maximum voltage level required by any sinusoidal disturbance. That maximum corresponds in fact to the spikes located at around 100 Hz, which in turn correspond to the higher chordwise bending modes, of which the system has no direct controllability. This is not an upsetting situation, since their frequency is much higher than that associated with the gust. For the selected 3 Hz, the voltage required (value of the transfer function) is approximately 0.2. That means that 20% of the available voltage limit is required to reject a 1 m/s gust. This confirms that rejection of the 5 m/s gust will exactly require the maximum voltage available (or in this case, tolerated by the AFCs).

It is obvious that the process above could not have been carried out if the regulator did not render the plant stable. Without an external disturbance the wing would be theoretically stable even when flying above the flutter speed. The slightest disturbance would then render the wing unstable. This case, gust alleviation above flutter is studied next.

Table 4.3 Gust amplitudes used in the study of the different active configurations.

AFC Orientation	Gust Magnitude [m/s]
0°	5.7
±22°	5.4
±45°	5.0

4.3.2.2.1 Wing Flying Above Flutter Speed

The configuration is the same as the one used in the stability analysis. Figures 4.17 and 4.19 show the time response of the tip of the wing to the 3 Hz gust disturbance (Figure 4.14) for the $\pm 45^\circ$ actuation orientation actuated in torsion and bending respectively. As one can see, the maximum magnitude of the flatwise tip deflection about the nonlinear equilibrium position is about 15% of the wing semi-span, and the maximum tip rotation is about 3° . The chordwise tip deflection remains roughly about its steady value (maximum unsteady deflection of about 2 mm). Figures 4.18 and 4.20 show the voltage history of both configurations to the same disturbance. Note that in all the cases the actuators never saturate, which was expected since the gust amplitude was chosen based on the disturbance to voltage transfer function. Figures 4.15 and 4.16 show the evolution with time of the control and state energy. The time response of the tip and voltage history for the 0° actuation orientation is also included for comparison in Figures 4.21 and 4.22.

Table 4.4 summarizes the time response of the configurations to the gust. A minimum “maximum state energy times control cost” ratio means the regulator is able to dampen down the deflections on the wing with less actuation, thus giving a more effective controller in terms of gust alleviation. The reason for this parameter will be explained in detail in the following subsection. As one can see in the table, the bending actuation is the most effective way of achieving such gust alleviation. In fact, even the less direct way of realizing bending actuation through the $\pm 45^\circ$ actuation orientation in bending is more effective than the twist actuation configurations. The settling time, however, is significantly shorter for the twist actuation configurations due to the unstable condition (15% above flutter speed).

Table 4.4 Effect of the actuation orientation on the response settling time due to a gust disturbance of a wing flying at 15% above corresponding flutter speed and for a 2° root angle of attack.

Gust Freq.	Gust Amplitude	Actuation orientation	ρ	Control Cost (Jc) [m ³ ·s]	State Cost (Js) [J·s]	Settling time [s]	Max. State Energy [J]	MaxSE·Jc (x1e3) [J·m ³ ·s]
3 Hz	5.7 m/s	0°	1.2589E+00	8.0405E-05	7.6329	0.3956	49.8641	4.0093
	5.4 m/s	22° (B)	1.1220E+00	9.1358E-05	7.2650	0.4712	45.6848	4.1737
	5.4 m/s	22° (T)	3.3884E-01	3.4083E-04	4.1659	0.8136	23.5121	8.0136
	5 m/s	45° (B)	5.6234E-01	9.8248E-05	7.7726	0.5370	44.4597	4.3681
	5 m/s	45° (T)	3.1623E-01	4.0350E-04	3.4138	1.0925	17.4684	7.0485

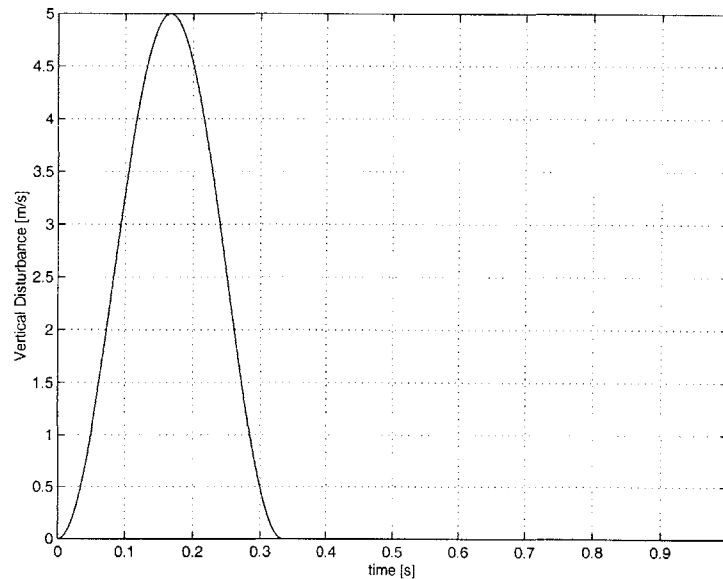


Figure 4.14 Profile of the ‘1-Cosine’ gust disturbance (5 m/s, 3 Hz).

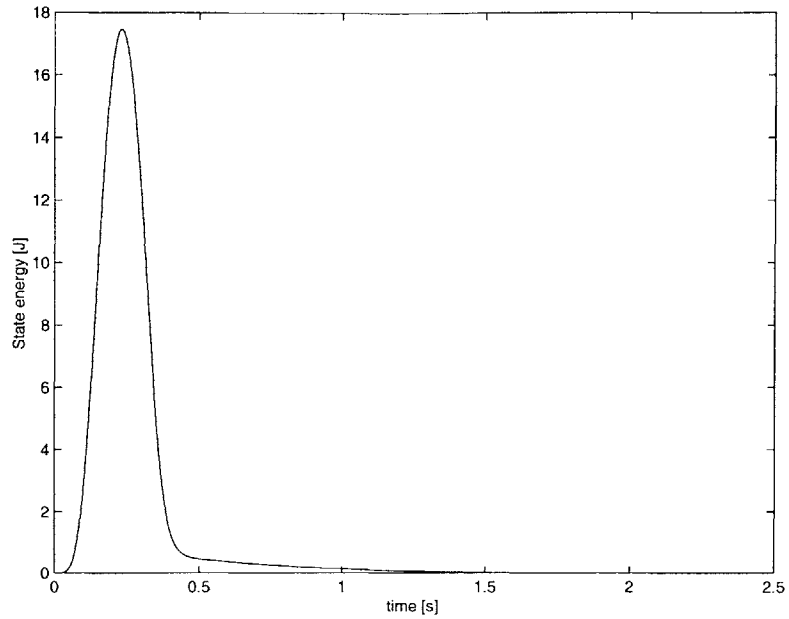


Figure 4.15 State energy for actuation oriented at $\pm 45^\circ$ actuated in torsion under a 5 m/s, 3 Hz gust disturbance at 15% above flutter speed and wing at 2° root angle of attack.

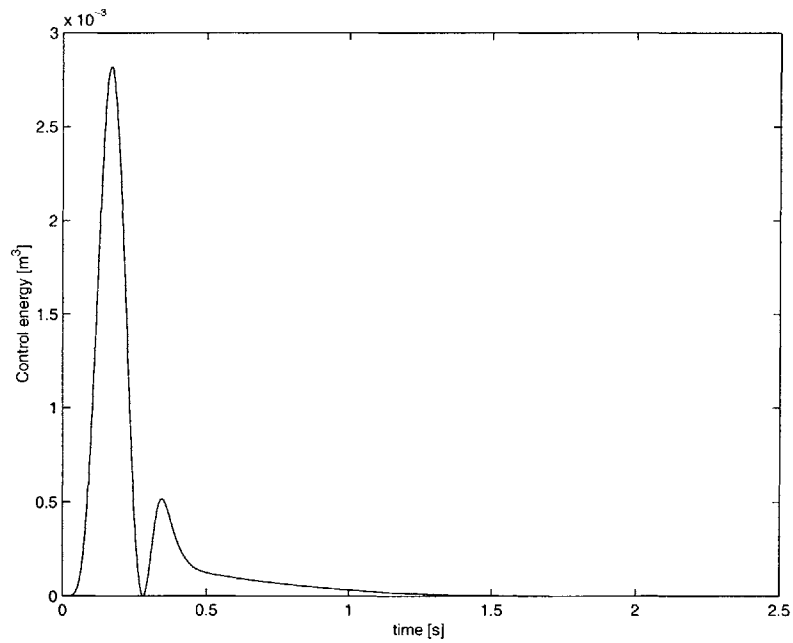


Figure 4.16 Control energy for actuation oriented at $\pm 45^\circ$ actuated in torsion under a 5 m/s, 3 Hz gust disturbance at 15% above flutter speed and wing at 2° root angle of attack.

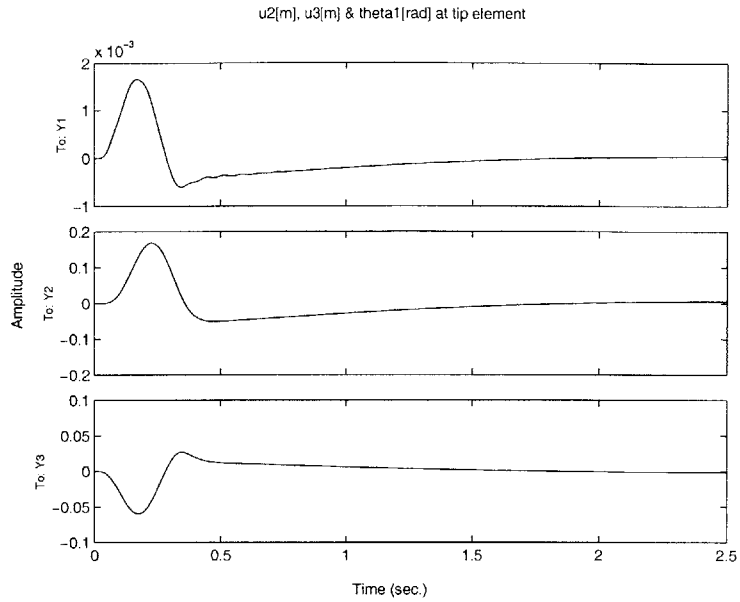


Figure 4.17 Gust alleviation for twist actuation oriented at $\pm 45^\circ$. (i) chordwise tip deflection (u_2), (ii) flatwise tip deflection (u_3), (iii) tip rotation (θ_3). Gust frequency is 3 Hz at 15% above flutter speed and root angle of attack is 2° .

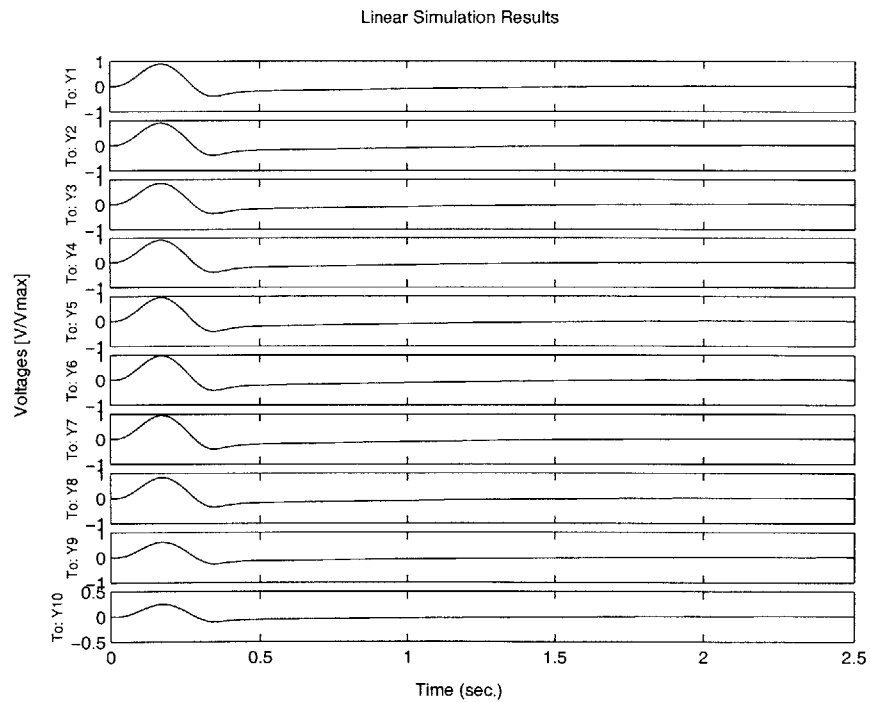


Figure 4.18 Voltage history for twist actuation oriented at $\pm 45^\circ$ under a 3 Hz gust disturbance at 15% above flutter speed, and 2° root angle of attack.

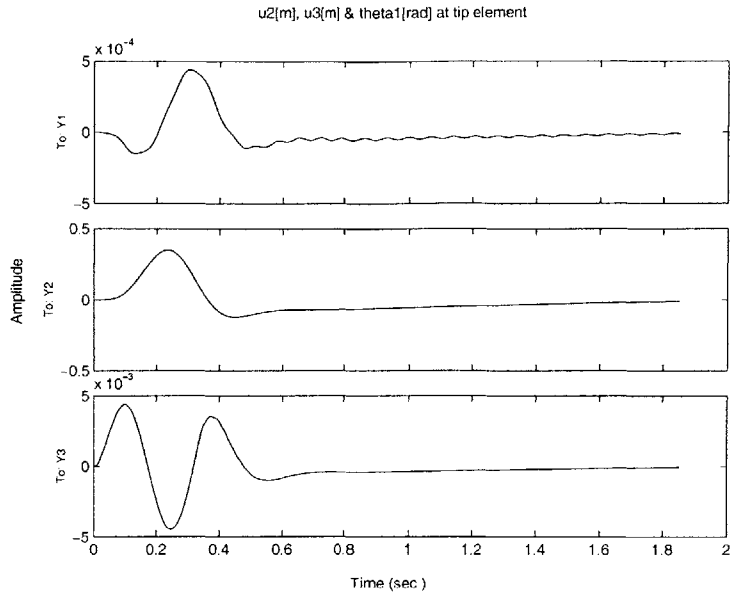


Figure 4.19 Gust alleviation for bending actuation oriented at $\pm 45^\circ$. (i) chordwise tip deflection (u_2), (ii) flatwise tip deflection (u_3), (iii) tip rotation (θ_3). Gust frequency is 3 Hz at 15% above flutter speed and root angle of attack is 2° .

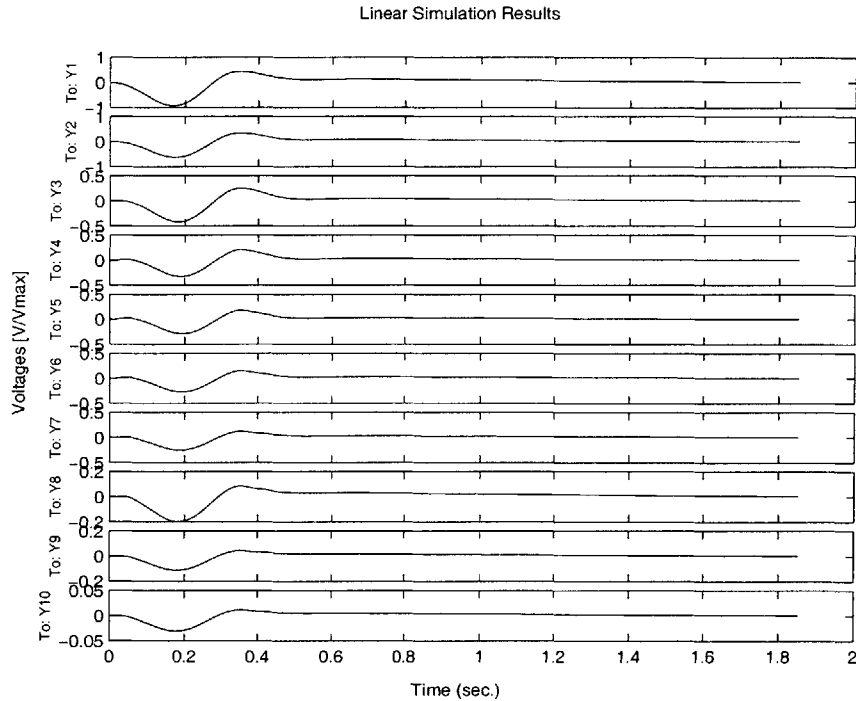


Figure 4.20 Voltage history for bending actuation oriented at $\pm 45^\circ$ under a 3 Hz gust disturbance at 15% above flutter speed, and 2° root angle of attack.

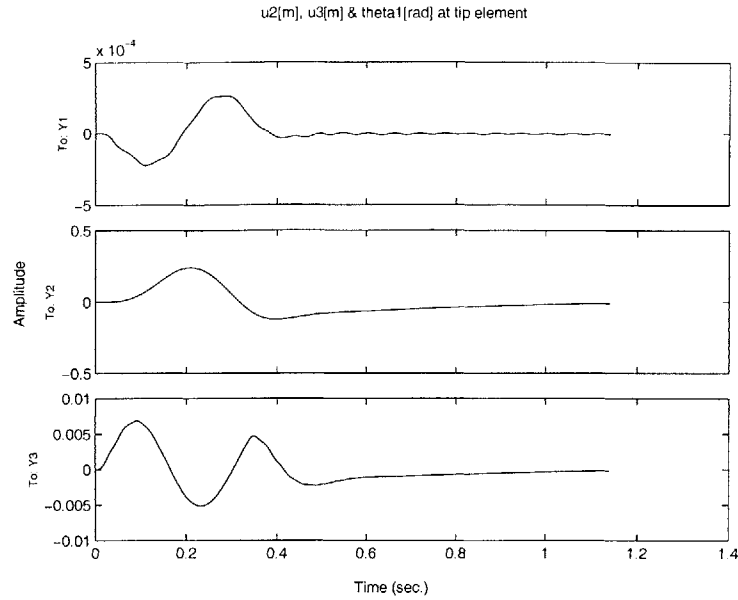


Figure 4.21 Gust alleviation for bending actuation oriented at 0° . (i) chordwise tip deflection (u_2), (ii) flatwise tip deflection (u_3), (iii) tip rotation (θ_3). Gust frequency is 3 Hz at 15% above flutter speed and root angle of attack is 2° .

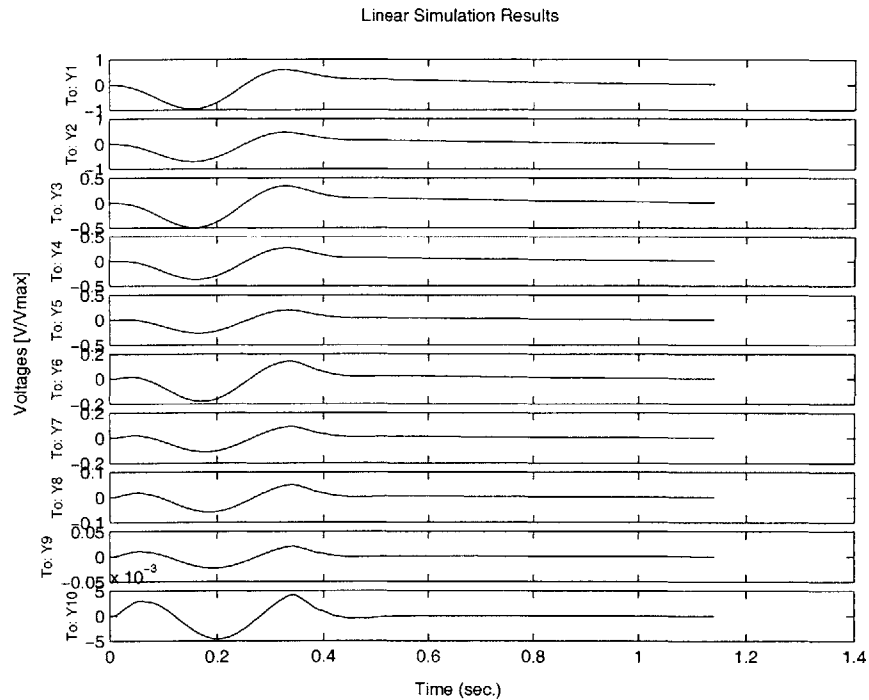


Figure 4.22 Voltage history for bending actuation oriented at 0° under a 3 Hz gust disturbance at 15% above flutter speed, and 2° root angle of attack.

4.3.2.2.2 Wing Flying Below Flutter Speed

Rejecting a gust at speeds over flutter gives information on the robustness of the regulator, but it is perhaps more useful in practice to study the effect of gust rejection below flutter. Consider now the same configurations discussed before but now flying at 15% below flutter speed. So, stability is not a concern at this point, and all the energy of the actuators can be concentrated in rejecting the gust. Table 4.5 summarizes the results. The low frequency of the gust is expected to primarily excite the first bending mode, but the results in Table 4.5 indicate that actuating in torsion yields shorter settling times and lower maximum state energy than actuating in bending. The reason is that the implementation of the system does not let the actuators saturate, and a closer look to the voltage distribution would show that actuating in bending quickly saturates the root actuator while the voltage level in the other regions is still low. Ideally, the root element would saturate and the rest of the elements would be allowed to draw more voltage, making the bending actuation more effective. The metric “maximum state energy times control cost” can be used to account for this limitation.

Another option is to have less individually controlled actuation regions, that is, from the current 10 regions, to two or one. Section 4.3.3 discusses the effect of different number of independently actuated regions within this non-saturation condition. Moreover, the much higher control cost required by the actuation in torsion confirms the fact that the bending actuation configurations are not driving as much control energy as available. Looking at the results for the “maximum state energy times control cost” metric presented in the last column of Table 4.5, it is obvious that bending-actuated configurations are more effective for gust rejection, providing smaller “maximum state energy times control cost.” Very low values are obtained by all the orientations in bending in the expected order: 0° , $\pm 22^\circ$, and $\pm 45^\circ$. The performance of the two configurations actuated in torsion is well behind those actuated in bending.

Figures 4.23 to 4.32 show the time responses of the tip of the wing as well as the voltage history for every orientation. Notice that the maximum tip twist amplitude is higher in the torsion configuration than in the bending ones. This is due to the fact that the twist actuation configurations use exactly the wing twist to control the flatwise bending motion.

Table 4.5 Effect of the actuation orientation on the response settling time due to a gust disturbance of a wing flying at 15% below corresponding flutter speed and for a 2° root angle of attack.

Gust Freq.	Gust Amplitude	Actuation orientation	ρ	Control Cost (Jc) [m ³ ·s]	State Cost (Js) [J·s]	Settling time [s]	Max. State Energy [J]	MaxSE·Jc (x1e3) [J·m ³ ·s]
3 Hz	5.7 m/s	0°	1.0471E+00	1.9718E-04	4.5075	0.4741	29.779	5.8718
	5.4 m/s	22° (B)	1.0000E+00	2.0796E-04	4.4771	0.5049	28.2691	5.8788
	5.4 m/s	22° (T)	2.8184E-01	6.0258E-04	3.3131	0.4059	20.2847	12.2232
	5 m/s	45° (B)	4.5709E-01	2.8822E-04	5.2665	0.5720	29.6361	8.5417
	5 m/s	45° (T)	2.5119E-01	7.5492E-04	3.0596	0.6290	16.8474	12.7184

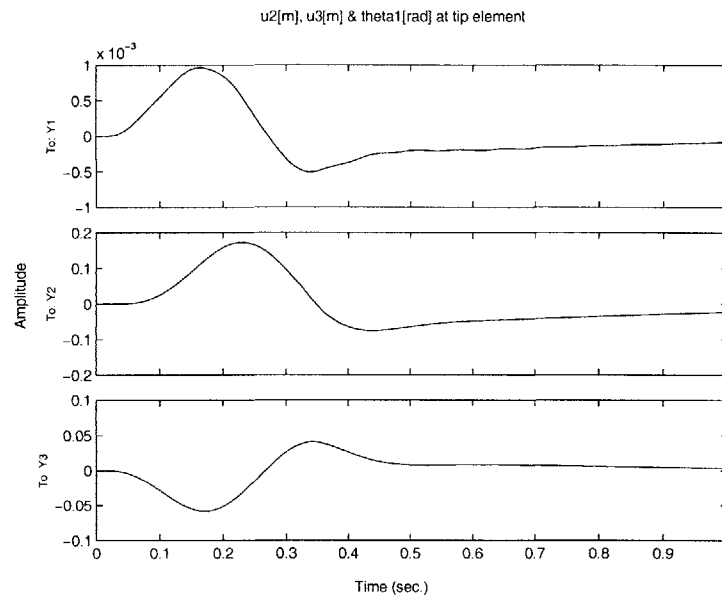


Figure 4.23 Gust alleviation for twist actuation oriented at $\pm 45^\circ$. (i) chordwise tip deflection (u_2), (ii) flatwise tip deflection (u_3), (iii) tip rotation (θ_3). Gust frequency is 3 Hz at 15% below flutter speed and root angle of attack is 2°.

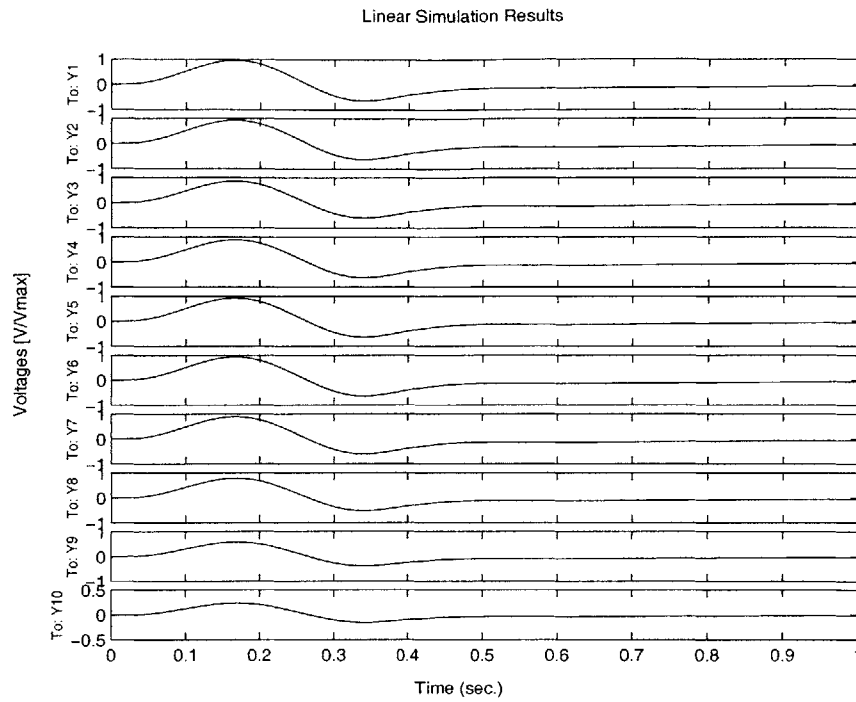


Figure 4.24 Voltage history for twist actuation oriented at $\pm 45^\circ$ under a 3 Hz gust disturbance at 15% below flutter speed, and 2° root angle of attack.

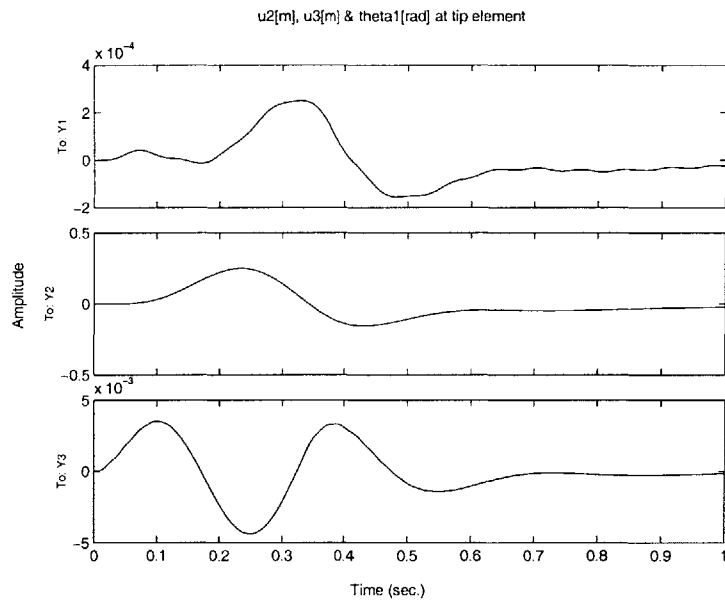


Figure 4.25 Gust alleviation for bending actuation oriented at $\pm 45^\circ$. (i) chordwise tip deflection (u_2), (ii) flatwise tip deflection (u_3), (iii) tip rotation (θ_3). Gust frequency is 3 Hz at 15% below flutter speed and root angle of attack is 2° .

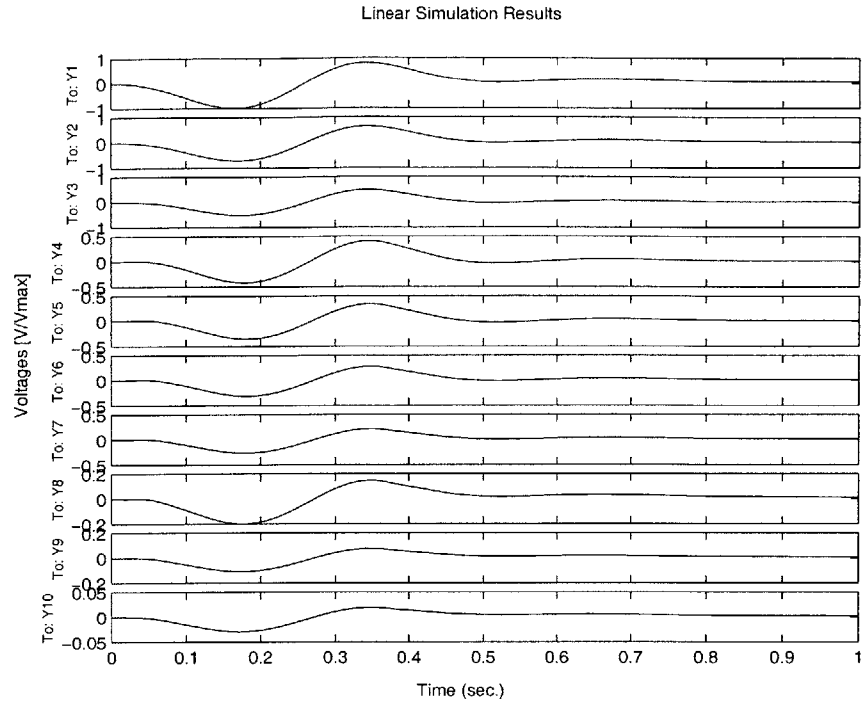


Figure 4.26 Voltage history for bending actuation oriented at $\pm 45^\circ$ under a 3 Hz gust disturbance at 15% below flutter speed, and 2° root angle of attack.

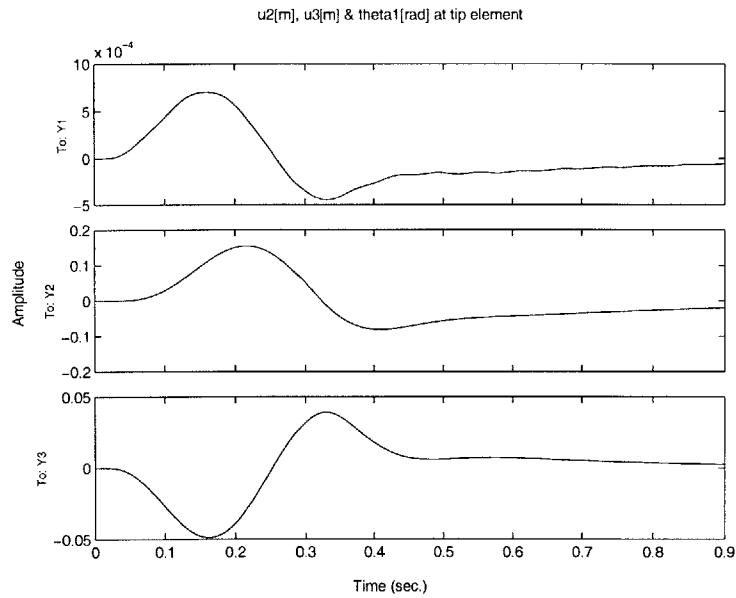


Figure 4.27 Gust alleviation for twist actuation oriented at $\pm 22^\circ$. (i) chordwise tip deflection (u_2), (ii) flatwise tip deflection (u_3), (iii) tip rotation (θ_3). Gust frequency is 3 Hz at 15% below flutter speed and root angle of attack is 2° .

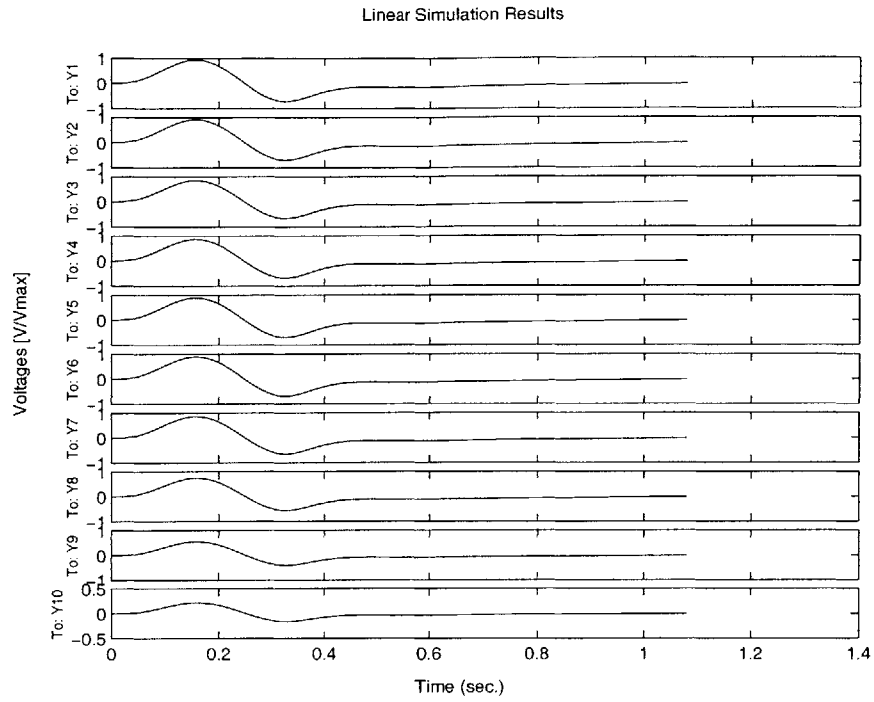


Figure 4.28 Voltage history for twist actuation oriented at $\pm 22^\circ$ under a 3 Hz gust disturbance at 15% below flutter speed, and 2° root angle of attack.

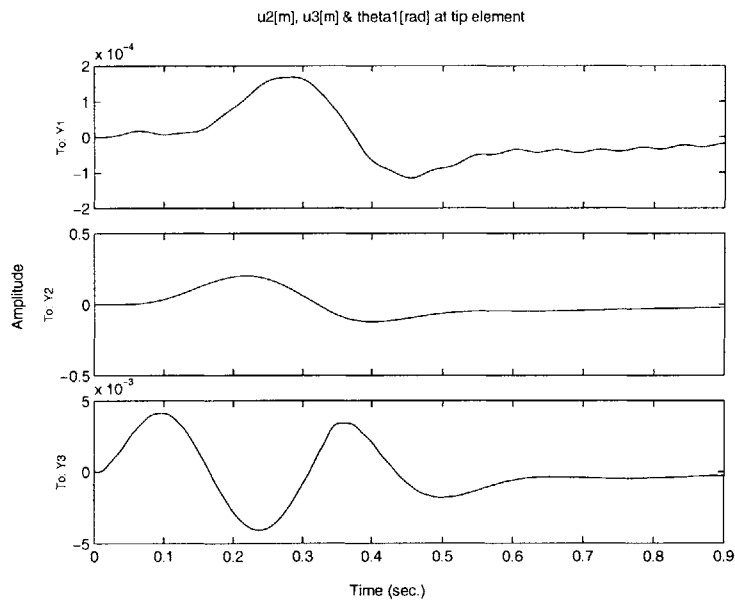


Figure 4.29 Gust alleviation for bending actuation oriented at $\pm 22^\circ$. (i) chordwise tip deflection (u_2), (ii) flatwise tip deflection (u_3), (iii) tip rotation (θ_3). Gust frequency is 3 Hz at 15% below flutter speed and root angle of attack is 2° .

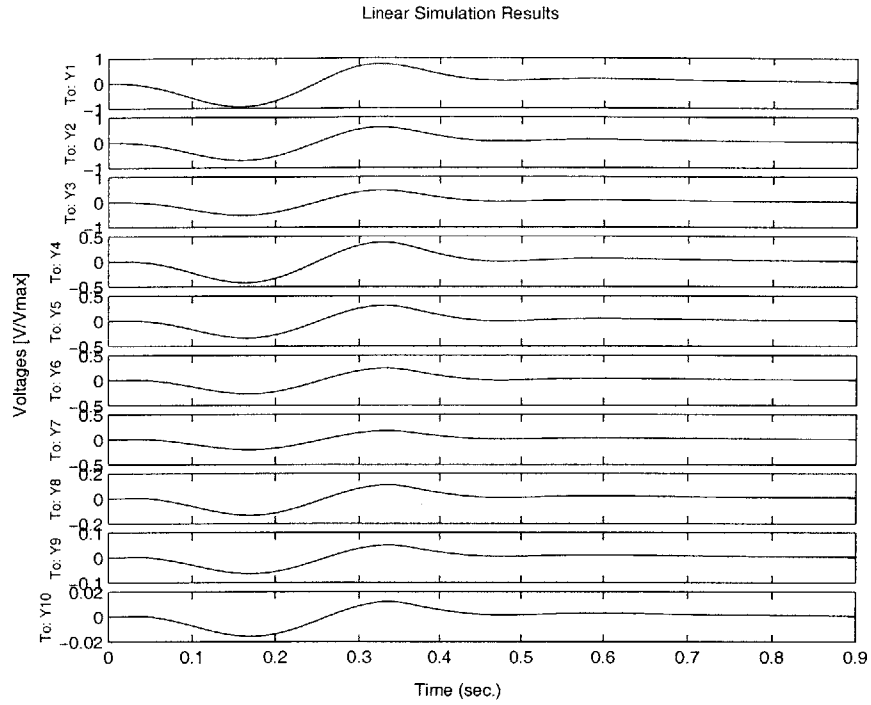


Figure 4.30 Voltage history for bending actuation oriented at $\pm 22^\circ$ under a 3 Hz gust disturbance at 15% below flutter speed, and 2° root angle of attack.

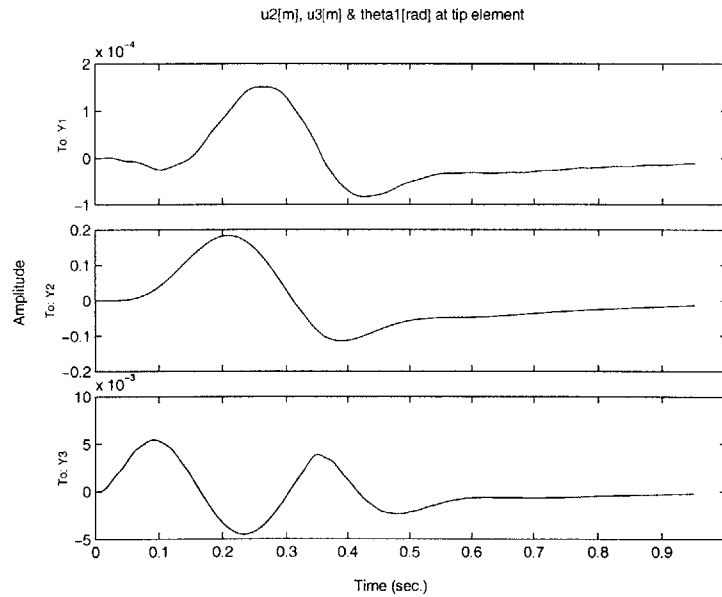


Figure 4.31 Gust alleviation for bending actuation oriented at 0° . (i) chordwise tip deflection (u_2), (ii) flatwise tip deflection (u_3), (iii) tip rotation (θ_3). Gust frequency is 3 Hz at 15% below flutter speed and root angle of attack is 2° .

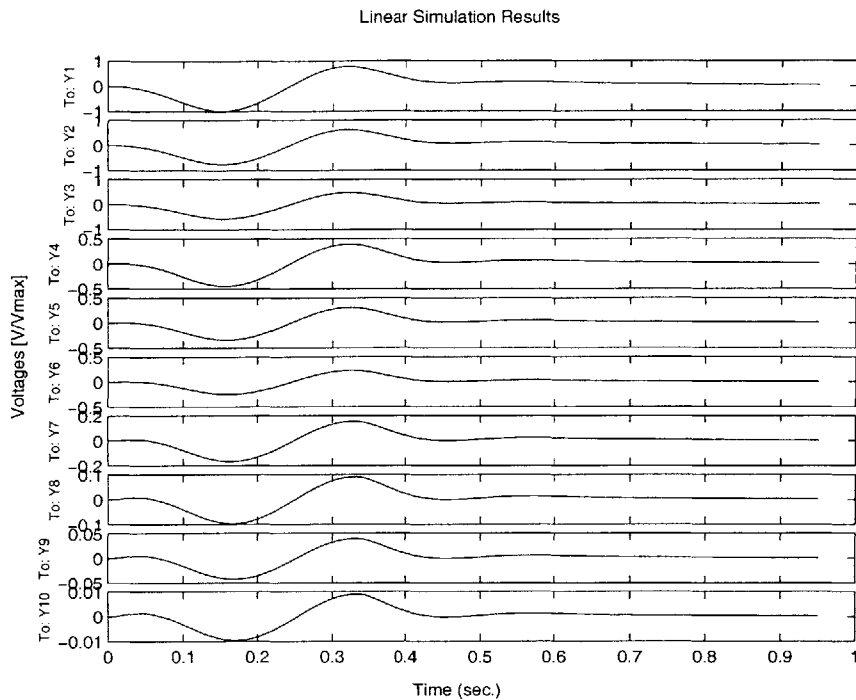


Figure 4.32 Voltage history for bending actuation oriented at 0° under a 3 Hz gust disturbance at 15% below flutter speed, and 2° root angle of attack.

4.3.3 The Effect of Multiple Control Regions

It seems to agree with intuition that the more actuators that we can control independently, the better. Grouping all actuators into a single control (that is, identically actuating all of them with the same phase and magnitude) only provides controllability of very low order structural modes. The question is how much better can be done by further dividing them into a higher number of smaller regions.

As done before, the theory and implementation described in Section 3.8 is used. Four configurations have been chosen: 1, 2, 5 and 10 active regions. One active region means that all actuators are excited simultaneously, while 10 means that every actuator in every element is powered independently (in terms of magnitude only). The configuration used in this section is the following:

- The root angle of attack is set to 2° .

- The actuation is oriented at $\pm 45^\circ$ (maximum twist actuation).
- One sensor of each type is placed in every element, that is, a bending strain gauge, a torsion strain gauge, and an accelerometer.

4.3.3.1 The Effect of Multiple Control Regions on Stability

Following the procedure used in the previous sections, one obtains the results shown in Figure 4.33. Increasing the number of zones does reduce the minimum cost needed for stability, though not linearly. Increasing the actuation regions from 5 to 10 does not improve much the performance, and they practically coincide in the graph. The reason is that 5 regions approximate very well the first torsion mode of the cantilever wing that is the one requiring stability enhancement. Higher actuator distribution than that has very low impact on the final distribution of voltage on the actuators.

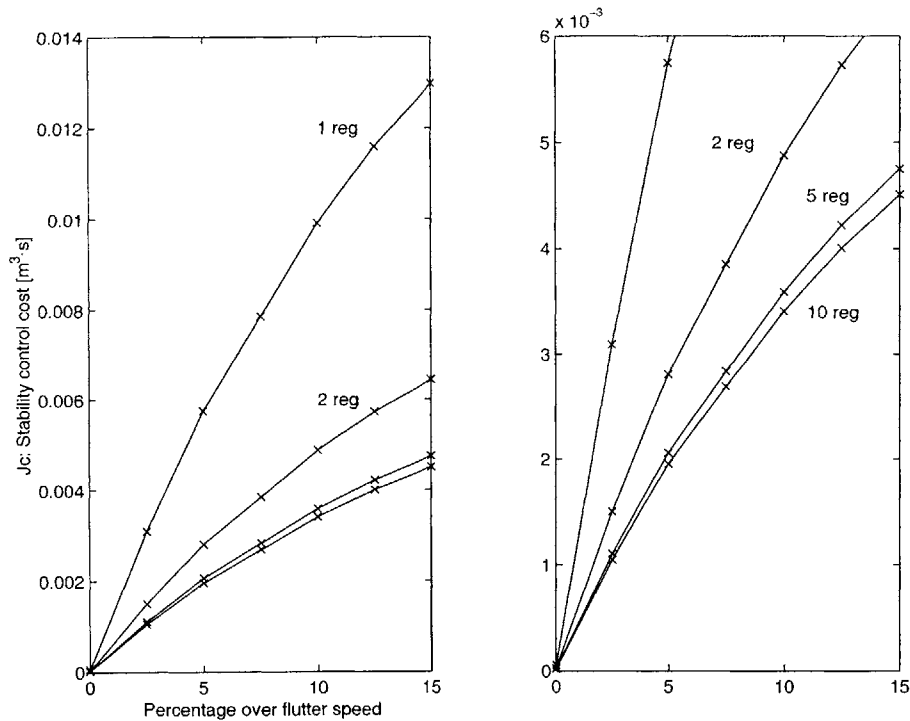


Figure 4.33 Normalized stability control cost vs. percentage over flutter speed for the wing flying at 2° root angle of attack (zoomed on the right) for different number of twist active regions.

4.3.3.2 The Effect of Multiple Control Regions on Gust Alleviation

Tables 4.6 and 4.7 show the settling times for the (1-Cosine) gust disturbance both above and below flutter, respectively. The same pattern observed in the stability control study where higher numbers of regions improved the cost response, is also visible in the gust alleviation case. By looking at both tables, one can verify that a higher number of active regions yields shorter rejection times, the reason being the possibility for the active forcing to both extend its actuation to higher modes and better excite the lower ones.

Table 4.6 Effect of the number of twist active regions on the response settling time due to a gust disturbance of a wing flying at 15% above corresponding flutter speed and for a 2° root angle of attack

Gust Freq.	Gust Amplitude	Active Regions	ρ	Control Cost (Jc) [m ³ ·s]	State Cost (Js) [J·s]	Settling time [s]	Max. State Energy [J]	MaxSE·Jc (x1e3) [J·m ³ ·s]
3 Hz	5 m/s	1 region	5.8884E+00	2.6147E-04	4.1976	0.8920	22.9229	5.9937
		2 regions	3.1623E+00	2.6852E-04	4.1002	0.9230	22.2804	5.9827
		5 regions	1.2589E+00	2.7019E-04	4.0182	0.9450	21.7336	5.8722
		10 regions	6.3096E-01	2.1010E-04	4.0063	0.9475	21.6543	4.5496

Table 4.7 Effect of the number of twist active regions on the response settling time due to a gust disturbance of a wing flying at 15% below corresponding flutter speed and for a 2° root angle of attack

Gust Freq.	Gust Amplitude	Active Regions	ρ	Control Cost (Jc) [m ³ ·s]	State Cost (Js) [J·s]	Settling time [s]	Max. State Energy [J]	MaxSE·Jc (x1e3) [J·m ³ ·s]
3 Hz	5 m/s	1 region	9.1201E+00	2.4025E-04	4.1696	0.5220	23.7411	5.7038
		2 regions	4.8978E+00	2.3540E-04	4.1447	0.5230	23.5954	5.5544
		5 regions	1.9953E+00	2.3282E-04	4.1182	0.5210	23.4500	5.4596
		10 regions	1.0000E+00	2.3295E-04	4.1113	0.5210	23.4113	5.4537

4.3.4 The Effect of Sensor Type and Placement

As explained in Section 3.4.1, there are three types of sensors available: bending strain gauges, torsion strain gauges, and accelerometers. Every element in the discretization can have any combination of these three.

The type and especially the placement of the sensors are fundamental for the performance of the controller. One must remember that in the LQG the full state is not

known, and it has to be estimated from the available information coming from the sensors. Obviously, the more the sensors, the better. An ideal situation under the given conditions would be to have the two types of strain gauges plus an accelerometer in every element. The candidate locations for the accelerometers are obviously away from the root, where element displacements are greater. More interesting is to investigate the placement of the two types of strain gauges. Thus, a configuration with a strain gauge of every type in every element is the baseline for this part of the study. In addition, two other configurations are tested that try to take advantage of the knowledge of the behavior of the structure. Finally, these four configurations will be compared against a maximum sensing distribution with all possible strain gauges and accelerometers mounted.

As described in Section 3.4.2, sensor placement benefits from knowledge of the structural modes. Appendix B explained how to obtain the structural modes of the structure. In order to maximize their sensing, the strain gauges should be placed at the maximum curvature locations. (Refer to Appendix B for a way to obtain the approximate bending and torsion modes.) This is essentially a preliminary step in order to obtain the maximum curvature location along the span for every one of the first few modes. Since the bending and torsion sensors actually measure the curvature, placing the strain gauges at those locations guarantees maximum (and therefore optimum) sensing within the simplifying assumptions.

The bending and torsion modes are shown in Figures 4.34 and 4.35 along with their curvatures. Table 4.8 summarizes the maximum curvature information obtained from the plots.

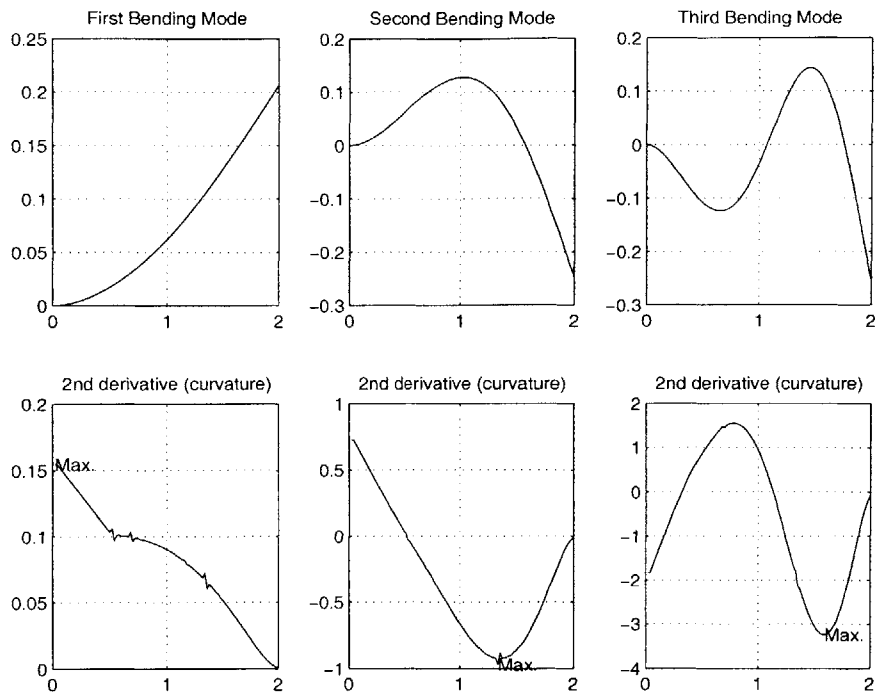


Figure 4.34 First bending modes and their curvatures with the actuators oriented at $\pm 45^\circ$.

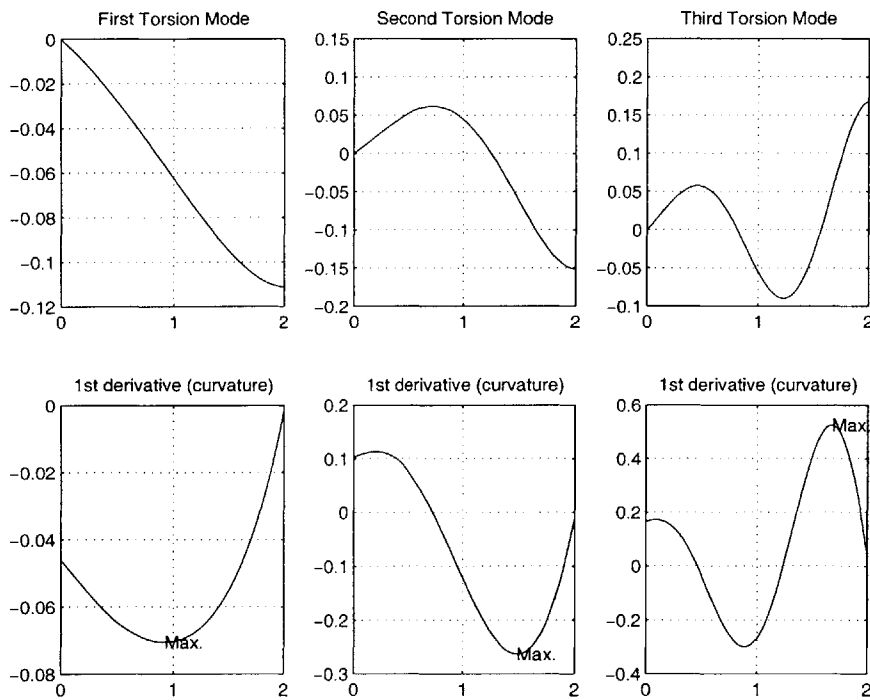


Figure 4.35 First torsion modes and their curvatures with the actuators oriented at $\pm 45^\circ$.

Table 4.8 Location of the maximum curvature for the first three modes

	Bending [m]	Torsion [m]
1st	0	0.92
2nd	1.34	1.49
3rd	1.6	1.68

This information allows to place the strain gauges as depicted in Figure 4.36, showing only the best location for every bending or torsion mode. Only the first three modes are considered.

If a minimal set of sensors wants to be used in order to avoid manufacturing complexity, it is rational to use just one to detect the first torsion mode, which is the unstable mode. For the same reason, it is also interesting to have a bending strain gauge to measure the second bending mode, which coalesces with the first torsion mode in flutter. Due to the low frequency component of gusts, which excite the low energy bending modes, it also makes sense to have a bending strain gauge at the root measuring the first bending mode. These three cases are compared with the “full strain gauge sensing mode”, which assumes the two type of strain gauges placed at every element in the wing, and with a “maximum” mode which is equivalent to the “full” strain gauge sensing mode plus all possible accelerometers.

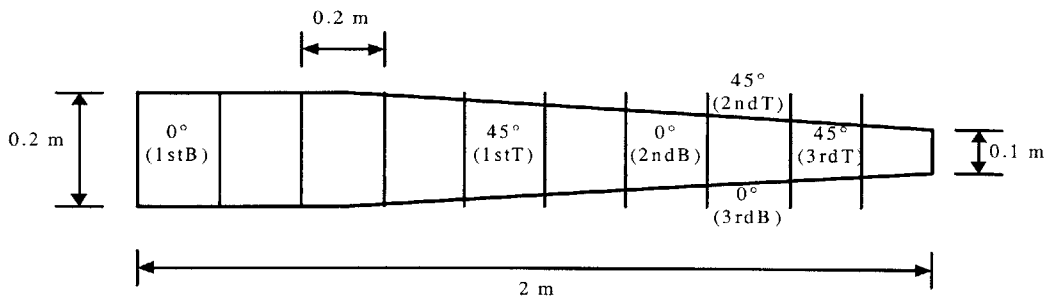


Figure 4.36 Optimum locations if one strain gauge is used to sense each bending or torsion mode for a wing divided into 10 elements.

4.3.4.1 The Effect of Sensor Type and Placement on Stability

Consider the wing flying at 15% above flutter speed with twist actuation oriented at $\pm 45^\circ$. The control cost required to stabilize the wing for every type of sensor is shown in Figure 4.37. It can be inferred from the plot that having a strain gauge sensing the first torsion mode is almost equivalent to having one sensing the second bending mode. One must remember that those are the two modes coalescing in flutter, thus making sense to use them in stabilizing the wing. The first bending mode is not an effective way of stabilizing the plant, since it is not directly related to the instability as Figure 4.37 clearly demonstrates. The plot also shows the effect of adding the accelerometers to a wing with full strain gauge sensing. The stability control cost can be successfully reduced in half at 15% above flutter by adding the accelerometers.

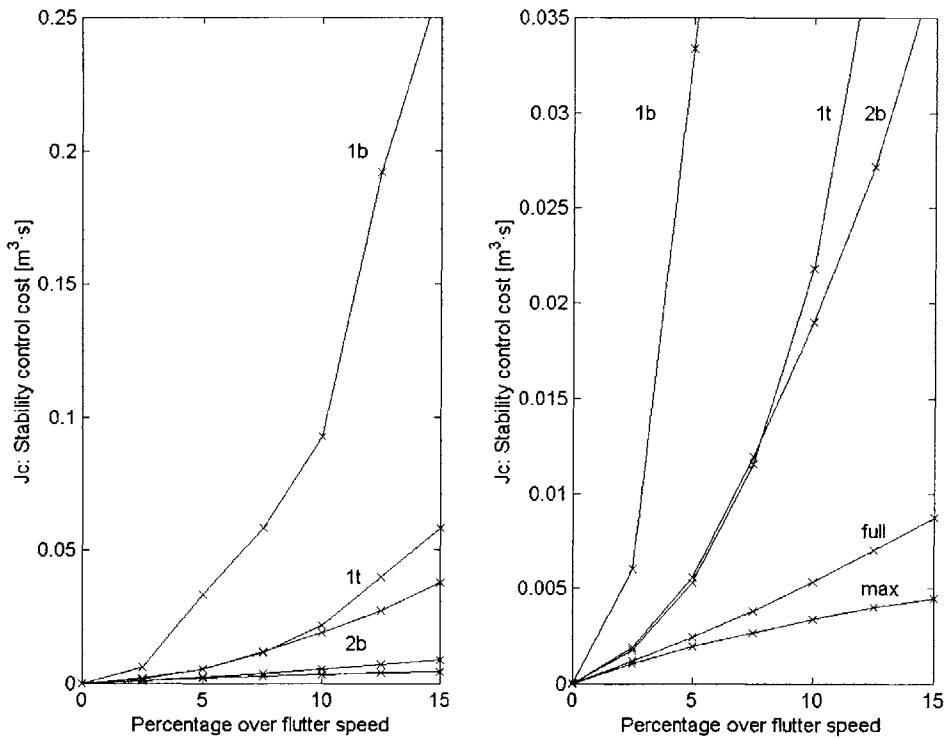


Figure 4.37 Stability control cost for five sensor configurations (“max” means the three types of sensors are present in each element; “full” implies there is a bending and a torsion sensor in each element; “1t” means first torsion, “1b” means first bending and “2b” means second bending).

4.3.4.2 The Effect of Sensor Type and Placement on Gust Alleviation

Table 4.9 details the settling times resulting when the wing is disturbed by the 3 Hz gust. The configuration is the same as in the stability study. The ratio “maximum state energy times control cost” is not needed in this table because, except for the maximum sensing case, all cases are far from saturating the actuators. By inspection of the table, one realizes that having maximum sensing greatly improves gust alleviation and reduces the maximum state energy in the wing in the process. The rest of the options entail similar settling times. The full strain gauge sensing option takes slightly less time than the second bending strain gauge, even though at a slightly higher cost. This explanation lies in the better knowledge of the wing behavior that the full sensing provides, which allows the controller to better react to the disturbance at the expense of a little more actuation cost. In fact, due to the high low frequency content of the gust, which significantly affect the bending modes, it is a very cost effective solution to use bending strain gauges in the configuration. Notice, however, that detecting the second bending mode is effective only in this particular configuration due to the fact that it is involved in the flutter coalescence. This advantage will disappear when the wing is flown below flutter speed.

Table 4.9 Effect of the sensor placement on the response settling time due to a gust disturbance of a wing flying at 15% above corresponding flutter speed and for a 2° root angle of attack.

Gust Freq.	Gust Amplitude	Sensor Detection	ρ	Control Cost (Jc) [m ³ ·s]	State Cost (Js) [J·s]	Settling time [s]	Max. State Energy [J]
3 Hz	5 m/s	Maximum	6.3096E-01	2.1010E-04	4.0063	0.9475	21.6543
		Full	3.1623E-05	1.0961E-08	8.2861	0.7367	47.2498
		1st Torsion	3.1623E-05	9.7625E-10	8.2956	0.7380	47.2986
		1st Bending	3.1623E-05	3.9474E-07	8.2931	0.7370	47.2847
		2nd Bending	3.1623E-05	3.1749E-08	8.2856	0.7370	47.2420

The results for a speed 15% below flutter (see Table 4.10) are very similar to the ones in Table 4.9, except for the second bending mode. Since the configuration is now stable *per se*, measuring the second bending mode is no longer that effective. The full strain gauge case is the best choice as expected (other than the maximum sensing option,

obviously), and again, it is more helpful to detect the first bending mode than the first torsion mode.

Table 4.10 Effect of the sensor placement on the response settling time due to a gust disturbance of a wing flying at 15% below corresponding flutter speed and for a 2° root angle of attack.

Gust Freq.	Gust Amplitude	Sensor Detection	ρ	Control Cost (Jc) [m ³ -s]	State Cost (Js) [J-s]	Settling time [s]	Max. State Energy [J]
3 Hz	5 m/s	Maximum	1.0000E+00	2.3295E-04	4.1113	0.5210	23.4113
		Full	3.1623E-05	1.2009E-08	5.8858	0.9017	32.5345
		1st Torsion	3.1623E-05	1.7999E-15	5.8876	0.9033	32.5276
		1st Bending	3.1623E-05	6.9895E-11	5.8873	0.9033	32.5277
		2nd Bending	3.1623E-05	8.0860E-11	5.8875	0.9033	32.5287

4.3.5 Robustness Check

This chapter has proven the soundness of the regulator working on a linearized plant about a non-linear equilibrium. But the non-linearities intrinsic to the plant require a particularly robust regulator. Ideally, the linear regulator would be tested against a completely non-linear plant to check its solidity, but this is clearly beyond the scope of the present work. Nevertheless, a simple check can be made using the linear plant to get a flavor of the robustness of the linear regulator. In essence, a regulator is designed around a linearized plant above flutter, for a given airspeed or angle of attack. Then, either the speed or the angle are varied and another linearized plant is obtained, but the original regulator is the one applied to the new plant. In other words, one regulator designed in a given flight condition is checked at some other setting. A robust regulator should be able to withstand the change of the new plant (i.e., to a new speed or angle of attack).

A regulator is therefore designed around the following wing configuration:

- The root angle of attack is set at 2°.
- The actuators are oriented at ±45°.
- The number of active regions is set to 10, that is, every element is an independently actuated zone.

- One sensor of each type is placed in every element, that is, a bending strain gauge, a torsion strain gauge, and an accelerometer.

4.3.5.1 Robustness of the Regulator under Changes in the Airspeed

The regulator is designed at 7.5% over the flutter speed and then tested on speeds that range from 0% to 15% above flutter. The stability control cost required to stabilize the plant under those conditions is shown in Figure 4.38. Note that if the speed is increased beyond the design speed (7.5%), the regulator is unable to stabilize the plant.

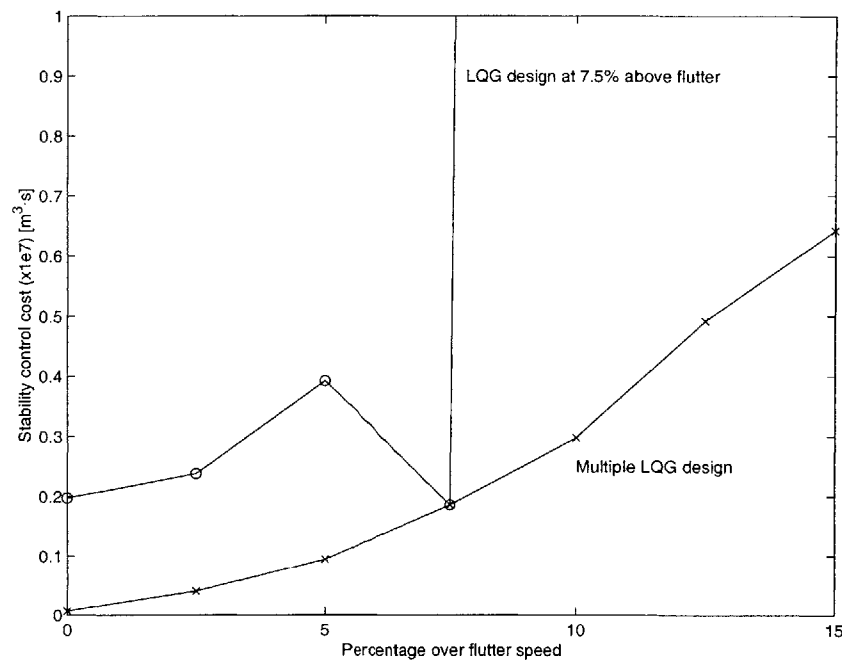


Figure 4.38 Stability control cost for a regulator designed at 7.5% over flutter speed and tested at other speeds.

Considering the multiple LQG design as the nominal design cost, one can translate these values into percentages over the nominal cost (see Figure 4.39). The stabilization cost is several times the nominal value for speeds between 0% and 7.5% over the flutter speed. Beyond that speed, the system is unstable as mentioned above. The flying conditions are therefore too demanding for the regulator to stabilize the plant for speeds

outside the LQG regulator design airspeed. A future study should try the possibility, for example, of a simple nonlinear controller designed as a dynamic gain scheduling.

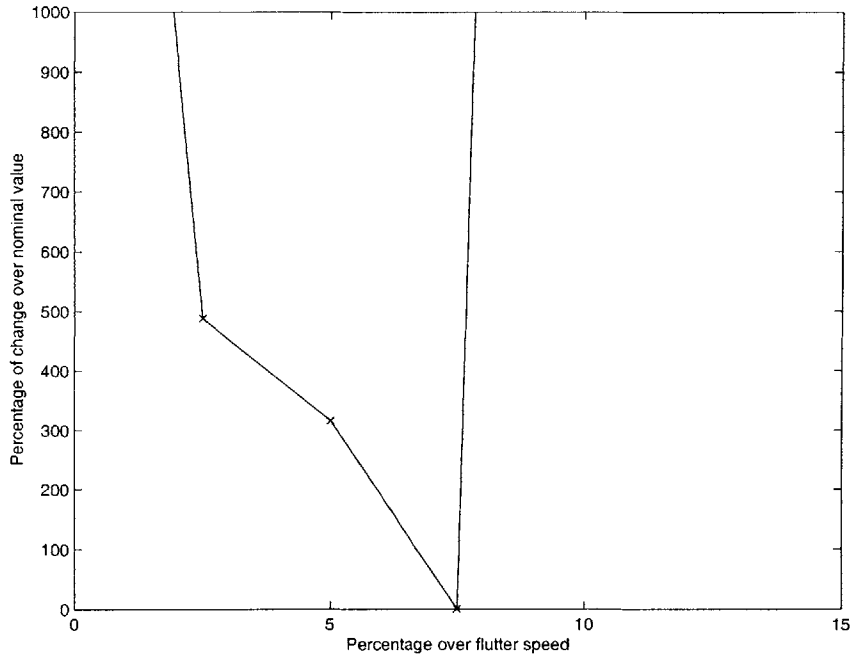


Figure 4.39 Percentage over the nominal stability control cost for a regulator designed at 7.5% over flutter speed and tested at other speeds.

4.3.5.2 Robustness of the Regulator under Changes in the Root Angle of Attack

An identical check is tried now for the same conditions but for a LQG designed at a specified root angle of attack (2°) also at a 7.5% over flutter speed. The angle at the wing root is varied $\pm 2^\circ$ around the specified value, resulting on the plot shown in Figure 4.40. This is a much worse scenario, as inferred by the vertical scale of the plot. The regulator is extremely sensible to changes in the angle of attack. In those conditions, one can conclude that the regulator will lack enough robustness to control the plant, since the required stabilization control increases by several orders of magnitude very quickly.

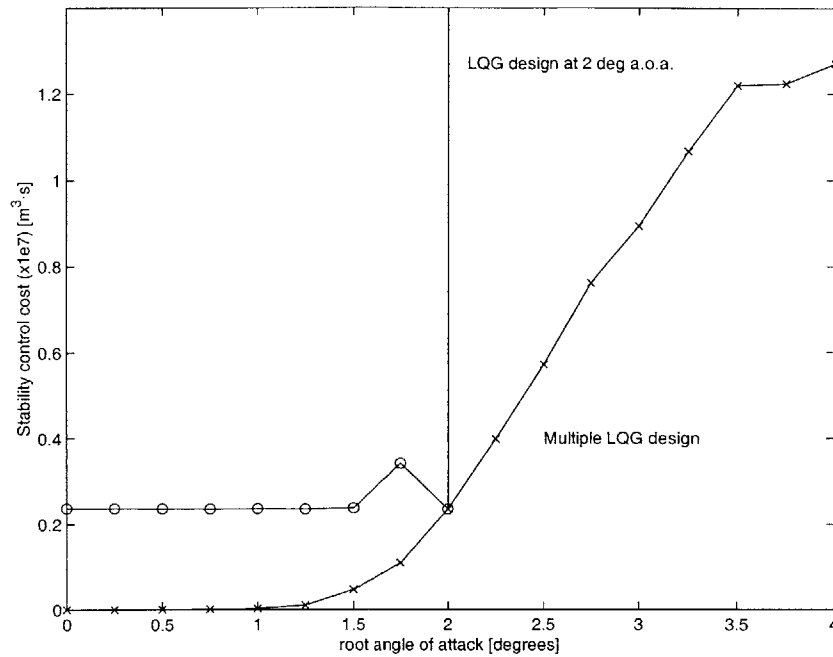


Figure 4.40 Stability control cost for a regulator designed at 2° root angle of attack and 7.5% over flutter speed and tested at a ±2° interval.

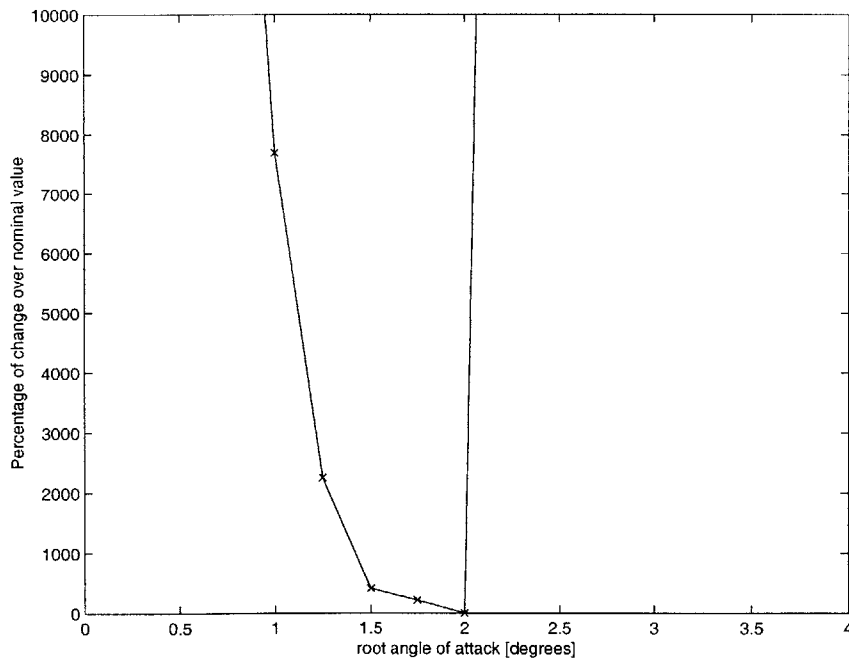


Figure 4.41 Percentage over the nominal stability control cost for a regulator designed at 2° angle root of attack and 7.5% over flutter speed and tested at a ±2° interval.

Chapter 5

Conclusions

An integrated framework to study the aeroelastic response of highly flexible active wings was presented. The framework consists of three main pillars: the active aeroelastic analysis, the control design block and a simulator. The present work successfully combines the three in a complete environment that offers the designer both aeroelastic analysis and tailoring capability, providing potential ways to understand the mechanisms of active aeroelastic response and instability of such wings.

The low-order, high-fidelity aeroelastic model effectively handles the non-linearity inherent in the structure and in the aerodynamics. It consists of an asymptotically correct active cross-sectional formulation, geometrically-exact mixed formulation for dynamics of moving beams, and a finite-state unsteady aerodynamics with the ONERA dynamic stall model. It represents the link between the physical model and the controller by providing a linearized plant about a non-linear equilibrium. For this purpose, a wing can be trimmed at a given flight speed and the deformations are calculated. The resulting state-space equations are then used in the control design and simulation.

The cross-sectional model is able to analyze general (thin-walled, thick-walled, solid) non-homogeneous and non-isotropic beams with embedded anisotropic actuation. It is an asymptotical analysis that reduces the original three-dimensional electroelastic formulation to a one-dimensional problem. The two dimensions eliminated from the problem are replaced by a stiffness matrix and an actuation vector. The developed analysis is then validated against several test cases: two box-beams, one single cell NACA 0012 wing, the two-cell Active Twist Rotot (ATR) prototype blade, and the 1/6th Mach-scale CH-47D blade section. All of the cases employed active fiber composites (AFC) embedded in the structure for actuation purposes. Comparison of the present formulation with another asymptotical analysis (limited to multi-cell thin-walled beams) shows very good correlation, and discrepancies are within the limitations of the thin-

walled approximation. Comparison of the present analysis with experimental twist actuation shows somewhat conflicting results. The correlation was extremely good for the simple airfoil-shape cross section and the complex CH-47D blade section, but inconclusive for the ATR blade. The reason for the latter is believed to be a combination of difficulties on the characterization of the active material properties, as well as the limitations on the linear piezoelectric model used to characterize the behavior of piezoelectric fiber composites on a more complex structure.

In order to test the impact of parameter variation in flight performance, a representative HALE-type composite wing was selected. The actuation was also obtained by means of active fiber composites. The open loop performance of the wing was studied first to determine the onset of flutter and the structural modes involved. The effect of varying the root angle of attack was included in this research, showing that the flutter speed decreases as the angle increases. Variations in the angle of attack may also change the modes that coalesce in flutter. A Linear Quadratic Gaussian (LQR) regulator was chosen as a potential method for controlling the structure, where only a limited number of states were available for feedback. Even though the LQG regulator is a robust controller when distributed sensing is involved around a linear plant, it has proven not to be robust enough over variations about a specified flight condition above flutter speed in the present nonlinear model.

Different controllers were simulated for set flight velocities in order to study the impact of parameter variation in the aeroelastic performance. Firstly, the impact of the orientation of the actuators was studied. Due to their anisotropy, one of the conclusions of the research was that the stiffness properties of the wing vary as the actuation is rotated thus changing the stability boundary. Setting the orientation of the actuation to $\pm 45^\circ$ and actuating it in torsion reduces the control required to stabilize the structure by maximizing the twist-authority. When gust alleviation is concerned, the closer the orientation is to 0° , the easier the disturbance is rejected. For other orientations, the aeroelastic response to gust improves if the AFCs are actuated in bending, since the bending frequencies are most excited by gust due to its low-frequency content.

Secondly, the investigation focused on the grouping of the piezoelectrics. Increasing the number of zones does reduce the minimum cost needed for stability, but the

improvement is small beyond 5 regions. The reason is that 5 regions already approximate very well the first torsion mode of the cantilever wing that is the one requiring stability enhancement, but higher actuator distribution than that has very low impact on the final distribution of voltage on the actuators. A higher number of active regions also yields shorter gust rejection times and less kinetic and potential energy in the wing, since the active forcing can both extend its actuation to higher modes and more accurately excite the lower ones.

Thirdly, research was carried out into the observability of the system. Proper placement of the sensors helps in reducing the total number of sensors with a minimum performance penalty in estimating the states. Sensing the modes that coalesce in flutter was the most effective approach, particularly sensing the unstable mode. The study showed that a single strain gauge measuring that mode is enough to stabilize the wing, with a performance closer than expected to that of full bending and torsion sensing. However, adding the accelerometers to the wing dramatically increases the observability and stabilization of the system. As far as gust rejection is involved, sensing the bending modes proves to be the most effective solution, particularly the first bending mode.

The results conclude that anisotropic strain actuation tailoring is successful in improving the performance of high aspect ratio wings, in particular in controlling linear aeroelastic instabilities and performing gust alleviation. By carefully orienting the embedded actuators in independent regions, placing the right type of sensors, and selecting the electric field profile, a single configuration may be able to satisfy all the requirements for performance on stability augmentation and gust alleviation.

Fundamental conclusions have been drawn from the control design. Firstly, the stability margin of operation in flutter can be increased within the limits of the embedded actuators. Secondly, the regulator has proven to be effective in rejecting gust disturbances even above the flutter speed. And thirdly, the control design method allows the optimization of the amount of actuation required. Unfortunately, the control methodology used in the present study was unable to deal with the nonlinearities of the plant.

Finally, the research itself confirmed the two-dimensional simulator as a valuable virtual environment where any desired configurations can be validated.

Chapter 6

Future Work

The present work pretends to be a complete analysis environment, which should not only facilitate the design of high aspect ratio wings, but also the study and understanding of their aeroelastic response.

An integral analysis environment is a tremendous task, and it should not surprise the reader to learn that there is room for improvement and additions. The LQG regulator has proven to be efficient for linear plants. However, preliminary tests indicated that the LQG is not robust enough to the levels of change in the plant as experienced in this nonlinear aeroelastic case. Future work should look into nonlinear controllers and their effectiveness for the present problem.

The present work has considered several actuation orientations (0° , $\pm 22^\circ$, and $\pm 45^\circ$), actuated either in bending or in torsion. This implicitly assumes all actuators simultaneously operated with the same electric field pattern to obtain either bending or twist along the span. But an interesting studied could be carried out in which some of the regions would be actuated in bending and others in torsion. This could better adapt the strain actuation to whatever mode or modes were necessary to be controlled, providing a more effective aeroelastic control system.

In all numerical examples, active fiber composites have been used as the means to provide strain actuation (even though the formulation is not restricted to this). The simple robustness check has made apparent the limitations in terms of maximum strain actuation of the currently available AFC packs. The effectiveness of the regulator would undoubtedly benefit from any improvements on the active response of that media.

The present closed loop simulator implementation in Matlab relies on a convenient built-in function to perform the numerical integration necessary to obtain the time response of the system to a disturbance. It does not allow, however, saturation of the

actuators or the possibility to trigger the regulator at a time other than the initial time. The Simulink implementation of the simulators overcomes these limitations, but there is a much higher computational time associated with Simulink's versatility. Future work is necessary to develop a more flexible numerical integration scheme to handle these features.

There are some details in the current numerical implementation that could be improved. In particular, there are two aspects of the mesh generator which would benefit from further coding: (i) improvement of the 6-node element mesh generator so that it properly handles the interior region of the airfoil, and (ii) improvement of the "Pro-Engineer"- "VABS-A" interface for the 8-node element meshes.

The computer front-end developed to completely integrate and automate the presented design tool is general enough to handle all the cases presented here. However, more work could be put into the Tk code to improve the user interface. An example would be to have a refined file opening dialog window and an improved file tracking system that would allow working from any directory.

Bibliography

- [1] Dunn, P. and Dugundji, J., "Nonlinear Stall Flutter and Divergence Analysis of Cantilevered Graphite/Epoxy Wings," *AIAA Journal*, Vol. 30, No. 1, Jan. 1992, pp. 153-162.
- [2] Tang, D. M., and Dowell, E. H., "Experimental and Theoretical Study of Non-linear Aeroelastic Behavior of Flexible Rotor Blades," *AIAA Journal*, Vol. 31, No. 6, Jun. 1993, pp. 1133-1142.
- [3] Virgin, L. N. and Dowell, E. H., "Nonlinear Aeroelasticity and Chaos," In Atluri, S. N., editor, *Computational Nonlinear Mechanics in Aerospace Engineering*, Chapter 15. AIAA, Washington, DC, 1992.
- [4] Cesnik, C. E. S. and Shin, S.-J., "Structural Analysis for Designing Rotor Blades With Integral Actuators," in *Proceedings of the 39th Structures, Structural Dynamics, and Materials Conference*, Long Beach, California, 370 L'Enfant Promenade, S.W., Washington, D.C. 20024, April 20-23 1998, American Institute of Aeronautics and Astronautics, AIAA Paper No. 98-2107.
- [5] Cesnik, C. E. S., Hodges, D. H., and Patil, M. J., "Aeroelastic Analysis of Composite Wings," In *Proceedings of the 37th Structures, Structural Dynamics, and Materials Conference*, Salt Lake City, Utah, April 18-19, 1996.
- [6] Patil, M. J., Hodges, D. H., and Cesnik, C. E. S., "Nonlinear Aeroelasticity Analysis of High Aspect Ratio Wings," In *Proceedings of the 38th Structures, Structural Dynamics, and Materials Conference*, Long Beach, California, April 1998.
- [7] Livne, E., "Integrated Aeroservoelastic Optimization: Status and Directions," In *Proceedings of the 38th AIAA Structures, Structural Dynamics, and Materials Conference*, Kissimmee, Florida, April 1997, AIAA 97-1409.
- [8] Loewy, R. G., "Recent Developments in Smart Structures with Aeronautical Applications," In *Proceedings of the 37th Israel Annual Conference on Aerospace Sciences*, February 26-27, 1997.

- [9] Pendleton, E. W., Griffin, K. E., Kehoe, M., and Perry, B., "A Flight Research Program for the Active Aeroelastic Wing Concept," In *Proceedings of the 37th AIAA Structures, Structural Dynamics, and Materials Conference*, Salt Lake City, Utah, April 1996.
- [10] duPlessis, A. J. and Hagood, N. W., "Modeling and Experimental Testing of Twist Actuated Single Cell Composite Beams for Helicopter Blade Control," AMSL #96-1, Massachusetts Institute of Technology, Feb. 1996.
- [11] Kudva, J. N., *et al*, "Overview of the ARPA/WL 'Smart Structures and Material Development - Smart Wing' Contract," In *Proceedings of the SPIE Smart Structures, and Materials*, Vol. 2721, San Diego, California, Feb. 1996.
- [12] McGowan, A. R., Heeg, J., Lake, R., "Results of Wind-Tunnel Testing from the Piezoelectric Aeroelastic Response Tailoring Investigation," In *Proceedings of the 37th AIAA Structures, Structural Dynamics, and Materials Conference*, Salt Lake City, Utah, April 1996.
- [13] Lin, C.Y. and Crawley, E.F., "Design Considerations for a Strain Actuated Adaptive Wing for Aeroelastic Control," *Proceedings of the Fourth International Conference on Adaptive Structures*, Cologne, Germany, 1993.
- [14] Lazarus, K. B., Crawley, E. F., and Lin, C. Y., "Multivariable Active Lifting Surface Control Using Strain Actuation: Analytical and Experimental Results," *Journal of Aircraft*, Vol. 34, No. 3, May-June 1997, pp. 313-321.
- [15] Lin, C. Y., "Towards Optimal Strain Actuated Aeroelastic Control," PhD Thesis, Department of Aeronautics and Astronautics, M.I.T., Cambridge, MA, Jan. 1996, M.I.T. SERC Report #3-96.
- [16] How, J. P., Haddad, W. M., and Hall, S. R., "Application of Popov Controller Synthesis to Benchmark Problems with Real Parameter Uncertainty," *Journal of the Guidance, Control, and Dynamics*, July-August 1994, pp. 759-768.
- [17] How, J. P., Hall, S. R., and Haddad, W. M., "Robust Controllers for the Middeck Active Control Experiment Using Popov Controller Synthesis," *IEEE Transactions on Control Systems Technology*, 2(2), 1994.

- [18] Hodges, D. H., "A Mixed Variational Formulation Based on Exact Intrinsic Equations for Dynamics of Moving Beams," *International Journal of Solids and Structures*, Vol. 26, No. 11, 1990, pp. 1253-1273.
- [19] Peters, D. A. and Johnson, M. J., "Finite-State Airloads for Deformable Airfoils on Fixed and Rotating Wings," In *Symposium on Aeroelasticity and Fluid/Structure Interaction, Proceedings of the Winter Annual Meeting*. ASME, November 6-11, 1994.
- [20] Peters, D. A., Barwey, D., and Johnson, M. J., "Finite-State Airloads Modeling with Compressibility and Unsteady Free-Stream," In *Proceedings of the Sixth International Workshop on Dynamics and Aeroelastic Stability Modeling of Rotorcraft Systems*, November 8-10, 1995.
- [21] Shang, X. and Hodges, D. H., "Aeroelastic Stability of Composite Rotor Blades in Hover," In *Proceedings of the 36th Structures, Structural Dynamics and Materials Conference*, New Orleans, Louisiana, April 10-12, 1995, pp. 2602-2610, AIAA Paper 95-1453.
- [22] Hodges, D. H., Atilgan, A. R., Cesnik, C. E. S., and Fulton, M. V., "On a Simplified Strain Energy Function for Geometrically Nonlinear Behaviour of Anisotropic Beams," *Composites Engineering*, Vol. 2, No. 5-7, 1992, pp. 513-526.
- [23] Cesnik, C. E. S., and Ortega-Morales, M., "Active Composite Beam Cross-Sectional Modeling--Stiffness and Active Force Constants," in *Proceedings of the 40th AIAA/ASCE/AHS/ASC Structures, Structural Dynamics and Materials Conference*, St. Louis, Missouri, April 12-15, 1999.
- [24] Peters, D. A., Karunamoorthy, S., and Cao, W. M., "Finite State Induced Flow Models; Part I : Two-Dimensional Thin Airfoil," *Journal of Aircraft*, Vol. 32, No. 2, Mar.-Apr. 1995, pp. 313-322.
- [25] Hodges, D. H., Shang, X., and Cesnik, C. E. S., "Finite Element Solution of Nonlinear Intrinsic Equations for Curved Composite Beams," *Journal of the American Helicopter Society*, Vol. 41, No. 4, Oct. 1996, pp. 313-321.
- [26] Cesnik, C. E. S. and Hodges, D. H., "VABS: A New Concept for Composite Rotor Blade Cross-Sectional Modeling," *Journal of the American Helicopter Society*, Vol. 42, No. 1, 1997, pp. 27-38.

- [27] Berdichevsky, V. L., "On the Energy of an Elastic Rod," *PMM*, Vol. 45, 1982, pp. 518-529.
- [28] Rehfield, Lawrence W., "Design Analysis Methodology for Composite Rotor Blades," in *Proceedings of the Seventh DoD/NASA Conference on Fibrous Composites in Structural Design*, Denver, CO, June 1985, Grant NAG-2-238.
- [29] Song, O. and Librescu, L., "Vibrational Behavior of Rotating Helicopter Blades Incorporating Adaptive Capabilities," in *Proceedings of the SPIE Symposium on Smart Structures and Materials*, Vol. 1917, Part 1, 1993.
- [30] Wilkie, W. K., Belvin, W., and Park, K. C., "Aeroelastic Analysis of Helicopter Rotor Blade Incorporating Anisotropic Piezoelectric Twist Actuator," in *Proceedings of ASME World Congress and Exposition*, 1996.
- [31] Giese, C. L., Reich, G. W., Hopkins, M. A., and Griffin, K. E., "An investigation of the Aeroelastic Tailoring of Smart Structures Concepts," In *Proceedings of the 37th AIAA Structures, Structural Dynamics, and Materials Conference*, Salt Lake City, Utah, April 1996.
- [32] Gilliatt, H. C., Strganac, T. W., and Kurdila, A. J., "Nonlinear Aeroelastic Response of an Airfoil," In *Proceedings of the 35th Aerospace Sciences Meeting and Exhibit*, Reno, Nevada, Jan. 1997.
- [33] Cesnik, C. E. S. and Shin, S.-J., "On the Cross-Sectional Modeling of Active Helicopter Blades," in *Proceedings of PACAM VI*, Rio de Janeiro, Brazil, January 4-8, 1999.
- [34] Danielson, D. A. and Hodges, D. H., "Nonlinear Beam Kinematics by Decomposition of the Rotation Tensor," *Journal of Applied Mechanics*, Vol. 54, No. 2, 1987, pp. 258-262.
- [35] Anon., "IEEE Standard on Piezoelectricity," Technical Report Std. 176-1978, The Institute of Electrical and Electronics Engineers, 1978, pp. 9-14.
- [36] Crandall, S. H., Karnopp, D. C., Kurtz, Jr. E. F., and Pridmore-Brown, D. C., "Dynamics of Mechanical and Electromechanical Systems," Robert E. Kreiger Publishing Co., Malabar, Florida, 1968.

- [37] Cesnik, C. E. S., "Cross-Sectional Analysis of Initially Twisted and Curved Composite Beams," Ph.D. Thesis, Aerospace Engineering, Georgia Institute of Technology, May 1994.
- [38] Bent, A. A. and Hagood, N. W., "Piezoelectric Fiber Composites with Interdigitated Electrodes," *Journal of Intelligent Material Systems and Structures*, 1996.
- [39] Rodgers, J. P., Hagood, N. W., and Weems, D. B., "Design and Manufacture of an Integral Twist-Actuated Rotor Blade," in *Proceedings of the 38th AIAA Structures, Structural Dynamics and Materials Conference*, Kissimmee, Florida, 1997, AIAA Paper No. 97-1264.
- [40] Rodgers, J. P., Bent, A. A., and Hagood, N. W., "Characterization of Interdigitated Electrode Piezoelectric Fiber Composites Under High Electrical and Mechanical Loading," in *Proceedings of the Society of Photo-Optical and Instrumentation Engineers*, San Diego, California, 1996.
- [41] Cesnik, C. E. S., Shin, S.-J., Wilkie, W. K., Wilbur, M. L., and Mirick, P. H., "Modeling, Design and Testing of the NASA/ARMY/MIT Active Twist Rotor Prototype Blade," in *Proceedings of the American Helicopter Society 55th Annual Forum*, Montreal, Canada, May 25-27, 1999.
- [42] Cesnik, C. E. S., Shin, S.-J., "On the Twist Performance of a Multiple-Cell Active Helicopter Blade," in *Proceedings of the 9th Conference on Adaptive Structures and Technologies*, Boston, Massachusetts, October 14-18 1998, pp. 193-202.
- [43] "Shephard's: Unmanned Vehicles Handbook," The Shephard Pres, UK, 1998.
- [44] Kenneth Munson, Editor, "Jane's: Unmanned Aerial Vehicles and Targets," Jane's Information Group Ltd., UK, 1998.
- [45] Bisplinghoff R. L., and Ashley, H., "Principles of Aeroelasticity," Dover, 1962.
- [46] Patil, M. J., "Nonlinear Aeroelastic Analysis, Flight Dynamics, and Control of a Complete Aircraft," Ph.D. Thesis, Aerospace Engineering, Georgia Institute of Technology, May 1999.
- [47] Bernstein, D. S. and Haddad, W. M. "Multivariable Control-System Synthesis: The Fixed-Structure Approach," preprint.
- [48] Analytic Sciences Corporation, Technical Staff, "Applied Optimal Estimation," Cambridge, Mass., M.I.T. Press, 1974.

- [49] Giurgiutiu V., and Rogers, C. A., "Review of Smart-Materials Actuation Solutions for Aeroelastic and Vibration Control," in *Proceedings of the CEAS/AIAA/ICASE/NASA Langley International Forum on Aeroelasticity and Structural Dynamics 1999*, Williamsburg, Virginia, June 22-25, 1999.
- [50] Dowell, E. H. (Editor), Crawley, E. F., Curtiss Jr., H.C., Peters, D. A., Scanlan, R. H., and Sisto, Fernando, "A Modern Course in Aeroelasticity," third revised and enlarged edition, Kluwer Academic Publishers, The Netherlands, 1994.
- [51] Chen, P. C. and Chopra, I., "Wind Tunnel Test of a Smart Rotor Model with Individual Blade Twist Control," *SPIE* Vol. 3041, pp.217-229, 1997.
- [52] Rodgers, J. P., and Hagood, N. W., "Preliminary Mach-Scale Hover Testing of an Integrated Twist-Actuated Rotor Blade," *SPIE* Vol. 3329, pp.291-308, 1998.
- [53] Millott, T. A., and Friedmann, P. P., "Vibration Reduction in Hingeless Rotors in Forward Flight Using an Actively Controlled Trailing Edge Flap: Implementation and Time Domain Simulation," *Proceedings of the AIAA/ASME/ASCE/AHS/ASC 35th Structures, Structural Dynamics and Materials Conference*, Hilton Head, SC, April 18-20, 1994, paper AIAA-94-1306-CP, pp. 8-22.
- [54] Patil, M. J., Hodges, D. H., and Cesnik, C. E. S., "Nonlinear Aeroelasticity and Flight Dynamics of High-Altitude Long Endurance Aircraft," In *Proceedings of the 40th Structures, Structural Dynamics, and Materials Conference*, St. Louis, Missouri, April 1999.
- [55] Ousterhout, J. K., "Tcl and the Tk toolkit," Addison-Wesley, Reading, Mass., c1994.
- [56] Hall, S. R. and Prechl, E. F., "Preliminary Testing of a Mach-Scaled Active Rotor Blade with a Trailing Edge Servo-Flap," *SPIE Smart Structures and Materials Symposium*, Newport Beach, CA, 1-5 March 1999, paper #3668-03
- [57] Ogata, K., "Modern Control Engineering," Prentice-Hall, Inc., Upper Saddle River, NJ, 1997.
- [58] J.P. How, Robust Control Design with Real Parameter Uncertainty using Absolute Stability Theory. PhD thesis, Department of Aeronautics and Astronautics, M.I.T., Cambridge, MA, Feb. 1993. M.I.T. SERC Report #1-93.

- [59] Schaub, H. and Junkins, J. L., "Stereographic Orientation Parameters for Attitude Dynamics: A Generalization of the Rodrigues Parameters," *Journal of the Astronautical Sciences*, Vol. 44, No. 1, Jan.-Mar. 1996, pp. 1-19.
- [60] Drela, M., "Integrated Simulation Model for Preliminary Aerodynamic, Structural, and Control-Law Design of Aircraft," in *Proceedings of the 40th AIAA/ASCE/AHS/ASC Structures, Structural Dynamics and Materials Conference*, St. Louis, Missouri, April 12-15, 1999, AIAA paper # 99-1394.

Appendix A

Cross-Sectional Properties for the Wind Tunnel Model (NACA 0014)

Table A.1 Material properties for the wind tunnel model's cross section (NACA 0014).

	E-Glass	AFC
E_1 (GPa)	19.3	42.2
E_2 (GPa)	19.3	17.5
E_3 (GPa)	9.8	17.5
G_{12} (GPa)	4.1	5.5
G_{13} (GPa)	4.1	5.5
G_{23} (GPa)	3.28	4.4
ν_{12}	0.148	0.354
ν_{13}	0.148	0.354
ν_{23}	0.207	0.496
Thickness (mm)	0.1143	0.127
d_{11} (pm/V)	-	309
d_{12} (pm/V)	-	-129
electrode dist. (mm)	-	1.143

Mass (m)

Units: [Kg/m].

- Elements 1-3:

0.4000

- Element 4:

0.3733

- Element 5:

0.3467

- Element 6:

0.3200

- Element 7:

0.2933

- Element 8:

0.2667

- Element 9:

0.2400

- Element 10:

0.2133

Center of gravity offset

Center of gravity offset with respect to the reference axes, located at 30% of the chord, expressed as (spanwise, chordwise, up/down).

Units: [m].

- Elements 1-3:

0.00000E+00 -0.40000E-01 0.00000E+00

- Element 4:

0.00000E+00 -0.37330000E-01 0.00000E+00

- Element 5:

0.00000E+00 -0.34670000E-01 0.00000E+00

- Element 6:

0.00000E+00 -0.320000E-01 0.00000E+00

- Element 7:

0.00000E+00 -0.29330000E-01 0.00000E+00

- Element 8:

0.00000E+00 -0.26670000E-01 0.00000E+00

- Element 9:

0.00000E+00 -0.240000E-01 0.00000E+00

- Element 10:

0.00000E+00 -0.21330000E-01 0.00000E+00

Inertia Moment (I)

Units: [Kg·m].

- Elements 1-3:

0.40000E-02 0.00000E+00 0.00000E+00
0.00000E+00 0.59540E-05 0.00000E+00
0.00000E+00 0.00000E+00 0.38500E-02

- Element 4:

0.32520000E-02 0.00000E+00 0.00000E+00
0.00000E+00 0.59540E-05 0.00000E+00
0.00000E+00 0.00000E+00 0.38500E-02

- Element 5:

0.26040000E-02 0.00000E+00 0.00000E+00
0.00000E+00 0.59540E-05 0.00000E+00
0.00000E+00 0.00000E+00 0.38500E-02

- Element 6:

0.20480000E-02 0.00000E+00 0.00000E+00
0.00000E+00 0.59540E-05 0.00000E+00
0.00000E+00 0.00000E+00 0.38500E-02

- Element 7:

0.15770000E-02 0.00000E+00 0.00000E+00
0.00000E+00 0.59540E-05 0.00000E+00
0.00000E+00 0.00000E+00 0.38500E-02

- Element 8:

0.11840000E-02 0.00000E+00 0.00000E+00
0.00000E+00 0.59540E-05 0.00000E+00
0.00000E+00 0.00000E+00 0.38500E-02

- Element 9:

0.08640000E-02 0.00000E+00 0.00000E+00
0.00000E+00 0.59540E-05 0.00000E+00
0.00000E+00 0.00000E+00 0.38500E-02

- Element 10:

0.06100000E-02 0.00000E+00 0.00000E+00
0.00000E+00 0.59540E-05 0.00000E+00
0.00000E+00 0.00000E+00 0.38500E-02

Stiffness and actuation constants

Nomenclature:

Stiffness results: 1-extension; 2-twist; 3- and 4-bending

Actuation results: 1-Force; 2- 3- and 4-Moments

Units:

$$K(1,1) = [N], K(1,2) = [N \cdot m], K(1,3) = [N \cdot m], K(1,4) = [N \cdot m],$$

$$K(2,2) = [N \cdot m^2], K(2,3) = [N \cdot m^2], K(2,4) = [N \cdot m^2],$$

$$K(3,3) = [N \cdot m^2], K(3,4) = [N \cdot m^2], K(4,4) = [N \cdot m^2].$$

$$F_1^{(a)} = [N/m], M_1^{(a)} = [N \cdot m/m], M_2^{(a)} = [N \cdot m/m], M_3^{(a)} = [N \cdot m/m].$$

Gamma is the extensional actuation and Kappa1, Kappa2 and Kappa3 are the actuation rates in [deg/m].

Actuation oriented at 0°: Stiffness

• Elements 1-3:

$$K(1,1) = 9060847.09$$

$$K(1,2) = -1.32929933$$

$$K(1,3) = 0.0126881075$$

$$K(1,4) = -11322.1957$$

$$K(2,1) = -1.32929933$$

$$K(2,2) = 426.709675$$

$$K(2,3) = -9.78359929E-07$$

$$K(2,4) = -0.0731824933$$

$$K(3,1) = 0.0126881075$$

$$K(3,2) = -9.78359908E-07$$

$$K(3,3) = 721.948201$$

$$K(3,4) = -0.000787058162$$

$$K(4,1) = -11322.1957$$

$$K(4,2) = -0.0731824933$$

$$K(4,3) = -0.000787058163$$

$$K(4,4) = 24204.6879$$

• Element 4:

$$K(1,1) = 8534259.08$$

$$K(1,2) = -0.906606834$$

$$K(1,3) = -0.00510207086$$

$$K(1,4) = -9958.21154$$

$$K(2,1) = -0.906606834$$

$$K(2,2) = 347.947237$$

$$K(2,3) = 4.87494607E-07$$

$$K(2,4) = -0.036068645$$

$$K(3,1) = -0.00510207083$$

$$K(3,2) = 4.87494608E-07$$

$$K(3,3) = 584.969568$$

$$K(3,4) = 0.000254921793$$

$$K(4,1) = -9958.21154$$

$$K(4,2) = -0.036068645$$

$$K(4,3) = 0.000254921792$$

$$K(4,4) = 20092.373$$

• Element 5:

$$K(1,1) = 7960754.71$$

$$K(1,2) = -0.824759919$$

$$K(1,3) = -0.00315629108$$

$$K(1,4) = -8559.43057$$

$$K(2,1) = -0.824759919$$

$$K(2,2) = 277.598781$$

$$K(2,3) = 3.95341111E-07$$

$$K(2,4) = -0.0303092876$$

$$K(3,1) = -0.00315629117$$

$$K(3,2) = 3.95341117E-07$$

$$K(3,3) = 465.517193$$

K(3 4) = 0.000198984015
K(4 1) = -8559.43057
K(4 2) = -0.0303092876
K(4 3) = 0.000198984015
K(4 4) = 16287.585

• Element 6:

K(1 1) = 7360346.42
K(1 2) = -0.599442086
K(1 3) = -2.98218133
K(1 4) = -7216.92526
K(2 1) = -0.599442086
K(2 2) = 216.845776
K(2 3) = 0.0002189648
K(2 4) = -0.0148259802
K(3 1) = -2.98218133
K(3 2) = 0.0002189648
K(3 3) = 363.047034
K(3 4) = 0.176736231
K(4 1) = -7216.92526
K(4 2) = -0.0148259802
K(4 3) = 0.176736231
K(4 4) = 12907.6178

• Element 7:

K(1 1) = 6873409.43
K(1 2) = -0.481217923
K(1 3) = -0.00874607484
K(1 4) = -6461.41176
K(2 1) = -0.481217923
K(2 2) = 166.637628
K(2 3) = 9.29233468E-07
K(2 4) = -0.00992354013
K(3 1) = -0.00874607483
K(3 2) = 9.29233463E-07
K(3 3) = 279.053321
K(3 4) = 0.000450164674
K(4 1) = -6461.41176
K(4 2) = -0.00992354013
K(4 3) = 0.000450164673
K(4 4) = 9981.94962

• Element 8:

K(1 1) = 6233787.34
K(1 2) = -0.364847041
K(1 3) = 0.000358744914
K(1 4) = -5244.17272
K(2 1) = -0.364847041
K(2 2) = 123.595793
K(2 3) = 2.47754845E-06
K(2 4) = -0.00482374387
K(3 1) = 0.000358744906
K(3 2) = 2.47754845E-06
K(3 3) = 206.760384
K(3 4) = 0.000354887574
K(4 1) = -5244.17272
K(4 2) = -0.00482374387
K(4 3) = 0.000354887574
K(4 4) = 7505.31611

• Element 9:

K(1 1) = 5590756.42
K(1 2) = -0.282134877
K(1 3) = 0.00591295996
K(1 4) = -4166.26383
K(2 1) = -0.282134877
K(2 2) = 88.5393303
K(2 3) = 2.30946825E-06
K(2 4) = -0.00189367069
K(3 1) = 0.00591295994
K(3 2) = 2.30946825E-06
K(3 3) = 148.148889
K(3 4) = 7.76585528E-05
K(4 1) = -4166.26383
K(4 2) = -0.00189367069
K(4 3) = 7.76585527E-05
K(4 4) = 5464.0786

• Element 10:

K(1 1) = 4948403.4
K(1 2) = -0.169653704
K(1 3) = 0.00629680026
K(1 4) = -3271.6001
K(2 1) = -0.169653704
K(2 2) = 60.8834341
K(2 3) = -4.41627393E-07

$$\begin{aligned}K(2\ 4) &= 0.00170007942 \\K(3\ 1) &= 0.00629680025 \\K(3\ 2) &= -4.41627391E-07 \\K(3\ 3) &= 101.834126 \\K(3\ 4) &= -0.000259926206\end{aligned}$$

$$\begin{aligned}K(4\ 1) &= -3271.6001 \\K(4\ 2) &= 0.00170007942 \\K(4\ 3) &= -0.000259926206 \\K(4\ 4) &= 3826.79666\end{aligned}$$

Actuation oriented at 0°: Bending actuation constants

• Elements 1-3:

$$\begin{aligned}F_1^{(a)} &= 3.15696774 \\M_1^{(a)} &= 5.49593972E-05 \\M_2^{(a)} &= -2.56980014E-07 \\M_3^{(a)} &= -0.108725298\end{aligned}$$

$$\begin{aligned}\text{Gamma} &: 3.43006146E-07 \\Kappa1 &: 7.3982482E-06 \text{ [deg/m]} \\Kappa2 &: -2.10105772E-08 \text{ [deg/m]} \\Kappa3 &: -0.00024817455 \text{ [deg/m]}\end{aligned}$$

• Element 4:

$$\begin{aligned}F_1^{(a)} &= 2.79998265 \\M_1^{(a)} &= 0.000104353862 \\M_2^{(a)} &= -1.48370027E-06 \\M_3^{(a)} &= -0.07113824\end{aligned}$$

$$\begin{aligned}\text{Gamma} &: 3.24143558E-07 \\Kappa1 &: 1.72120604E-05 \text{ [deg/m]} \\Kappa2 &: -1.4507704E-07 \text{ [deg/m]} \\Kappa3 &: -0.000193654378 \text{ [deg/m]}\end{aligned}$$

• Element 5:

$$\begin{aligned}F_1^{(a)} &= 2.4011032 \\M_1^{(a)} &= 6.30087558E-05 \\M_2^{(a)} &= -1.90280293E-06 \\M_3^{(a)} &= -0.0383329423\end{aligned}$$

$$\begin{aligned}\text{Gamma} &: 2.9925615E-07 \\Kappa1 &: 1.30420724E-05 \text{ [deg/m]} \\Kappa2 &: -2.34026652E-07 \text{ [deg/m]} \\Kappa3 &: -0.000125835385 \text{ [deg/m]}\end{aligned}$$

• Element 6:

$$\begin{aligned}F_1^{(a)} &= 2.11292691 \\M_1^{(a)} &= 5.75070279E-05\end{aligned}$$

$$\begin{aligned}M_2^{(a)} &= 9.21814255E-05 \\M_3^{(a)} &= -0.0166796458\end{aligned}$$

$$\begin{aligned}\text{Gamma} &: 2.85958789E-07 \\Kappa1 &: 1.52355582E-05 \text{ [deg/m]} \\Kappa2 &: 1.47141562E-05 \text{ [deg/m]} \\Kappa3 &: -6.48788926E-05 \text{ [deg/m]}\end{aligned}$$

• Element 7:

$$\begin{aligned}F_1^{(a)} &= 1.88638282 \\M_1^{(a)} &= 8.7172875E-05 \\M_2^{(a)} &= -2.58933417E-07 \\M_3^{(a)} &= -0.000291825878\end{aligned}$$

$$\begin{aligned}\text{Gamma} &: 2.74586093E-07 \\Kappa1 &: 3.00189901E-05 \text{ [deg/m]} \\Kappa2 &: -5.26854587E-08 \text{ [deg/m]} \\Kappa3 &: 8.50884621E-06 \text{ [deg/m]}\end{aligned}$$

• Element 8:

$$\begin{aligned}F_1^{(a)} &= 1.6767818 \\M_1^{(a)} &= 5.37834832E-05 \\M_2^{(a)} &= -1.12828241E-07 \\M_3^{(a)} &= 0.00939968966\end{aligned}$$

$$\begin{aligned}\text{Gamma} &: 2.70195269E-07 \\Kappa1 &: 2.49815402E-05 \text{ [deg/m]} \\Kappa2 &: -3.14349516E-08 \text{ [deg/m]} \\Kappa3 &: 8.25745352E-05 \text{ [deg/m]}\end{aligned}$$

• Element 9:

$$\begin{aligned}F_1^{(a)} &= 1.51243733 \\M_1^{(a)} &= 2.37547805E-05 \\M_2^{(a)} &= 8.21978149E-07 \\M_3^{(a)} &= 0.0140846442\end{aligned}$$

$$\text{Gamma} : 2.72600442E-07$$

Kappa1: 1.54254339E-05 [deg/m]
Kappa2: 3.17188321E-07 [deg/m]
Kappa3: 0.00015959928 [deg/m]

$M_2^{(a)} = -5.49996052E-07$
 $M_3^{(a)} = 0.0174558563$

• Element 10:

$F_1^{(a)} = 1.3908675$
 $M_1^{(a)} = 6.29580348E-05$

Gamma : 2.84250482E-07
Kappa1: 5.92858296E-05 [deg/m]
Kappa2: -3.09753021E-07 [deg/m]
Kappa3: 0.000275277045 [deg/m]

Actuation oriented at $\pm 22^\circ$: Stiffness

• Elements 1-3:

K(1 1) = 7719454.31
K(1 2) = 338.674765
K(1 3) = 0.0164353273
K(1 4) = -7395.53281
K(2 1) = 338.674765
K(2 2) = 717.617859
K(2 3) = 0.000136233316
K(2 4) = 1.18130924
K(3 1) = 0.0164353273
K(3 2) = 0.000136233316
K(3 3) = 848.261579
K(3 4) = -0.000762272687
K(4 1) = -7395.53281
K(4 2) = 1.18130924
K(4 3) = -0.000762272685
K(4 4) = 20817.2736

K(4 2) = 1.10484767
K(4 3) = -0.00110085672
K(4 4) = 17348.9439

• Element 5:

K(1 1) = 6864886.92
K(1 2) = 300.557005
K(1 3) = -0.000471691614
K(1 4) = -5710.56759
K(2 1) = 300.557005
K(2 2) = 471.418624
K(2 3) = 9.67543833E-05
K(2 4) = 0.916573046
K(3 1) = -0.00047169159
K(3 2) = 9.67543833E-05
K(3 3) = 551.655393
K(3 4) = -0.000562611623
K(4 1) = -5710.56759
K(4 2) = 0.916573046
K(4 3) = -0.000562611623
K(4 4) = 14109.5255

• Element 4:

K(1 1) = 7319928.44
K(1 2) = 322.682757
K(1 3) = 0.000603093396
K(1 4) = -6530.60182
K(2 1) = 322.682757
K(2 2) = 587.775575
K(2 3) = 0.00014809963
K(2 4) = 1.10484767
K(3 1) = 0.00060309335
K(3 2) = 0.00014809963
K(3 3) = 690.439391
K(3 4) = -0.00110085671
K(4 1) = -6530.60182

• Element 6:

K(1 1) = 6378887.27
K(1 2) = 282.778998
K(1 3) = 0.0123446917
K(1 4) = -4864.44009
K(2 1) = 282.778998
K(2 2) = 369.868205
K(2 3) = 8.59679613E-05
K(2 4) = 0.721094431
K(3 1) = 0.0123446917
K(3 2) = 8.59679613E-05

$$\begin{aligned}K(3\ 3) &= 431.886319 \\K(3\ 4) &= -0.000518368257 \\K(4\ 1) &= -4864.44009 \\K(4\ 2) &= 0.721094431 \\K(4\ 3) &= -0.000518368259 \\K(4\ 4) &= 11208.0464\end{aligned}$$

• Element 7:

$$\begin{aligned}K(1\ 1) &= 5868079.2 \\K(1\ 2) &= 256.690743 \\K(1\ 3) &= -0.0068317651 \\K(1\ 4) &= -4135.81377 \\K(2\ 1) &= 256.690743 \\K(2\ 2) &= 283.305197 \\K(2\ 3) &= -1.20586977E-05 \\K(2\ 4) &= 0.666484441 \\K(3\ 1) &= -0.00683176511 \\K(3\ 2) &= -1.20586977E-05 \\K(3\ 3) &= 330.32518 \\K(3\ 4) &= 0.00050537407 \\K(4\ 1) &= -4135.81377 \\K(4\ 2) &= 0.666484441 \\K(4\ 3) &= 0.000505374069 \\K(4\ 4) &= 8672.41538\end{aligned}$$

• Element 8:

$$\begin{aligned}K(1\ 1) &= 5343951.9 \\K(1\ 2) &= 235.388447 \\K(1\ 3) &= 0.0021933679 \\K(1\ 4) &= -3409.56258 \\K(2\ 1) &= 235.388447 \\K(2\ 2) &= 210.918696 \\K(2\ 3) &= 5.85654121E-05 \\K(2\ 4) &= 0.380203387 \\K(3\ 1) &= 0.00219336791 \\K(3\ 2) &= 5.85654121E-05 \\K(3\ 3) &= 245.751117 \\K(3\ 4) &= -0.000545759771 \\K(4\ 1) &= -3409.56258\end{aligned}$$

$$\begin{aligned}K(4\ 2) &= 0.380203387 \\K(4\ 3) &= -0.000545759772 \\K(4\ 4) &= 6527.61918\end{aligned}$$

• Element 9:

$$\begin{aligned}K(1\ 1) &= 4809548.4 \\K(1\ 2) &= 211.285714 \\K(1\ 3) &= 0.0106257907 \\K(1\ 4) &= -2729.01238 \\K(2\ 1) &= 211.285714 \\K(2\ 2) &= 151.401151 \\K(2\ 3) &= 3.79138767E-05 \\K(2\ 4) &= 0.502425638 \\K(3\ 1) &= 0.0106257907 \\K(3\ 2) &= 3.79138767E-05 \\K(3\ 3) &= 176.841966 \\K(3\ 4) &= 0.000132329684 \\K(4\ 1) &= -2729.01238 \\K(4\ 2) &= 0.502425638 \\K(4\ 3) &= 0.000132329685 \\K(4\ 4) &= 4752.17543\end{aligned}$$

• Element 10:

$$\begin{aligned}K(1\ 1) &= 4270248.69 \\K(1\ 2) &= 185.959143 \\K(1\ 3) &= 0.00524953617 \\K(1\ 4) &= -2142.85387 \\K(2\ 1) &= 185.959143 \\K(2\ 2) &= 104.320464 \\K(2\ 3) &= 2.05239915E-05 \\K(2\ 4) &= 0.469139844 \\K(3\ 1) &= 0.00524953615 \\K(3\ 2) &= 2.05239915E-05 \\K(3\ 3) &= 122.127349 \\K(3\ 4) &= 0.000272097977 \\K(4\ 1) &= -2142.85387 \\K(4\ 2) &= 0.469139844 \\K(4\ 3) &= 0.000272097977 \\K(4\ 4) &= 3326.51488\end{aligned}$$

Actuation oriented at $\pm 22^\circ$: Bending actuation constants

• Elements 1-3:

$$F_1^{(a)} = 0.189091468$$

$$M_1^{(a)} = -0.171739569$$

$$M_2^{(a)} = 25.7298025$$

$$M_3^{(a)} = -0.0182542229$$

$$\text{Gamma} : 3.41169817\text{E-}08$$

$$\text{Kappa1} : -0.0137131401 \text{ [deg/m]}$$

$$\text{Kappa2} : 1.73791812 \text{ [deg/m]}$$

$$\text{Kappa3} : -4.87051901\text{E-}05 \text{ [deg/m]}$$

• Element 4:

$$F_1^{(a)} = 0.202235358$$

$$M_1^{(a)} = -0.141185052$$

$$M_2^{(a)} = 22.5542681$$

$$M_3^{(a)} = -0.0178889881$$

$$\text{Gamma} : 3.73234212\text{E-}08$$

$$\text{Kappa1} : -0.0137641172 \text{ [deg/m]}$$

$$\text{Kappa2} : 1.87165515 \text{ [deg/m]}$$

$$\text{Kappa3} : -5.72790119\text{E-}05 \text{ [deg/m]}$$

• Element 5:

$$F_1^{(a)} = 0.200548602$$

$$M_1^{(a)} = -0.115976797$$

$$M_2^{(a)} = 19.498046$$

$$M_3^{(a)} = -0.0162801277$$

$$\text{Gamma} : 3.90562592\text{E-}08$$

$$\text{Kappa1} : -0.0140974298 \text{ [deg/m]}$$

$$\text{Kappa2} : 2.02509722 \text{ [deg/m]}$$

$$\text{Kappa3} : -6.42079078\text{E-}05 \text{ [deg/m]}$$

• Element 6:

$$F_1^{(a)} = 0.188776156$$

$$M_1^{(a)} = -0.0911860232$$

$$M_2^{(a)} = 16.6053757$$

$$M_3^{(a)} = -0.0139001179$$

$$\text{Gamma} : 3.95309896\text{E-}08$$

$$\text{Kappa1} : -0.0141276123 \text{ [deg/m]}$$

$$\text{Kappa2} : 2.20293617 \text{ [deg/m]}$$

$$\text{Kappa3} : -6.90638736\text{E-}05 \text{ [deg/m]}$$

• Element 7:

$$F_1^{(a)} = 0.19102346$$

$$M_1^{(a)} = -0.0702856734$$

$$M_2^{(a)} = 13.911412$$

$$M_3^{(a)} = -0.0127033534$$

$$\text{Gamma} : 4.24494736\text{E-}08$$

$$\text{Kappa1} : -0.0142165176 \text{ [deg/m]}$$

$$\text{Kappa2} : 2.41297147 \text{ [deg/m]}$$

$$\text{Kappa3} : -8.18150284\text{E-}05 \text{ [deg/m]}$$

• Element 8:

$$F_1^{(a)} = 0.171631674$$

$$M_1^{(a)} = -0.0532338768$$

$$M_2^{(a)} = 11.4356253$$

$$M_3^{(a)} = -0.010342455$$

$$\text{Gamma} : 4.22326687\text{E-}08$$

$$\text{Kappa1} : -0.0144641929 \text{ [deg/m]}$$

$$\text{Kappa2} : 2.66616529 \text{ [deg/m]}$$

$$\text{Kappa3} : -8.8450982\text{E-}05 \text{ [deg/m]}$$

• Element 9:

$$F_1^{(a)} = 0.155686133$$

$$M_1^{(a)} = -0.0370525409$$

$$M_2^{(a)} = 9.19090471$$

$$M_3^{(a)} = -0.00839324869$$

$$\text{Gamma} : 4.20348341\text{E-}08$$

$$\text{Kappa1} : -0.0140258289 \text{ [deg/m]}$$

$$\text{Kappa2} : 2.97780039 \text{ [deg/m]}$$

$$\text{Kappa3} : -9.84122465\text{E-}05 \text{ [deg/m]}$$

• Element 10:

$$F_1^{(a)} = 0.178413225$$

$$M_1^{(a)} = -0.0252695621$$

$$M_2^{(a)} = 7.185599$$

$$M_3^{(a)} = -0.00862558993$$

$$\text{Gamma} : 5.09907383\text{E-}08$$

$$\text{Kappa1} : -0.0138839852 \text{ [deg/m]}$$

$$\text{Kappa2} : 3.37110826 \text{ [deg/m]}$$

$$\text{Kappa3} : -0.000145002568 \text{ [deg/m]}$$

Actuation oriented at $\pm 22^\circ$: Twist actuation constants

• Elements 1-3:

$$\begin{aligned}F_1^{(a)} &= 3.73739457 \\M_1^{(a)} &= 16.283186 \\M_2^{(a)} &= 1.23996215E-06 \\M_3^{(a)} &= 0.00153852882\end{aligned}$$

$$\begin{aligned}\text{Gamma} &: -8.71359348E-07 \\ \text{Kappa1} &: 1.75721849 \text{ [deg/m]} \\ \text{Kappa2} &: -1.49384357E-07 \text{ [deg/m]} \\ \text{Kappa3} &: -9.88874718E-05 \text{ [deg/m]}\end{aligned}$$

• Element 4:

$$\begin{aligned}F_1^{(a)} &= 3.30028406 \\M_1^{(a)} &= 14.3290405 \\M_2^{(a)} &= -2.02778599E-07 \\M_3^{(a)} &= 0.0229250257\end{aligned}$$

$$\begin{aligned}\text{Gamma} &: -1.00389837E-06 \\ \text{Kappa1} &: 1.89370713 \text{ [deg/m]} \\ \text{Kappa2} &: -1.26696696E-07 \text{ [deg/m]} \\ \text{Kappa3} &: -3.18014622E-05 \text{ [deg/m]}\end{aligned}$$

• Element 5:

$$\begin{aligned}F_1^{(a)} &= 2.92939659 \\M_1^{(a)} &= 12.4000835 \\M_2^{(a)} &= 7.02950753E-07 \\M_3^{(a)} &= 0.042580152\end{aligned}$$

$$\begin{aligned}\text{Gamma} &: -1.14702891E-06 \\ \text{Kappa1} &: 2.05184127 \text{ [deg/m]} \\ \text{Kappa2} &: -5.19250277E-08 \text{ [deg/m]} \\ \text{Kappa3} &: 3.30689796E-05 \text{ [deg/m]}\end{aligned}$$

• Element 6:

$$\begin{aligned}F_1^{(a)} &= 2.70827672 \\M_1^{(a)} &= 10.5665352 \\M_2^{(a)} &= -0.000374426064 \\M_3^{(a)} &= 0.0509004846\end{aligned}$$

$$\begin{aligned}\text{Gamma} &: -1.30519787E-06 \\ \text{Kappa1} &: 2.23429427 \text{ [deg/m]} \\ \text{Kappa2} &: -1.22622375E-05 \text{ [deg/m]} \\ \text{Kappa3} &: 0.000113211632 \text{ [deg/m]}\end{aligned}$$

• Element 7:

$$\begin{aligned}F_1^{(a)} &= 2.29850487 \\M_1^{(a)} &= 8.86542374 \\M_2^{(a)} &= -1.26617102E-06 \\M_3^{(a)} &= 0.0588559924\end{aligned}$$

$$\begin{aligned}\text{Gamma} &: -1.48312127E-06 \\ \text{Kappa1} &: 2.45402661 \text{ [deg/m]} \\ \text{Kappa2} &: -3.32071647E-07 \text{ [deg/m]} \\ \text{Kappa3} &: 0.000204754584 \text{ [deg/m]}\end{aligned}$$

• Element 8:

$$\begin{aligned}F_1^{(a)} &= 2.2043578 \\M_1^{(a)} &= 7.27957381 \\M_2^{(a)} &= -6.44271627E-06 \\M_3^{(a)} &= 0.0541912149\end{aligned}$$

$$\begin{aligned}\text{Gamma} &: -1.68336995E-06 \\ \text{Kappa1} &: 2.71626681 \text{ [deg/m]} \\ \text{Kappa2} &: -1.99998264E-06 \text{ [deg/m]} \\ \text{Kappa3} &: 0.000291900614 \text{ [deg/m]}\end{aligned}$$

• Element 9:

$$\begin{aligned}F_1^{(a)} &= 1.92499874 \\M_1^{(a)} &= 5.84797741 \\M_2^{(a)} &= -2.85491463E-06 \\M_3^{(a)} &= 0.0620162419\end{aligned}$$

$$\begin{aligned}\text{Gamma} &: -1.93871829E-06 \\ \text{Kappa1} &: 3.04552671 \text{ [deg/m]} \\ \text{Kappa2} &: -1.80522735E-06 \text{ [deg/m]} \\ \text{Kappa3} &: 0.000430028692 \text{ [deg/m]}\end{aligned}$$

• Element 10:

$$\begin{aligned}F_1^{(a)} &= 1.63045224 \\M_1^{(a)} &= 4.5766845 \\M_2^{(a)} &= 1.69499776E-06 \\M_3^{(a)} &= 0.0536100028\end{aligned}$$

$$\begin{aligned}\text{Gamma} &: -2.24069877E-06 \\ \text{Kappa1} &: 3.46385073 \text{ [deg/m]} \\ \text{Kappa2} &: 3.47455766E-07 \text{ [deg/m]} \\ \text{Kappa3} &: 0.000514141335 \text{ [deg/m]}\end{aligned}$$

Actuation oriented at $\pm 45^\circ$: Stiffness

• Elements 1-3:

K(1 1) = 5646151.72
K(1 2) = 204.137272
K(1 3) = 0.0157910716
K(1 4) = -267.883142
K(2 1) = 204.137272
K(2 2) = 854.389753
K(2 3) = -0.000210587573
K(2 4) = 3.02193601
K(3 1) = 0.0157910716
K(3 2) = -0.000210587571
K(3 3) = 615.817763
K(3 4) = -7.20740632E-05
K(4 1) = -267.883142
K(4 2) = 3.02193601
K(4 3) = -7.20740588E-05
K(4 4) = 15440.8911

• Element 4:

K(1 1) = 5353002.67
K(1 2) = 192.863574
K(1 3) = 0.00160694481
K(1 4) = -216.440373
K(2 1) = 192.863574
K(2 2) = 699.573685
K(2 3) = 9.90850646E-05
K(2 4) = 2.5046933
K(3 1) = 0.00160694488
K(3 2) = 9.90850645E-05
K(3 3) = 501.394326
K(3 4) = -0.000749793439
K(4 1) = -216.440373
K(4 2) = 2.5046933
K(4 3) = -0.000749793436
K(4 4) = 12865.5541

• Element 5:

K(1 1) = 5018200.26
K(1 2) = 177.888648

K(1 3) = 0.000872380181
K(1 4) = -170.108251
K(2 1) = 177.888648
K(2 2) = 561.038306
K(2 3) = 5.24756304E-05
K(2 4) = 1.9558965
K(3 1) = 0.00087238019
K(3 2) = 5.24756302E-05
K(3 3) = 400.706755
K(3 4) = -0.000311181993
K(4 1) = -170.108251
K(4 2) = 1.9558965
K(4 3) = -0.000311181995
K(4 4) = 10459.3993

• Element 6:

K(1 1) = 4662498.97
K(1 2) = 165.606959
K(1 3) = 0.0139759738
K(1 4) = -150.770305
K(2 1) = 165.606959
K(2 2) = 440.02237
K(2 3) = -0.000171361322
K(2 4) = 1.52896524
K(3 1) = 0.0139759738
K(3 2) = -0.000171361322
K(3 3) = 313.815134
K(3 4) = -5.51043203E-05
K(4 1) = -150.770305
K(4 2) = 1.52896524
K(4 3) = -5.51043229E-05
K(4 4) = 8309.34095

• Element 7:

K(1 1) = 4288654.94
K(1 2) = 148.556117
K(1 3) = -0.00352413007
K(1 4) = -136.954495
K(2 1) = 148.556117
K(2 2) = 337.036381

$K(2\ 3) = -2.44972636E-05$
 $K(2\ 4) = 1.20847588$
 $K(3\ 1) = -0.00352413003$
 $K(3\ 2) = -2.44972637E-05$
 $K(3\ 3) = 240.124895$
 $K(3\ 4) = 0.000443661668$
 $K(4\ 1) = -136.954495$
 $K(4\ 2) = 1.20847588$
 $K(4\ 3) = 0.000443661667$
 $K(4\ 4) = 6428.77729$

• Element 8:

$K(1\ 1) = 3905268.12$
 $K(1\ 2) = 134.897853$
 $K(1\ 3) = 0.00073746597$
 $K(1\ 4) = -114.782616$
 $K(2\ 1) = 134.897853$
 $K(2\ 2) = 250.852085$
 $K(2\ 3) = 6.93433321E-05$
 $K(2\ 4) = 0.84382027$
 $K(3\ 1) = 0.000737465928$
 $K(3\ 2) = 6.93433322E-05$
 $K(3\ 3) = 178.732335$
 $K(3\ 4) = -0.000463986794$
 $K(4\ 1) = -114.782616$
 $K(4\ 2) = 0.84382027$
 $K(4\ 3) = -0.000463986795$
 $K(4\ 4) = 4838.76601$

• Element 9:

$K(1\ 1) = 3514212.01$
 $K(1\ 2) = 119.607256$

$K(1\ 3) = 0.0139734437$
 $K(1\ 4) = -85.8681822$
 $K(2\ 1) = 119.607256$
 $K(2\ 2) = 179.940132$
 $K(2\ 3) = -0.000156418231$
 $K(2\ 4) = 0.730680625$
 $K(3\ 1) = 0.0139734437$
 $K(3\ 2) = -0.000156418231$
 $K(3\ 3) = 128.693954$
 $K(3\ 4) = 0.000439325119$
 $K(4\ 1) = -85.8681822$
 $K(4\ 2) = 0.730680625$
 $K(4\ 3) = 0.000439325119$
 $K(4\ 4) = 3521.97257$

• Element 10:

$K(1\ 1) = 3119449.89$
 $K(1\ 2) = 104.649162$
 $K(1\ 3) = 0.0095805776$
 $K(1\ 4) = -47.6575911$
 $K(2\ 1) = 104.649162$
 $K(2\ 2) = 123.918996$
 $K(2\ 3) = -0.00012074851$
 $K(2\ 4) = 0.544808546$
 $K(3\ 1) = 0.00958057758$
 $K(3\ 2) = -0.00012074851$
 $K(3\ 3) = 88.946838$
 $K(3\ 4) = 0.000479439834$
 $K(4\ 1) = -47.6575911$
 $K(4\ 2) = 0.544808546$
 $K(4\ 3) = 0.000479439834$
 $K(4\ 4) = 2464.20586$

Actuation oriented at $\pm 45^\circ$: Bending actuation constants

• Elements 1-3:

$F_1^{(a)} = 0.321245753$
 $M_1^{(a)} = -0.247796017$
 $M_2^{(a)} = 9.21606499$
 $M_3^{(a)} = -0.0367222011$

Gamma : 6.72305752E-08
Kappa1: -0.0166175573 [deg/m]

Kappa2: 0.857464142 [deg/m]
Kappa3: -0.000132940277 [deg/m]

• Element 4:

$F_1^{(a)} = 0.319173726$
 $M_1^{(a)} = -0.203748205$
 $M_2^{(a)} = 8.0799537$
 $M_3^{(a)} = -0.0329650979$

Gamma : 7.00128937E-08
Kappa1: -0.0166879043 [deg/m]
Kappa2: 0.923319721 [deg/m]
Kappa3: -0.000143437464 [deg/m]

• Element 5:

$F_1^{(a)} = 0.356958049$
 $M_1^{(a)} = -0.166797357$
 $M_2^{(a)} = 6.98730628$
 $M_3^{(a)} = -0.032851206$

Gamma : 8.1564663E-08
Kappa1: -0.0170350636 [deg/m]
Kappa2: 0.999092667 [deg/m]
Kappa3: -0.000176665103 [deg/m]

• Element 6:

$F_1^{(a)} = 0.278163299$
 $M_1^{(a)} = -0.131519715$
 $M_2^{(a)} = 5.95264278$
 $M_3^{(a)} = -0.0233828528$

Gamma : 7.01303717E-08
Kappa1: -0.0171258624 [deg/m]
Kappa2: 1.08682241 [deg/m]
Kappa3: -0.000158001494 [deg/m]

• Element 7:

$F_1^{(a)} = 0.261816026$
 $M_1^{(a)} = -0.10108013$
 $M_2^{(a)} = 4.98967239$
 $M_3^{(a)} = -0.0199002184$

Gamma : 7.13578376E-08
Kappa1: -0.0171845927 [deg/m]

Actuation oriented at $\pm 45^\circ$: Twist actuation constants

• Elements 1-3:

$F_1^{(a)} = 5.07837124$
 $M_1^{(a)} = 25.6498103$
 $M_2^{(a)} = -2.58551417E-05$
 $M_3^{(a)} = 0.150889006$

Kappa2: 1.19057702 [deg/m]
Kappa3: -0.000174123264 [deg/m]

• Element 8:

$F_1^{(a)} = 0.212308743$
 $M_1^{(a)} = -0.0764822442$
 $M_2^{(a)} = 4.10373914$
 $M_3^{(a)} = -0.0146670509$

Gamma : 6.48056934E-08
Kappa1: -0.0174706873 [deg/m]
Kappa2: 1.3155255 [deg/m]
Kappa3: -0.000170411516 [deg/m]

• Element 9:

$F_1^{(a)} = 0.170937429$
 $M_1^{(a)} = -0.053104912$
 $M_2^{(a)} = 3.30055217$
 $M_3^{(a)} = -0.0102769742$

Gamma : 5.8514781E-08
Kappa1: -0.0169097295 [deg/m]
Kappa2: 1.46943745 [deg/m]
Kappa3: -0.000163780191 [deg/m]

• Element 10:

$F_1^{(a)} = 0.199636408$
 $M_1^{(a)} = -0.0357362982$
 $M_2^{(a)} = 2.58268629$
 $M_3^{(a)} = -0.0104468768$

Gamma : 7.35193128E-08
Kappa1: -0.0165240898 [deg/m]
Kappa2: 1.663657 [deg/m]
Kappa3: -0.000239491512 [deg/m]

Gamma : -1.85797174E-07
Kappa1: 1.72009021 [deg/m]
Kappa2: -1.81705829E-06 [deg/m]
Kappa3: 0.000223073223 [deg/m]

• Element 4:

$F_1^{(a)} = 4.86539844$

$$M_1^{(a)} = 22.6277814$$

$$M_2^{(a)} = 4.04777526E-06$$

$$M_3^{(a)} = 0.134793043$$

$$\text{Gamma} : -2.56286116E-07$$

$$\text{Kappa1} : 1.85324105 \text{ [deg/m]}$$

$$\text{Kappa2} : 9.67201347E-08 \text{ [deg/m]}$$

$$\text{Kappa3} : 0.000239250807 \text{ [deg/m]}$$

• Element 5:

$$F_1^{(a)} = 4.65212346$$

$$M_1^{(a)} = 19.6544122$$

$$M_2^{(a)} = 1.97953401E-06$$

$$M_3^{(a)} = 0.102240789$$

$$\text{Gamma} : -3.14689982E-07$$

$$\text{Kappa1} : 2.007203 \text{ [deg/m]}$$

$$\text{Kappa2} : 2.03710758E-08 \text{ [deg/m]}$$

$$\text{Kappa3} : 0.000184429093 \text{ [deg/m]}$$

• Element 6:

$$F_1^{(a)} = 4.24640585$$

$$M_1^{(a)} = 16.7791689$$

$$M_2^{(a)} = -2.48216274E-05$$

$$M_3^{(a)} = 0.1030697$$

$$\text{Gamma} : -4.43500572E-07$$

$$\text{Kappa1} : 2.18484197 \text{ [deg/m]}$$

$$\text{Kappa2} : -3.33764982E-06 \text{ [deg/m]}$$

$$\text{Kappa3} : 0.000308217042 \text{ [deg/m]}$$

• Element 7:

$$F_1^{(a)} = 3.8098284$$

$$M_1^{(a)} = 14.1103179$$

$$M_2^{(a)} = -2.34915086E-06$$

$$M_3^{(a)} = 0.0893576578$$

$$\text{Gamma} : -5.61670417E-07$$

$$\text{Kappa1} : 2.39875014 \text{ [deg/m]}$$

$$\text{Kappa2} : -3.16918421E-07 \text{ [deg/m]}$$

$$\text{Kappa3} : 0.000344789953 \text{ [deg/m]}$$

• Element 8:

$$F_1^{(a)} = 3.49577947$$

$$M_1^{(a)} = 11.6167853$$

$$M_2^{(a)} = 7.23001739E-06$$

$$M_3^{(a)} = 0.0784084307$$

$$\text{Gamma} : -7.04269822E-07$$

$$\text{Kappa1} : 2.6533479 \text{ [deg/m]}$$

$$\text{Kappa2} : 1.28965427E-06 \text{ [deg/m]}$$

$$\text{Kappa3} : 0.000464765594 \text{ [deg/m]}$$

• Element 9:

$$F_1^{(a)} = 3.05472204$$

$$M_1^{(a)} = 9.33728535$$

$$M_2^{(a)} = -2.89908268E-05$$

$$M_3^{(a)} = 0.075400204$$

$$\text{Gamma} : -8.96639171E-07$$

$$\text{Kappa1} : 2.97317092 \text{ [deg/m]}$$

$$\text{Kappa2} : -9.28981826E-06 \text{ [deg/m]}$$

$$\text{Kappa3} : 0.000608540778 \text{ [deg/m]}$$

• Element 10:

$$F_1^{(a)} = 2.93883349$$

$$M_1^{(a)} = 7.30545454$$

$$M_2^{(a)} = -2.44034773E-05$$

$$M_3^{(a)} = 0.0525800218$$

$$\text{Gamma} : -1.03553209E-06$$

$$\text{Kappa1} : 3.37783307 \text{ [deg/m]}$$

$$\text{Kappa2} : -1.1130324E-05 \text{ [deg/m]}$$

$$\text{Kappa3} : 0.000474600592 \text{ [deg/m]}$$

Appendix B

An Approximation for the Structural Modes

Section 3.4.2 expressed the need for an approximation to the structural modes, which is now detailed in this Appendix. The bending stiffness and torsion stiffness ($EI(s)$ and $GJ(s)$ respectively) will be obtained by fitting a spline along the bending and torsion stiffness of each individual element, and will be entered in the lumped parameter formulation of a beam undergoing bending along its longitudinal axis:

$$[M]\{\ddot{u}_3\} + [K]\{u_3\} = \{F_{external}\} \quad (B.2)$$

where u_3 is the transversal deflection, M is the mass matrix, K the stiffness matrix, and $F_{external}$ the external forces on the beam. Eq. (B.2) is turned then into an eigenvalue problem:

$$\{u_3\} = \lambda^2 [C][M]\{u_3\} \quad (B.3)$$

which effectively has the form $A \cdot x = \lambda \cdot x$. C is the flexibility matrix, i.e $[C] = [K]^{-1}$. The flexibility influence coefficients C_{ij} are found next.

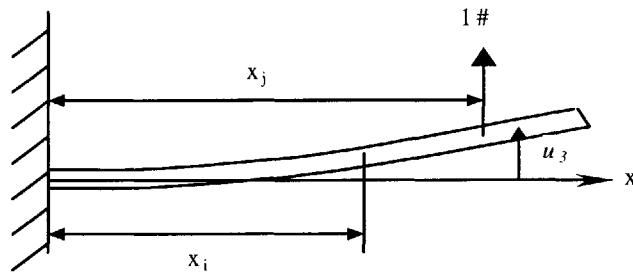


Figure B.1 Unit force applied on a cantilever beam (u_3 measures the deflection)

Figure B.1 shows a unit force acting on a cantilever beam. It holds that

$$EI \frac{d^2 u_3}{dx^2} = M(x) = 1 \cdot (x_j - x) \quad (\text{B.4})$$

Isolating u_3 from Eq. (B.4) yields the values of C_{ij} , since $C_{ij} = u_3(x_i)$ for a unit force acting at x_j . After integrating Eq. (B.4) twice, one obtains

$$C_{ij} = \begin{cases} \int_0^{x_i} \left[\int_0^{\xi} \frac{x_j - s}{EI(s)} ds \right] \cdot d\xi & x_j \geq x_i \\ u'_3(x_j) \cdot (x_i - x_j) + u_3(x_j) & x_j < x_i \end{cases} \quad (\text{B.5})$$

where

$$u'_3(x_j) = \int_0^{x_j} \frac{x_j - s}{EI(s)} ds$$

$$u_3(x_j) = \int_0^{x_i} \left[\int_0^{\xi} \frac{x_j - s}{EI(s)} ds \right] \cdot d\xi$$

Working similarly for the torsion case in a cantilever beam yields

$$C_{ij} = \begin{cases} \int_0^{x_i} \frac{ds}{GJ(s)} & x_j \geq x_i \\ \int_0^{x_j} \frac{ds}{GJ(s)} & x_j < x_i \end{cases} \quad (\text{B.6})$$

All there is left to do is to fit a curve along the bending and the torsion stiffness of the beam ($EI(s)$ and $GJ(s)$ respectively):

$$EI(x) = \begin{cases} EI_1 = EI_0 \cdot 2^{e_1} & x \leq 0.5m \\ EI_0 \left(\frac{3.5 - x}{1.5} \right)^{e_1} & x > 0.5m \end{cases} \quad (\text{B.7})$$

$$GJ(x) = \begin{cases} GJ_1 = GJ_0 \cdot 2^{e_2} & x \leq 0.5m \\ GJ_0 \left(\frac{3.5 - x}{1.5} \right)^{e_2} & x > 0.5m \end{cases} \quad (\text{B.8})$$

where $EI_0 = 60 \text{ kg}\cdot\text{m}^2$, $GJ_0 = 78 \text{ kg}\cdot\text{m}^2$, $e_1 = 3.1$ and $e_2 = 3$. The equations that describe the influence coefficients for the bending case are the following:

$$C_{ij} = \begin{cases} \int_0^{x_i} \left[\int_0^{\xi} \frac{x_j - s}{EI(s)} ds \right] \cdot d\xi & x_j \geq x_i \\ u'_3(x_j) \cdot (x_i - x_j) + u_3(x_j) & x_j < x_i \end{cases} \quad (\text{B.9})$$

where

$$u'_3(x_j) = \int_0^{x_j} \frac{x_j - s}{EI(s)} ds$$

$$u_3(x_j) = \int_0^{x_i} \left[\int_0^{\xi} \frac{x_j - s}{EI(s)} ds \right] \cdot d\xi$$

The following step is to compute the integral $\int_0^{\xi} \frac{x_j - s}{EI(s)} ds$.

For $\xi \leq 0.5m$,

$$\int_0^{\xi} \frac{x_j - s}{EI(s)} ds = \frac{1}{EI_1} \left[x_j s - \frac{s^2}{2} \right]_0^{\xi} = \frac{1}{EI_1} \left(x_j \xi - \frac{\xi^2}{2} \right) \quad (\text{B.10})$$

For $\xi > 0.5m$,

$$\int_0^{\xi} \frac{x_j - s}{EI(s)} ds = \int_0^{0.5} \frac{x_j - s}{EI_1} ds + \int_{0.5}^{\xi} \frac{x_j - s}{EI(s)} ds = \frac{1}{E_1} (0.5x_j - 0.125) -$$

$$- \frac{1.5}{EI_0} \left\{ \left(\frac{x_j - \xi}{1 - e_1} \right) \left(\frac{3.5 - \xi}{1.5} \right)^{1 - e_1} - 2^{1 - e_1} \left(\frac{x_j - 0.5}{1 - e_1} \right) - 1.5 \left(\frac{1}{1 - e_1} \right) \left(\frac{1}{2 - e_1} \right) \left[\left(\frac{3.5 - \xi}{1.5} \right)^{2 - e_1} - 2^{1 - e_1} \right] \right\} \quad (\text{B.11})$$

The equation for the torsion mode flexibility influence coefficients is

$$C_{ij} = \begin{cases} \int_0^{x_i} \frac{ds}{GJ(s)} & x_j \geq x_i \\ \int_0^{x_j} \frac{ds}{GJ(s)} & x_j < x_i \end{cases} \quad (\text{B.12})$$

Substituting Eq. (B.8) into Eq. (B.12) after calculations yields

$$C_{ij} = \begin{cases} \left[\left(\frac{-1.5}{GJ_0} \right) \left(\frac{1}{1 - e_2} \right) \left[\left(\frac{3.5 - x_i}{1.5} \right)^{1 - e_2} - \left(\frac{3.5}{1.5} \right)^{1 - e_2} \right] \right] & x_j \geq x_i \\ \left[\left(\frac{-1.5}{GJ_0} \right) \left(\frac{1}{1 - e_2} \right) \left[\left(\frac{3.5 - x_j}{1.5} \right)^{1 - e_2} - \left(\frac{3.5}{1.5} \right)^{1 - e_2} \right] \right] & x_j < x_i \end{cases} \quad (\text{B.13})$$

Appendix C

Simulation

One of the advantages of the digital computer is that it allows models to “become alive.” One is not restricted to look at a data printout but can actually watch the motion of the system, which gives the aeroelastician much insight into the design. Both the two-dimensional and the three-dimensional simulations that are presented in this chapter accomplish this. The three-dimensional simulation provides a more realistic representation of the wing behavior, while the two-dimensional simulation provides much more flexibility and information.

Formulation

Displacements and Rotations

The key concept in the simulation is to precisely know the displacements and rotations of any element with time. The procedure to obtain both was detailed in Section 3.3, which resulted in

$$u_n = [T_{u\theta} \quad 0 \quad 0] \begin{Bmatrix} \theta \\ \dot{\theta} \\ \lambda \end{Bmatrix} \quad (C.1)$$

$$\theta = [I \quad 0 \quad 0] \begin{Bmatrix} \theta \\ \dot{\theta} \\ \lambda \end{Bmatrix} \quad (C.2)$$

where u_n is the displacement vector, and θ the rotation vector expressed as Rodrigues parameters. These are a non-singular, minimal coordinate representation of a rigid body orientation. The Rodrigues parameters can be defined through a transformation from the Euler parameters:

$$\theta_i = \frac{\beta_i}{1 + \beta_0} \quad (\text{C.3})$$

with $i=1,2,3$, or in terms of the principal rotating axis \hat{e} and the principal rotating angle ϕ as

$$\theta = \hat{e} \cdot \tan \frac{\phi}{4} \quad (\text{C.4})$$

In order to implement the simulation in the three-dimensional space, the cosine rotation matrix must be expressed in terms of the Rodrigues parameters [59]:

$$C(\theta) = \frac{1}{\Delta^2} \begin{bmatrix} 4(\theta_1^2 - \theta_2^2 - \theta_3^2) + \Sigma^2 & 8\theta_1\theta_2 + 4\theta_3\Sigma & 8\theta_1\theta_3 - 4\theta_2\Sigma \\ 8\theta_1\theta_2 - 4\theta_3\Sigma & 4(-\theta_1^2 + \theta_2^2 - \theta_3^2) + \Sigma^2 & 8\theta_2\theta_3 + 4\theta_1\Sigma \\ 8\theta_1\theta_3 + 4\theta_2\Sigma & 8\theta_2\theta_3 + 4\theta_1\Sigma & 4(-\theta_1^2 - \theta_2^2 + \theta_3^2) + \Sigma^2 \end{bmatrix} \quad (\text{C.5})$$

where $\Delta = 1 + \theta^T \theta$ and $\Sigma = 1 - \theta^T \theta$.

Once the rotation matrix is known, any element can be correctly placed in space as shown in Figure C.1.

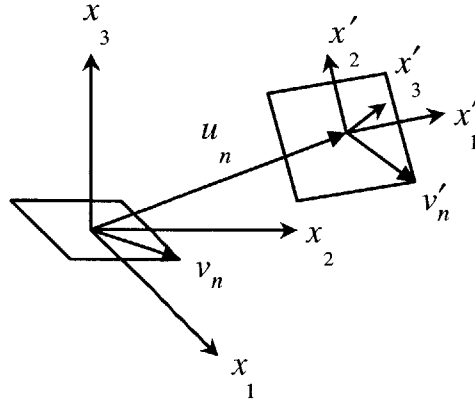


Figure C.1 Element Rotation in Space

Any vector can be transformed as

$$v'_n = d + C(\theta) \cdot v_n + u_n \quad (\text{C.6})$$

where d is the distance from the center of the element to the reference axes and u_n is the displacement vector for the element center point.

Normalized Output

In Section 3.7.1 it was already shown how to obtain the normalized inputs u as outputs by defining

$$\bar{C} = [0 \quad -C_k] \quad (C.7)$$

This is enough to plot the normalized voltage response to a given gust disturbance with respect to time:

$$u = [0 \quad -C_k] \cdot \begin{Bmatrix} \dot{\hat{x}} \\ \hat{x} \end{Bmatrix} + D \cdot \begin{Bmatrix} w \\ u_{ref} \end{Bmatrix} \quad (C.8)$$

Implementation

In the present work, two simulations have been implemented: a two-dimensional simulation (where the motion of selected elements of the wing is plotted) and a more realistic three-dimensional one (where the whole wing oscillates, even though not in real time).

Two-Dimensional Simulation

The 2-D simulation has been designed almost as a “virtual oscilloscope.” The input is the disturbance due to gust and several outputs are available as functions of time. The 2-D simulation has been coded as a Matlab script and, as the regulator implementation, is able to handle discretizations of any number of elements.

Data Requirements

The input to the simulation is a gust disturbance with respect to time. Any function explicitly described with respect to time is straightforward to implement. The following models are already built in:

- 1-Cosine gust model (see Section 3.5).
- Sinusoidal
- Step
- Pulse
- Ramp and plateau

Graphical Output

The Matlab implementation produces graphical outputs such as the one shown in Figure C.2 and Figure C.3.

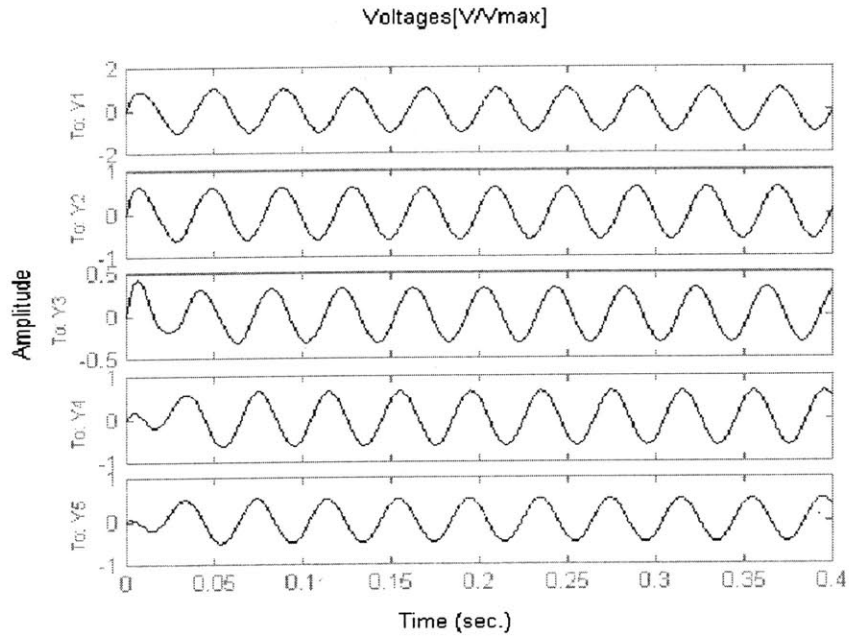


Figure C.2 Normalized voltages with respect to time for a wing divided into 5 active regions

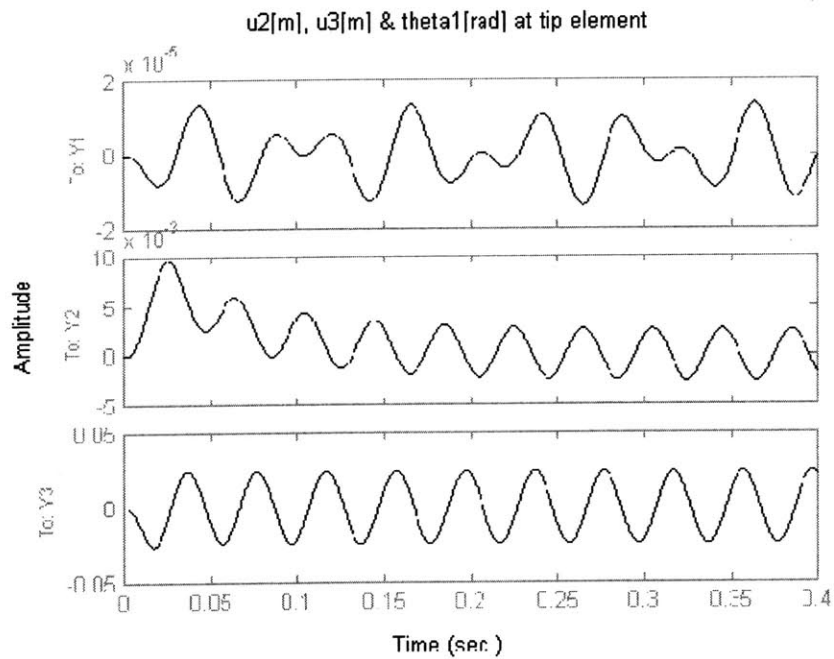


Figure C.3 Two displacements and a rotation at the tip after a disturbance: (i) chordwise tip deflection (u_2), (ii) flatwise tip deflection (u_3), (iii) tip twist (θ_1).

Three-Dimensional Simulation

The 3-D simulation may not provide as much numerical data as the 2-D one, but it certainly provides greater insight on how the wing behaves under some disturbance. The graphical simulation handles wings discretized in any number of elements. It has been implemented in Simulink using Matlab scripts for the different element position and rotation calculations. Unfortunately, the motion is not fast enough to simulate a highly flexible wing oscillating in real time on a desktop computer. A movie generation algorithm was implemented in the simulation code to overcome this problem.

As the simulation marches, every new picture drawn on the screen is saved as a frame at some Δt determined by Simulink's numerical integrator. After the total simulation time, a Matlab script generates the whole animation in the right time sequence and at a reasonable pace.

Figure C.4 shows one frame in a simulation of a 5-element wing hit by a sinusoidal disturbance.

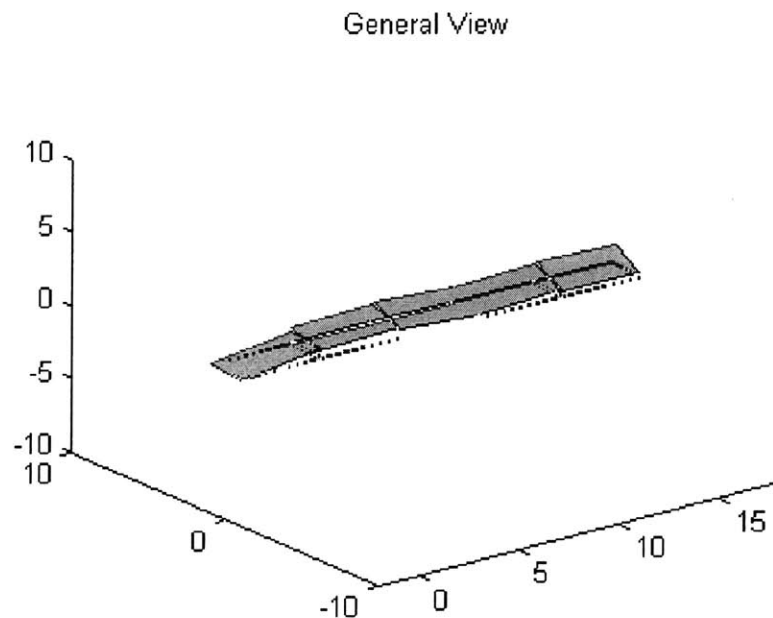


Figure C.4 One frame in a 3-D simulation of a 5-element wing hit by a sinusoidal disturbance

Appendix D

The Tcl/Tk Computer-Based Framework

The present formulation consists of different building blocks, each one implemented in a convenient computer language or script. Thus, the nonlinear aeroelastic model is coded in C++ with some Fortran 77 routines, VABS-A is programmed in Fortran 77, and the aeroelastic control design is implemented as Matlab scripts. The need for a computer infrastructure to integrate all the different elements under a common interface to facilitate the design was clear. This appendix concentrates on the software that accomplishes that integration. The code is named “Aeroelastic Modeling”, its current version is 1.1, it is programmed in Tcl/Tk and runs on a Pentium II computer under the Linux operating system.

Tcl and Tk were developed by John Ousterhout (Ref. [55]). Tcl stands for “tool command language,” and is both a language and a library. It is a simple textual language, intended primarily for issuing commands to interactive programs such as text editors, debuggers, illustrators, and shells; it can also be used as a library package embedded in application programs. Tk is an extension to Tcl which provides an interface to the X-Windows environment. Everything that follows is coded in Tcl/Tk. For more details on the language itself, please refer to Ousterhout’s excellent book (Ref. [55]).

The Tree Directory Structure

Everything in the program is relative to the `main` program installation directory. All the different aeroelastic options available have their own directory. Even though it is not essential for the user to know the exact tree structure (except for the *input* directory), it gives a good overview of what the program does and how it handles the data. The different directories are the following:

- *input* holds all new files that the user wants to input to the system,
- *data* contains the project names,
- *aerosolv* contains the aeroelastic solver information,
- *flightcond* contains the information relative to the flight conditions,
- *meshgen* contains everything relative to the mesh generator,
- *vabs* holds everything related to the beam cross-sectional model, and
- *wingplan* contains the wing planform dimensions.

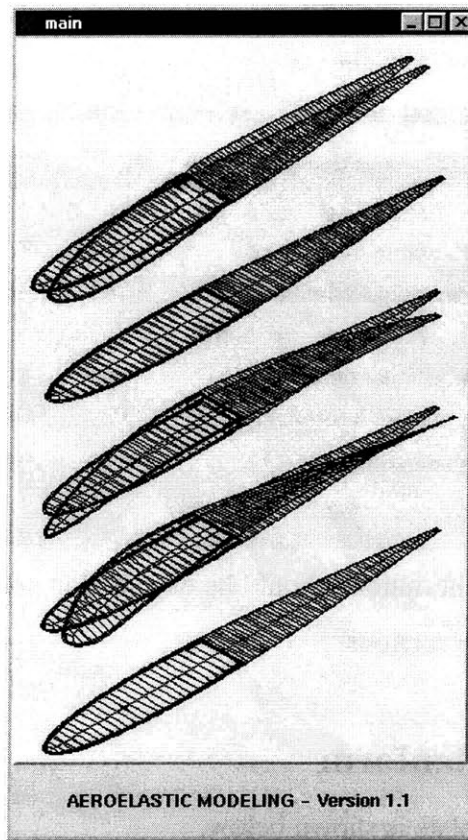
Most of these directories are divided into *data* and *code*. *code* contains all the executable files while *data* holds the associated data. The data is in turn classified in different directories, each one labeled as the correspondent project. There are two possibilities for file input:

1. placing the files directly in the appropriate subdirectories in the event that those directories have already been created, or
2. placing them directly in the *input* directory.

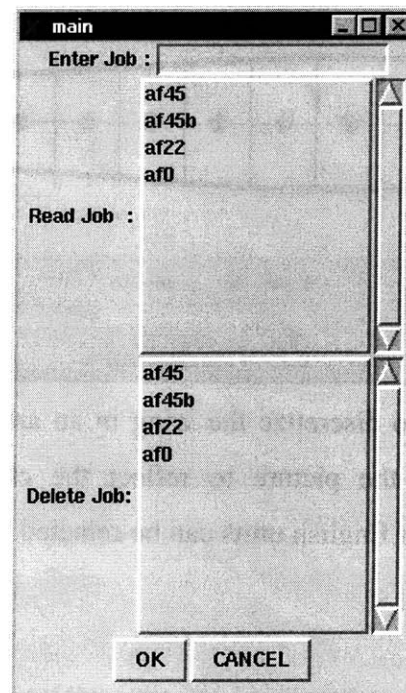
The program will always look first in the appropriate subdirectory for the required files in each aeroelastic option. If the directory or the files do not exist, the program will automatically revert to the *input* directory.

The Main Menu

Once the program is started by typing `main`, the welcome screen appears:



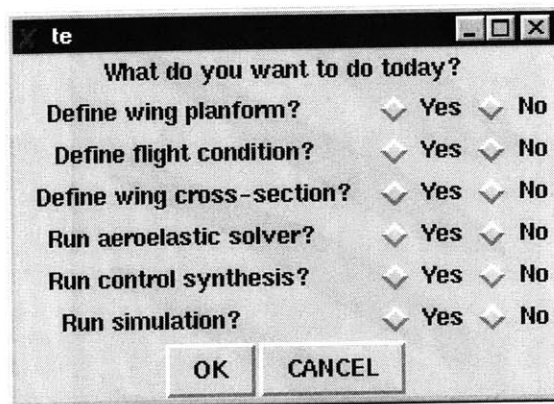
Clicking anywhere on the window leads to the main menu screen:



The main menu dialog window allows three options:

- To start a new project by typing a new name in the input box.
- To read the data from a previous project.
- To delete any of the previous projects.

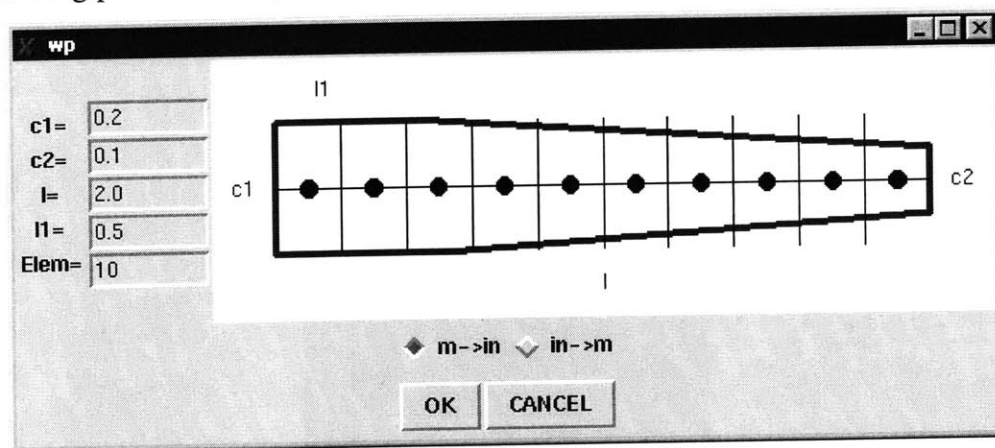
Once the project has been selected, the option selection screen pops up:



For a new project, the different options should be executed in sequence. All these options are described in the following sections.

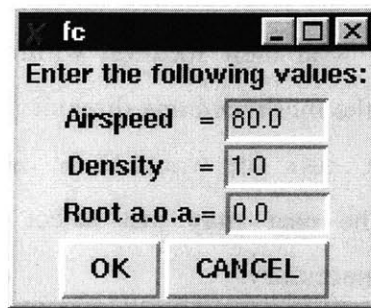
Defining the Wing Planform

The wing planform template is shown below.



The program allows the user to discretize the wing in an arbitrary number of elements and it automatically updates the picture to reflect the changes. The wing can be symmetrically tapered and SI or English units can be selected via the radio buttons.

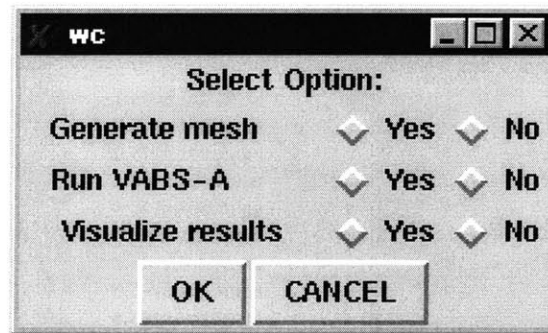
Defining the Flight Conditon



This template only serves as a reminder for the user, but it does *not* automatically update the appropriate analysis files in the current version.

Obtaning the Wing Cross-Section Properties

The wing cross-section option starts with another template with three options:

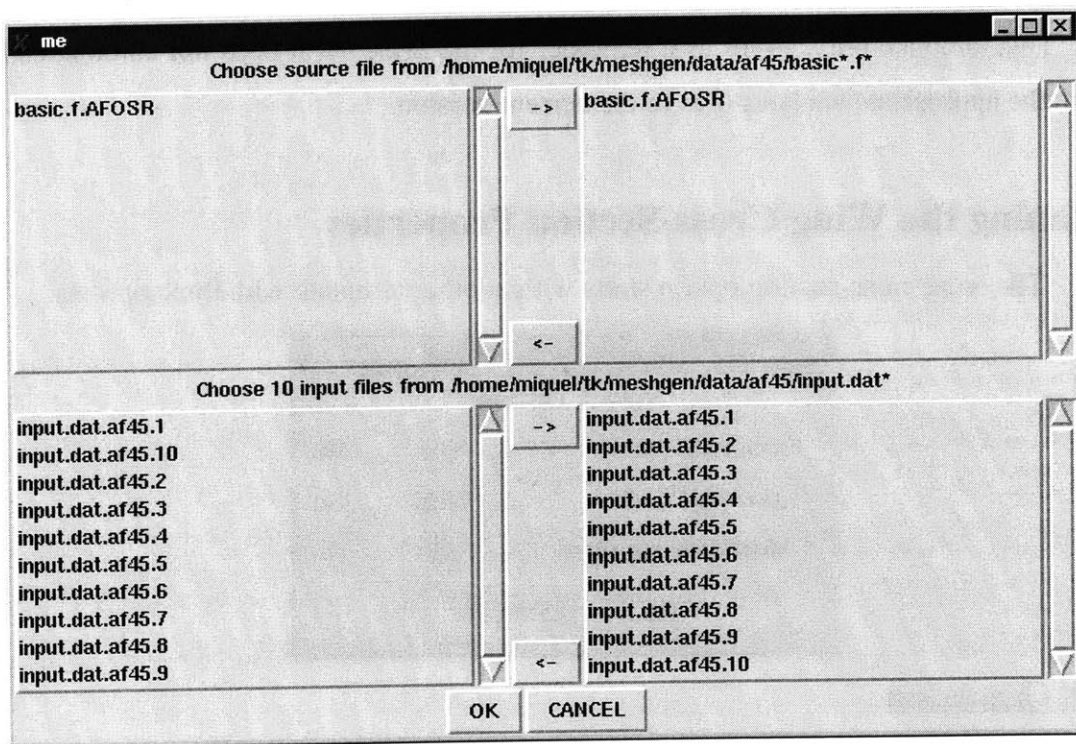


Mesh Generation

The dialog that pops up is a front-end for the files that the mesh generator requires. The user must enter them using any of the two options mentioned above.

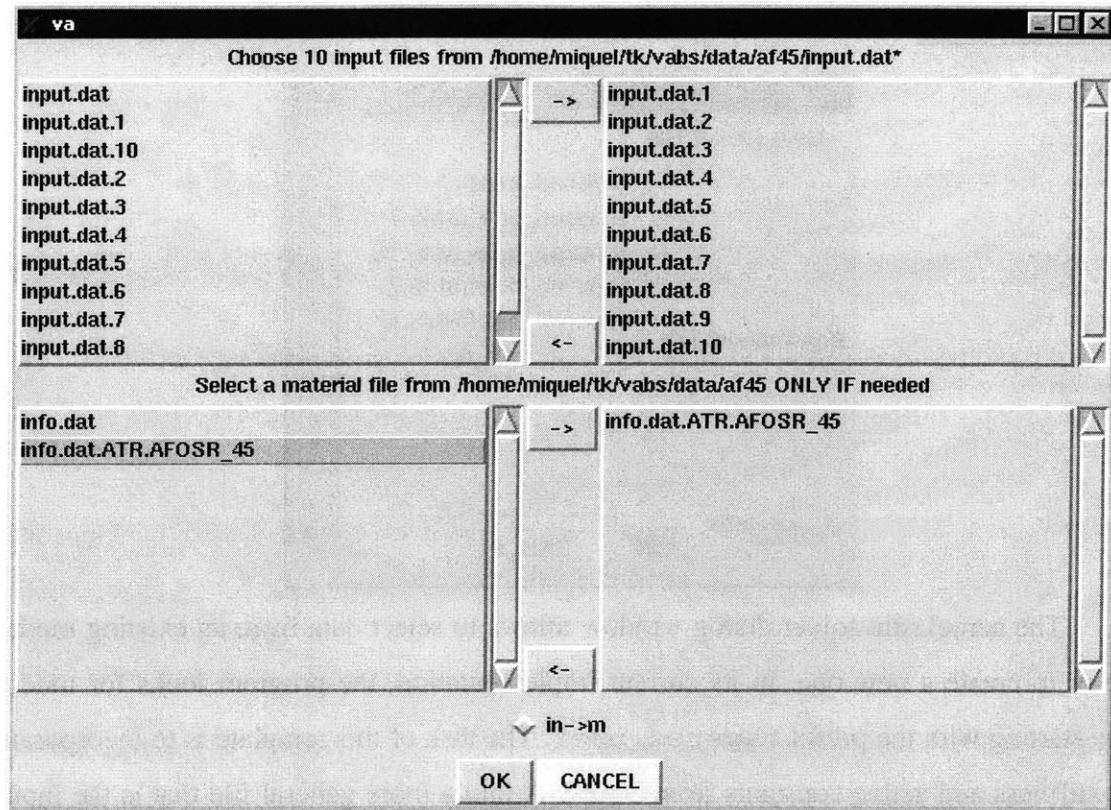
The top half of the window allows to select one `basic.f` file, which is a Fortran source file to contain the mathematical equations defining the airfoil profile. This file will be compiled by the program upon leaving the dialog window. Note that the program always looks for files starting with the string "basic.f," and will display them on the left subwindow. This applies to every option in the program, and must be remembered when reading the following sections. File selection is always accomplished by clicking the file on the left subwindow and then pressing the '->' button, which copies it to the selection window on the right.

The bottom half of the dialog window allows the selection of as many `input.dat` files as elements in the discretization of the wing. Each file must contain the lay-up information together with their location within the cross-section at every station (see the `readme` file in the `meshgen/code` directory for more information on the file syntax). If the same `input.dat` file wants to be used for every element (for a straight wing, for instance), the user may just select one file and the program automatically will replicate it as necessary.



Running VABS-A

This option provides a front-end for VABS-A, running it for every discretization element. The dialog window is shown on the following page. The top half allows the selection of the `input.dat` files that VABS-A needs, which are basically the ones output by the mesh generator routine. If the mesh generation option has been already run, the generated files will automatically be shown on the left. If the wing is straight, the program will allow to select only one file for all the stations. In that event, VABS-A will only be run once, since all files are the same. The program also avoids to run VABS-A on the sections of a tapered wing that share the same properties.



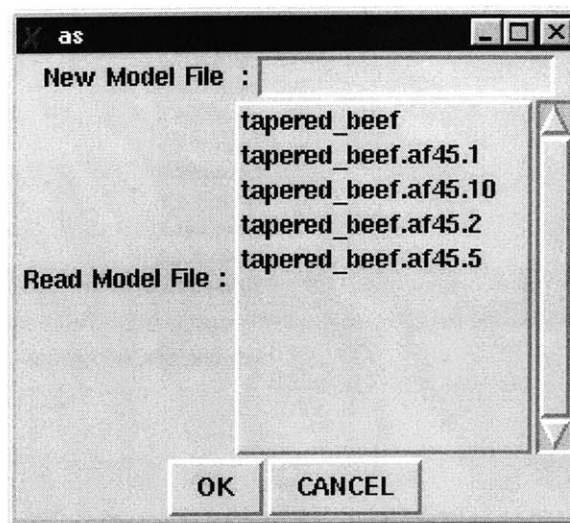
The bottom half of the window allows the material file selection, which must have the prefix `info.dat`. Please refer to the `readme` file in the VABS-A subdirectory for the right syntax.

Visualization of the Results

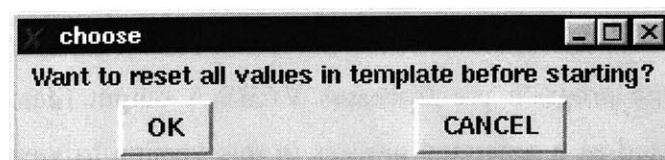
Even though the program pre-processes VABS-A output files for visualization, Matlab has to be started as a separated process in this version to view them, due to an incompatibility between the two.

Running the Aeroelastic Solver

The Model File



The aeroelastic solver dialog window allows to select data from an existing model file or to create a new one. In its current implementation, the program looks for model files starting with the prefix `tapered_beef`. The task of this template is to incorporate the stiffness and active constants from VABS-A into a more general file that is the input for the solver. In fact, the template allows to embed current VABS-A results into an existing file. To do this, the old file must be read first. Then, the new file must be created, at which point the program will ask if it should erase the old data in memory. Canceling this dialog will preserve the old data and just include the new VABS-A results.



Once a name has been selected, a series of templates will appear on the screen for input:

Element Data

One template for every discretization element will pop on the screen. One is given for reference on the following page. Please refer to the `readme` file in the `aerosolv/code` directory for a detailed description of every entry box in the template.

elem10			
Element number	10		
Length of element	1	1	
Offset of the center of element	0	1.90000	0
Curvature of undeformed frame	1	1	
Rotation matrix of undef. frame	1	1	
The m, zeta and l of full element	0	0.21330000E+00	
		0.00000E+00	-0.21330000E-01
		0.0610000E-02	0.00000E+00
		0.00000E+00	0.59540E-05
		0.00000E+00	0.00000E+00
Flexib. dgdf, dgdM, dkdF, dkdM	0	3.20578521E-07	0.
		0.	0.
		0.	0.
		-2.70754971E-07	-3.49312234E-11
		0.	0.
		0.	0.
		-2.70754971E-07	0.
		-3.49312234E-11	0.
		6.25982997E-09	0.
		0.00807002431	1.0994155E-08
		1.0994155E-08	0.0112426706
		-1.78942913E-06	-2.19049822E-09
		0.533300000000E-01	0.
c/z, control surface l & z_aero	0		-2.1330000000E-02
Cl_alpha, Cd_0, Cl_beta effic.	1	1	
Control num. in charge of flap	1	1	

Force Data

Additional forces can be added to the wing model using a template similar to the one below.

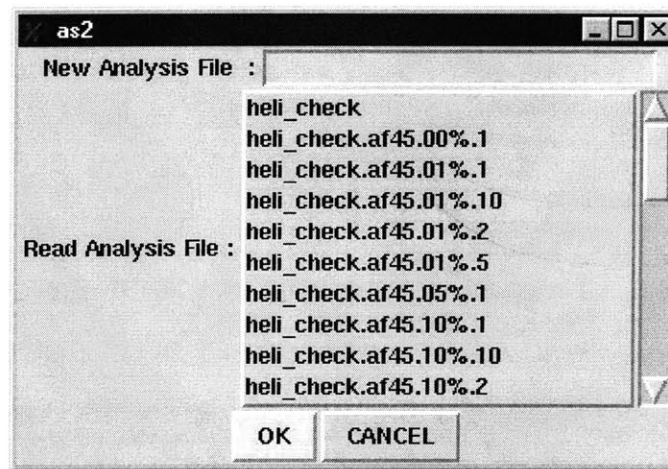
force1			
Element where force acts	0	10	
The force acting on it	0	0.0	0.0
The moment acting on it	0	0.0	0.0
The moment acting on it	0	0.0	0.0
Rotation matrix f-elem	0	1.0	0.0
		0.0	1.0
		0.0	0.0
Control number in charge	0	0	

Piezoelectric Data

One template for every independent actuation region allows to enter the corresponding active forcing constants. One must bear in mind that this information is automatically entered by the program if VABS-A has been run previously. These templates should be considered only as a way to modify that data.

piezo6				
Element where attached	0	6		
Actuator force of piezo	0	-4.24640585	0	0
Actuator moment of piezo	0	-16.7791689	2.48216274E-05	-0.1030697
Control number in charge	0	6		

The Analysis File



The current version of the program only allows selection of an existing analysis file (with the `heli_check` prefix), but it does not provide templates for creation of new files or modification of existing ones. After the selection, the aerolastic solver is automatically run by the program.

4797-17